Wave propagation in mammalian skulls and its contribution to acoustic source localization

Michael Reinwald

SORBONNE UNIVERSITÉ

École doctorale:

Sciences mécaniques, acoustique, électronique et robotique de Paris

THÈSE DE DOCTORAT DE ACOUSTIQUE PHYSIQUE

Wave propagation in mammalian skulls and its contribution to acoustic source localization

---

Par:
Michael REINWALD

Dirigée par
Dr. Quentin GRIMAL
Dr. Lapo BOSCHI

Devant un jury composé de:

Mme. Nathalie Favretto-Cristini	Chargée de recherche, LMA, Aix-Marseille Université	Rapporteuse
M. Eric Larose	Directeur de recherche, ISTerre, Université Grenoble Alpes	Rapporteur
M. Hervé Glotin	Professeur, LSIS, Université de Toulon	Examinateur
M. Olivier Adam	Professeur, d'Alembert, Sorbonne Université	Examinateur
M. Stefan Catheline	Directeur de recherche, LabTAU, Université Lyon 1	Examinateur
M. Quentin Grimal	Professeur, LIB, Sorbonne Université	Directeur de thèse
M. Lapo Boschi	Maître de conférences, ISTeP, Sorbonne Université	Co-directeur de thèse
M. Jacques Marchal	Maître de conférences, d'Alembert, Sorbonne Université	Invité

Présentée et soutenue publiquement le 16 Octobre 2018

"We patronize the animals for their incompleteness, for their tragic fate of having taken form so far below ourselves. And therein we err, and greatly err. For the animal shall not be measured by man. In a world older and more complete than ours, they are more finished and complete, gifted with extensions of the senses we have lost or never attained, living by voices we shall never hear. They are not brethren, they are not underlings; they are other Nations, caught with ourselves in the net of life and time, fellow prisoners of the splendour and travail of the earth."

Henry Beston, 2003

Summary

The spatial accuracy of source localization by dolphins has been observed to be equally accurate independent of source azimuth and elevation. This ability is counter-intuitive if one considers that humans and other species have presumably evolved pinnae to help determine the elevation of sound sources, while cetaceans have actually lost them. In this work, 3D numerical simulations are carried out to determine the influence of bone-conducted waves in the skull of a short-beaked common dolphin on sound pressure in the vicinity of the ears. A 3D model of the skull is created via CT scans, and assigned material parameters are verified via modal analysis. Depending on how bone tissue is modeled (acoustic, elastic, or solid rigid), sound pressure levels computed at the ears vary largely. However, the skull is not found to induce any salient spectral notches, as pinnae do in humans, that the animal could use to differentiate source elevations in the median plane; albeit, bone tissues and their surrounding soft tissues have the largest acoustic impedance mismatch in the head. The results instead suggest that signals reverberated within the dolphin's skull contain sufficient information to discriminate median-plane sound source positions. The potential of reverberated elastic waves for acoustic source localization is confirmed in a preliminary test using a human skull-shaped antenna. Experiments are conducted in a water tank by deploying sound sources on the horizontal and median plane around a skull of a dolphin and measuring bone-conducted waves in the mandible. Their full waveforms, and especially the coda, can be used to determine source elevation via a correlation-based source localization algorithm. While further experimental work is needed to substantiate this speculation, the results suggest that the auditory system of dolphins might be able to localize sound sources by analyzing the coda of biosonar echoes. 2D numerical simulations show that this algorithm benefits from the interaction of bone-conducted sound in a dolphin's mandible with the surrounding fats. Not only does this combination (fats and bone-conducted sound) induce large amplitudes for source azimuths of around 20° to the ipsilateral side for each ear respectively, it also increases the complexity of the waveforms at the ears, and, consequently, increases resolution of the full-waveform algorithm.

Keywords Elastic wave propagation; Time reversal; Source localization; Auditory cues; Bone conduction; Dolphin sonar.

Résumé

La précision avec laquelle le dauphin localise les sources sonores est excellente, que les sources soient situées dans le plan médial ou dans le plan transverse. Cette faculté est contre-intuitive étant donné que les dauphins n'ont pas d'oreille externe (pavillon), qui joue un rôle important chez les autres mammifères pour la localisation de sources en élévation. Dans cette thèse, des simulations tridimensionelles ont été réalisées pour déterminer l'influence de la conduction osseuse du son dans le crâne d'un dauphin commun à bec court sur la pression acoustique au voisinage de l'oreille. Le modèle numérique a été construit à partir d'un scanner et son réalisme a été testé en confrontant le comportement modal du modèle à des données expérimentales. Suivant la manière dont le tissu osseux est modélisé (milieu acoustique, élastique, solide rigide), la pression calculée varie dans des proportions relativement larges. D'autre part, la modalisation n'a pas permis de mettre en évidence d'encoches spectrales telles que celles créées par le pavillon de l'oreille externe des humains et qui codent chez celui-ci l'élévation de la source sonore. Ces résultats nous amènent à penser qu'un signal réverbéré dans l'os du crâne (conduction osseuse) du dauphin contient suffisamment d'information pour discriminer des sources sonores de manière très efficace dans l'espace tridimensionnel. Ce potentiel de la réverbération des ondes et de la conduction osseuse a été confirmé dans une expérience préliminaire qui a utilisé un modèle physique de crâne humain comme antenne acoustique. Une série d'expériences sur un crâne de dauphin, immergé dans une piscine, a permis de mesurer directement la conduction osseuse dans la mandibule. Les formes d'ondes complètes des sons reçus aux récepteurs fixés sur la mandibule, et particulièrement la coda du signal, a pu être utilisée avec succès pour obtenir la position de sources en utilisant un algorithme de corrélation. Ce résultat, qui devra être conforté par la réalisation d'autres expériences, suggère que le système auditif du dauphin pourrait utiliser la coda des signaux reçus lors de l'écholocation. Enfin, des simulations 2D ont permis de mettre en évidence le potentiel bénéfice du couplage de la conduction osseuse du son avec la propagation dans des structures graisseuses de la tête du dauphin. Ce couplage induit en particulier un renforcement des niveaux pour des sources situées à des azimuths autour de 20°. De plus, ce couplage complexifie la forme des ondes reçues par l'oreille, ce qui est en principe favorable pour un algorithme de localisation utilisant la forme d'onde complète.

Mots-clés Propagation des ondes élastiques; Retournement temporel; Localisation de source; Indices auditifs; Conduction osseuse; Sonar des dauphins.

Acknowledgements

Firstly, I would like to express my sincere gratitude to my supervisor Dr. Quentin Grimal for the continuous support of my work. Your patience, motivation, and immense knowledge were fundamental for my professional development over the last three years. I could not have imagined having a better supervisor. Merci beaucoup!

I would also like to thank my co-supervisor Dr. Lapo Boschi, who directly guided my work by continuously sharing many wonderful ideas and discussions, keeping me sane and my work always on the right track. Thank you for your responsiveness and encouragement, but also for the hard questions, which incented me to widen my research and always think further. Grazie mille!

I would like to thank all the jury members for taking the time to examine my work. I am especially grateful to the referees Dr. Nathalie Favretto-Cristini and Dr. Eric Larose for accepting to review this thesis and for carefully reading and commenting on the manuscript. Thank you!

My sincere thanks also go to Dr. Stefan Catheline, Dr. Jacques Marchal, and Christian Ollivon, who provided me with the opportunity to conduct experiments under their supervision, and to Florent Goussard, who helped with numerical modeling. My work would not have been successful without your positivity, great sense of humor, and guidance, despite my constant impatience. Sorry about that!

Thanks also go out to my fellow doctoral students in the WAVES program for being awesome remote colleagues and creating friendships and memories all over Europe. What a cracking group!

Thanks to some people in the LIB: Catherine, Laura, Maryline, Jami, Florian, Nicolas, Andres, Xiran, Chao, Jerome, Sylvain, Guillaume, Philippe, Pascal D., and Pascal L., it was great sharing the laboratory with all of you during the last three years. A special mention deserves Didier, who was always happy to answer my questions and help me solve many computational problems. I will pay you one day!

Thanks to my parents for their loving support and tolerance over many years, even the rough ones. You guys truly are my inspiration!

Last, but not least, thanks to my girlfriend and best friend Franziska, who decided to come to Paris with me, and who has been offering infinite love and support during my PhD. I cannot wait for our new adventures to come. Let's stay young together!

Contents

List of Figures

List of Tables

List of Abbreviations

AC	**A**ir **C**onduction
BC	**B**one **C**onduction
FEM	**F**inite-**E**lement **M**ethod
FRF	**F**requency **R**esponse **F**unction
HRIR	**H**ead-**R**elated **I**mpulse **R**esponse
HRTF	**H**ead-**R**elated **T**ransfer **F**unction
ILD	**I**nteraural **L**evel **D**ifference
IPD	**I**nteraural **P**hase **D**ifference
ITD	**I**nteraural **T**ime **D**ifference
MAA	**M**inimum **A**udible **A**ngle
SEM	**S**pectral-**E**lement **M**ethod
SPL	**S**ound **P**ressure **L**evel
SPP	**S**ound **P**ropagation **P**athway
SRTF	**S**kull-**R**elated **T**ransfer **F**unction
TPC	**T**ympano-**P**eriotic **C**omplex
TR	**T**ime **R**eversal
TRM	**T**ime-**R**eversal **M**irror

Chapter 1

Introduction

1.1 Context

Most literature concerned with the evolution of sound localization (e.g., Heffner and Heffner, 2016) postulates that this task is accomplished by means of several well established auditory cues, at least in mammals. While source azimuth can be determined via binaural cues, i.e., comparison of intensities or arrival times at the two ears, it is generally accepted that source elevation is determined with less precision and via certain spectral notches perceived by the ears. Their amplitude and location along the frequency axis, controlled by the complex shape of the pinnae, depend on the position, and in particular on the elevation of the source (e.g., Van Opstal, 2016, Chapter 7). Odontocete cetaceans, despite the absence of pinnae, have been shown to be equally sensitive to changes in the elevation or azimuth, granting them far superior localization accuracy compared to other studied mammals (Heffner and Heffner, 2016, Figure 3).

This work investigates how bone-conducted sound in a dolphin's skull contributes to acoustic source localization algorithms. The question is answered if the skull alone can induce salient spectral cues, similar to the effect of pinnae in terrestrial mammals. Also, bone-conducted waves in a dolphin's mandible, simulating biosonar echoes, are experimentally recorded and used in full-waveform acoustic source localization, fathoming the signals' full potential. It has been suggested (e.g., Nachtigall, 2016; Dobbins, 2007) that the auditory capabilities of dolphins cannot be explained without invoking, within their auditory system, a localization mechanism similar to the proposed full-waveform algorithm, which is different from the binaural/spectral-cue model attributed to other species. Furthermore, this study isolates the influence of certain material properties of the bones and parts of the head on source localization algorithms via numerical simulations.

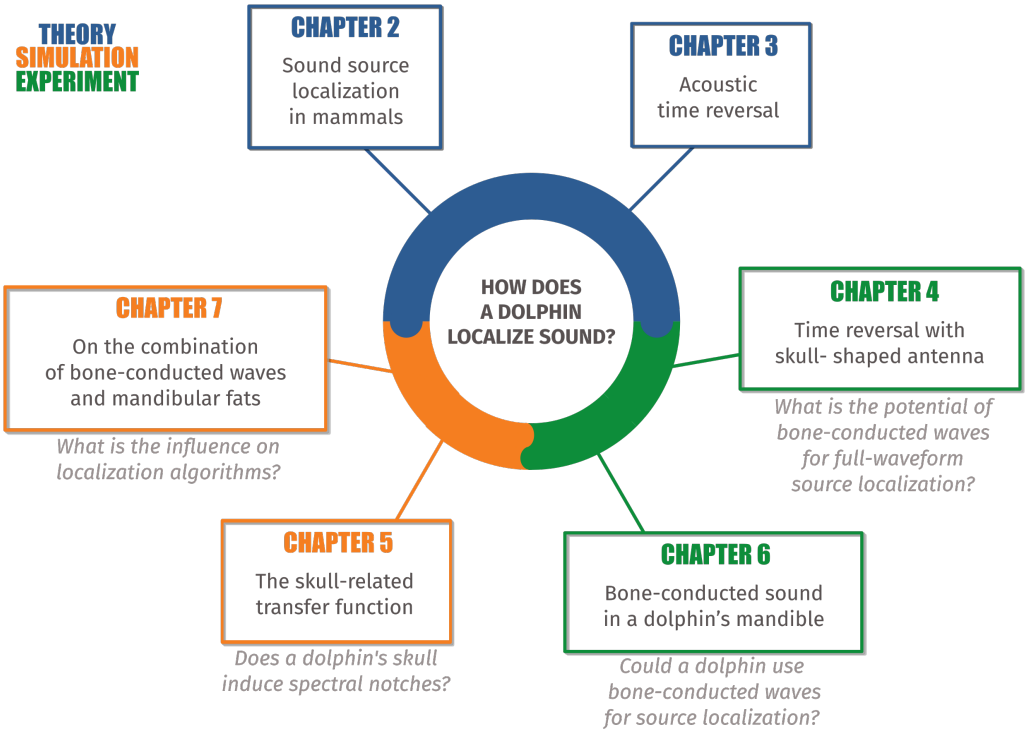

FIGURE 1.1: Graphical overview of all chapters. Colors show different types, either theoretical chapters (blue), numerical simulations (brown) or experiments (green).

1.2 Outline of this thesis

This thesis (excluding this introduction and the conclusion) is comprised of the following six chapters (see also Figure 1.1 for a graphical overview):

Chapter 2 summarizes the current knowledge of sound source localization abilities of mammals, specifically humans and dolphins. For each type of animal, auditory cues are analyzed depending on how they work, either requiring both ears or only one. A strong emphasis is placed on sound propagation pathways through dolphin heads, especially the influence of bone conduction on the animal's ability to localize sound sources.

Chapter 3 contains the mathematical formulation of acoustic and elastic wave propagation as well as a discussion of the acoustic source localization method "time reversal", its theory, strengths, and limitations in the context of how it used in this work. What follows is a discussion of material parameters used to describe elastic media. Furthermore, this chapter is concluded by a short presentation of two computational methods that are applied in this thesis to solve the wave equations, i.e.,

the spectral-element method and the finite-element method.

Chapter 4 discusses the potential of elastic waves propagating in a skull-shaped object for near-field acoustic time reversal by reconstructing sound source positions at below-wavelength distances. The resolution is compared with the theoretical far-field diffraction limit.

Chapter 5 presents the various steps in creating a 3D numerical model of the skull of a common dolphin, such as scanning the specimen and segmenting the scans. A suitable set of material parameters that best describes the vibrational response of the mandible is determined through experimental and numerical modal analysis. The model is then used in frequency-domain numerical simulations using the finite-element method to determine the influence of bone-conducted sound on sound pressure levels at the two ear positions. More precisely, the question is answered if the skull of a dolphin alone can induce salient spectral notches, as pinnae do in humans, that the animal could use to differentiate source elevations in the median plane.

Chapter 6 is a first-ever experimental investigation on the full waveforms of bone-conducted sound waves in a short-beaked common dolphin's mandible. It is determined whether and to what extent they could contribute to the task of localizing a sound source in the horizontal and median plane. This analysis is based on acoustic time reversal.

Chapter 7 presents 2D time-domain numerical simulations on a simplified model of a dolphin's head using the spectral-element method. It complements the two preceding chapters by analyzing the influence of mandibular fats, and their interaction with bone-conducted waves on sound propagation pathways through the head, the resulting signals at the ear positions and acoustic source localization algorithms such as interaural level differences and time reversal in the horizontal plane.

Chapters 4 and 6 correspond to papers submitted to peer-reviewed journals and can be read independently. In order of their appearance, the relevant papers are:

- Reinwald, M., Grimal, Q., Catheline, S. and Boschi, L. (2018). *Super-resolution in near-field acoustic time reversal using reverberated elastic waves in skull-shaped antenna.* Submitted to Acta Acustica united with Acustica.
- Reinwald, M., Grimal, Q., Marchal, J., Catheline, S. and Boschi, L. (2018). *Bone-conducted sound in a dolphin's mandible: Experimental investigation of elastic waves mediating information on sound source position.* Submitted to the Journal of the Acoustical Society of America.

Chapter 2

Sound source localization in mammals

This chapter summarizes the current knowledge of sound source localization abilities of mammals, specifically humans and dolphins. For each type of animal, auditory cues are analyzed depending on how they work, either requiring both ears or only one. A strong emphasis is placed on sound propagation pathways through dolphin heads, especially the influence of bone conduction on the animal's ability to localize sound sources.

Summary

Sound source localization is an ill-posed problem. The mammalian brain has to rely on indirect auditory cues to determine source azimuth and elevation. If the animal uses binaural cues, it correlates time differences or level differences between the two signals perceived at the two ears and, hence, can determine source azimuth. A more significant problem arises in the median plane; here, binaural cues can be assumed to be zero. Consequently, source localization abilities for most terrestrial mammals drastically decrease, since they now have to rely on monaural spectral patterns. They are caused by reflections on the pinna and are less efficient than binaural cues. However, dolphins have overcome this limitation. They locate sound equally precisely, independent of source position. Little is known of how exactly they achieve this ability. Investigations on sound propagation pathways suggest that the mandible, or its overlaying fats, or both, possibly serve as a "human pinna analog", introducing certain spectral colorations that could enable the animal to localize sources in the median plane with very high precision. However, sound propagation pathways in a dolphin's head are still not fully understood. Especially bone-conducted sound and its influence on the perceived sound and possible auditory cues has not yet been thoroughly investigated. Yet, it is not known whether sound localization in dolphins relies on the same mechanisms as in humans and other widely studied species, or on more sophisticated "algorithms" that we do not yet understand.

2.1 Sound source localization as an ill-posed problem

In the famous science-fiction novel "The Hitchhiker's Guide to the Galaxy" by Douglas Adams (Adams, 2010), humankind is confronted with a mind-boggling response of a computer. After calculating for 7.5 million years, the machine, named "Deep Thought", announces that "[...] the answer to the great question of life, the universe and everything [...]" is the number forty-two and that it is up to the humans to find the correct question to save Earth. As confusing (and upsetting[1]) as this reply is, it states a prevalent problem; if one does not know the question, sometimes the answer is not of any big help. Moreover, one can surely find many, actually an infinite amount of, questions for which the correct answer is 42[2]. Speaking the language of science, this problem (one answer, many questions) does not have a unique solution and is ill posed (Kabanikhin, 2008).

The same dilemma also exists in the mammalian auditory system. Sound reaching the ear usually originates from many different sources in the surrounding environment. A person in a restaurant does, for example, not only hear the person at his table talk but he/she could also hear other guests chatting, glasses tinkling, employees working in the kitchen and maybe some background music. Telling where one of these sounds comes from or what caused the sound is an ill-posed problem, because, in theory, there is an infinite amount of combinations of sound sources and sound source parameters[3] that could lead to the same perceived sound wave at the ear (Van Opstal, 2016). But it turns out that the auditory system is doing excellent work, not only in selectively attending to certain sounds, an ability often referred to as "cocktail party processing", but also in reducing the number of possible solutions to this problem and eventually identifying the best one, similar to probabilistic algorithms finding the solution to an inverse problem with the smallest error (Tarantola, 2005). It has developed ways to localize and discriminate sound sources through physical, simple, and indirect auditory cues, which solve most ambiguities and guide the individual in tasks such as navigation, hunting or communication (Köppl, 2009; Blauert, 1997). Studies suggest that the need to localize sound sources and therefore the development of these auditory cues has been an essential factor in the evolutionary changes of the auditory system in terrestrial mammals (Heffner and Heffner, 1992; Masterton, Heffner, and Ravizza, 1969).

[1] "Forty-two!" yelled Loonquawl "Is that all you've got to show for seven and a half million years' work?"

[2] How many US states existed on January 1st, 1890? What is 20+22? How many goals did Cristiano Ronaldo score in all competitions in the '16/'17 season?

[3] These parameters are, e.g., number of sources, frequency spectrum, times of arrival, loudness, and sound source position in 3D.

2.2 Auditory cues

In the following discussion of auditory cues, multiple source environments are neglected, and the subject's head, let it be from an animal or a human being, is assumed to be stationary, i.e., not moving. Most of the assumptions are generalized over the entire range of terrestrial mammalian species unless otherwise mentioned.

The position of a sound source is defined in polar coordinates of *azimuth* and *elevation*, whereas the third dimension (distance/radius) is neglected; the azimuthal angle φ describes horizontal changes in sound source position. By definition, positions to the left of the median plane correspond to negative azimuths ($\varphi < 0°$), positions to the right of the median plane to positive azimuths ($\varphi > 0°$). The azimuth is defined as $0°$ directly in front of the head (in the median plane). Likewise, elevation angles ϑ are defined to be negative ($\vartheta < 0°$) below the head and positive ($\vartheta > 0°$) above the head. The horizontal plane is, therefore, defined as the plane with zero elevation ($\vartheta = 0°$) incorporating the two ear positions, and the median plane as the plane with zero azimuth ($\varphi = 0°$) cutting the head in a left and a right half.

2.2.1 Binaural cues

There are two prominent auditory cues used by most mammals that require both ears, therefore named binaural cues (Blauert, 1997). Many scientists have investigated the role of the two ears in sound localization, such as Prof. Andrew Mayer, when he invented the "topophone" in 1880 for easier navigation through fog (Figure 2.1). In World Wars I and II, and before the invention of radar in the 1930s, such systems were used by many countries' military[4] to passively localize planes over great distances by listening to the noise of the engines. However, the method became obsolete with the invention of active radar. The first physical analysis of binaural cues has been done by Lord Rayleigh around 1900 and has hold up to be mostly valid until today (Rayleigh, 1907; Rayleigh, 1896). The first binaural cue is the *interaural time difference* (ITD) which results from the different paths sound takes while it propagates to the two ears from a certain azimuthal angle. If the sound originates from a position with negative azimuth, i.e., to the left of the subject, the sound will consequently arrive earlier at the left ear than at the right ear. Due to the large density difference between the head and the surrounding medium, sound is refracted and propagates along the head (illustrated in Figure 2.2). ITD in the horizontal plane can, therefore, be estimated through

$$ITD = \frac{r}{c} \cdot (\varphi + \sin \varphi), \tag{2.1}$$

[4]This includes Great Britain, Czechoslovakia, Austria, France, Germany, Japan, Russia, Sweden, USA, and China. For a fascinating collection of historical photographs and sketches of passive acoustic locators used during the first half of the 20th century, the reader is referred to the website of Douglas Self (*http://www.douglas-self.com/*)

FIGURE 2.1: Professor Andrew Mayer and his invention - the topophone. This drawing appeared in the Scientific American in 1880 (Anonymous, 1880). The device was supposed to help the user in determining "[...] quickly and surely the exact direction and position of any source of sound" while navigating through fog (Mayer, 1880).

where r is the head radius and c is the speed of sound in air. This equation, defined by Woodworth and Schlosberg (Woodworth and Schlosberg, 1938), is based on ray tracing and simplified geometries; it assumes a spherical head, computes the path length as a straight path tangential to the head plus the arc length from the point of tangency ξ to the ear. While more acute approximations have evolved (Klump, 2000), the "Woodworth model" mostly fits the data for a certain frequency range and range of terrestrial mammals, including humans (Kuhn, 1977; Middlebrooks, 1999; Heffner and Heffner, 1992). Following Equation 2.1, ITD is highly dependent on head size; the bigger the head, the higher the maximum ITD. For pure tones (a sinusoidal sound), where the onset is ill-defined, ITDs are usually evaluated by the listener through *interaural phase differences* (IPD) (Stevens and Newman, 1936). As soon as the frequency of the sound is higher than a certain limit (i.e., the time it takes for sound to travel one wavelength is smaller than twice the ITD), these phase differences become ambiguous and ITD could only be solved through neural cross correlation (Konishi, 2003). These two limitations are illustrated in Figure 2.3. Humans, for example, rely on ITDs smaller than 750 μs due to their approximate head radius of 10 cm. The maximum frequency without ambiguous azimuths using IPDs is roughly 1.4 kHz.

There are many models, mostly based on the cross correlation of the signals perceived by the two ears, which try to explain the neuronal mechanisms responsible for encoding ITDs in the mammalian brain. The most famous examples are the "Jeffress model"(Jeffress, 1948) and the contralateral inhibition model (McAlpine and

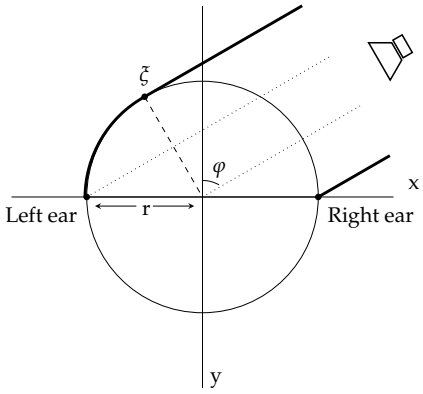

FIGURE 2.2: Woodworth's model of ITD in the horizontal plane (Equation 2.1). The difference in distance between a sound source and the two ears depends on the time it takes for sound to refract around the head.

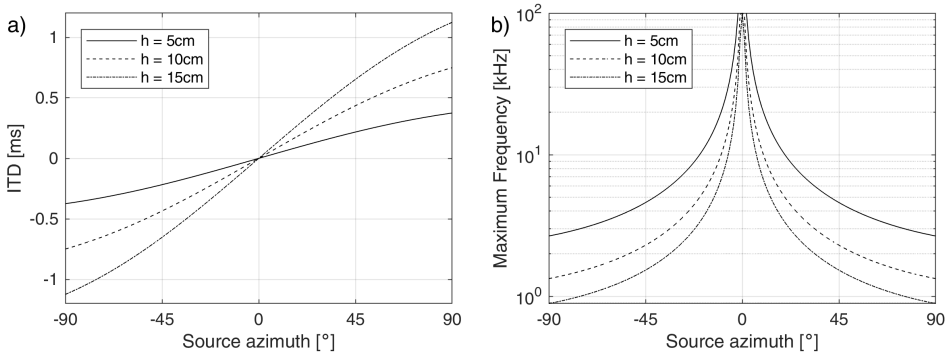

FIGURE 2.3: ITD limitations based on Woodworth's model (Equation 2.1). The speed of sound is set to be the approximate speed of sound in air (343 m/s). **Left**: The maximum ITD due to the different sound paths to the two ears (y-axis) is shown for various head sizes h (5 cm, 10 cm and 15 cm), and source azimuths (x-axis). The larger the head, the larger the maximum ITD. **Right:** The maximum frequency still resolvable through IPDs (y-axis) is shown for various head sizes, and source azimuths (x-axis). Maximum frequencies decrease with increasing absolute azimuth and decrease with increasing head size.

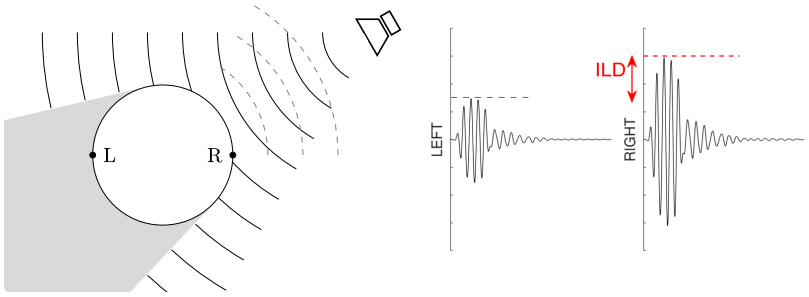

FIGURE 2.4: Schematic illustration of the "shadowing effect" and ILD. When the wavelengths are small enough, some of the energy is reflected off the head. Hence, sound is perceived louder at the ear closer to the sound source, and of less intensity at the ear which is on the other side.

Grothe, 2003). However, they both fail to account for the entire span of findings, such as animals that are sensitive to ITDs that extend to beyond their physiological range (Van Opstal, 2016). The discussion of how the mammalian brain precisely processes time or phase differences has therefore neither been settled yet nor would it fit into the framework of this thesis.

The second binaural cue is the *interaural level difference* (ILD), also known as interaural intensity difference. It is caused by the diffraction, reflection and refraction of sound waves by the head and body of the subject, often referred to as the "shadowing effect" of the respective anatomy, causing the sound level/intensity to be greater at one ear (the one closer to the sound source) than the other (the ear on the other side of the head). This phenomenon is illustrated in Figure 2.4. If the head is higher in density than its surrounding medium, such as in terrestrial mammals, there is the following rule of thumb: If the wavelength of the sound is smaller than the diameter of the head, some of its energy is reflected. For larger wavelengths, i.e., smaller frequencies, the head is acoustically transparent. Note that this limit is roughly $\frac{343\,\mathrm{m/s}}{0.2\,\mathrm{m}} \sim 1.7$ kHz for humans and almost seamlessly matches the previously discussed upper frequency limit for human ITDs (Figure 2.3). Hence, both binaural cues and their complementary frequency ranges are often referred to as "Rayleigh's duplex theory" (Rayleigh, 1896; Rayleigh, 1907). Since small variations in the anatomical geometry can have a profound effect on the received ILD, there are no theoretical models that fully explain ILD for various sounds and species (Brown, 1994). The current knowledge results mostly from psychophysical or acoustic experiments and empirical data for, e.g., humans (Van Wanrooij and Van Opstal, 2004; Firestone, 1930), alpacas (Heffner, Koay, and Heffner, 2014), or bats (Heffner, Koay, and Heffner, 2010).

2.2.2 The cone of confusion

While it is known that ITD and ILD are reliable cues for most terrestrial mammals, both can not unambiguously be used to determine the sound source position in three-dimensional space. If the head is considered to be symmetric, there are many positions that yield the same ITD and ILD. Determining the source position using these cues would be an ill-posed problem, as discussed in Section 2.1. Each azimuth φ has its own so-called "cone of confusion", which is defined by rotating the line

$$y = \frac{\cos(\varphi)}{\sin(\varphi)} \cdot x \tag{2.2}$$

around the (x-)axis connecting the two ears (Van Opstal, 2016; Blauert, 1997). Here y is the coordinate along the vertical axis centered between the two ears. All sources on the surface of such a cone will result in the same ITD[5]. If φ approaches 0°, the cone of confusion spans the entire median plane. Hence, sound sources in the median plane cause no ITD and ILD for all source elevations, if previous simplifications of the head are considered[6] (Woodworth and Schlosberg, 1938).

2.2.3 Monaural cues - The head-related transfer function

As a consequence, most mammals require a third auditory cue that allows them to determine any sound source position, including discrimination of sound source elevations in the median plane (Blauert, 1969). This cue is the spectrum of the received sound; head, pinnae, torso, and other parts of the body act as a direction-dependent spectral filter and change sound on its way to the ears. All of these spectral colorations, including reflections, refractions, etc., are described by the so-called *head-related transfer function*[7] (HRTF) (Wightman and Kistler, 1989). The HRTF is often referred to as a monaural cue since the spectral analysis does not require both ears, but only one (Middlebrooks, 2015).

In the time domain, any acoustic signal $s(\mathbf{r}_{R/L}, t)$ received at one of the two ears $\mathbf{r}_{R/L}$ is a convolution of the source function $c(\mathbf{x}, t)$ emitted at point $\mathbf{x}$, and the time-domain analog of the HRTF, i.e., the *head-related impulse response* (HRIR) $h(\mathbf{x}, \mathbf{r}_{R/L}, t)$:

$$s(\mathbf{r}_{R/L}, t) = c(\mathbf{x}, t) * h(\mathbf{x}, \mathbf{r}_{R/L}, t) \overset{\text{def}}{=} \int_{-\infty}^{\infty} h(\mathbf{x}, \mathbf{r}_{R/L}, t-\tau) c(\mathbf{x}, \tau) d\tau. \tag{2.3}$$

[5] This also holds for ILD considering a perfectly spherical head.

[6] One noteworthy exception to his is the barn owl, which has asymmetrically positioned ears (Keller, Hartung, and Takahashi, 1998).

[7] Dr. Jens Blauert, emeritus professor at the Ruhr-Universität Bochum, and author of the famous book *Spatial Hearing: The Psychophysics of Human Sound Localization* (Blauert, 1997), mentioned in a public e-mail discussion in 2018 that he discussed the term HRTF with Wightman and Kistler, around the time when it became popular. All of them agreed that the term is semantically wrong, and should rather be called head transfer function (HTF) because it is indeed the transfer function of the head, and not only related to the head. But " [...] it was too late [...] and Americans love their catchy abbreviations".

Here, $*$ denotes convolution. In the frequency domain, the received signal $S(\mathbf{r}_{R/L}, \omega)$ is therefore a multiplication of the source function $C(\mathbf{x}, \omega)$ and the HRTF $H(\mathbf{x}, \mathbf{r}_{R/L}, \omega)$:

$$S(\mathbf{r}_{R/L}, \omega) = \mathcal{F}\left[c(\mathbf{x}, t) * h(\mathbf{x}, \mathbf{r}_{R/L}, t)\right] = C(\mathbf{x}, \omega) H(\mathbf{x}, \mathbf{r}_{R/L}, \omega), \tag{2.4}$$

with the angular frequency ω, , where $H(\mathbf{x}, \mathbf{r}_{R/L}, \omega)$ coincides with the Fourier transform of $h(\mathbf{x}, \mathbf{r}_{R/L}, t)$.

It is well known that the external ears, the pinnae, play the most important role in the HRTFs of humans (and probably in most other terrestrial mammals) (Brown, 1994; Batteau, 1967; Roffler and Butler, 1968a), and in their ability to localize sources in the median plane; the most straightforward consideration is that the reflections of sound from the different cavities of the pinna, and their interference with the unreflected sound cause resonances and antiresonances. These spectral features vary with the angle of incidence, i.e., elevation in the median plane, due to the asymmetric shape of the pinna and, therefore, lead to unique spectral patterns for various sound source positions (Kulkarni and Colburn, 1998; Hofman and Van Opstal, 1998). In humans, such spectral notches due to destructive interference of the various sound waves can be seen starting at around 4 kHz and increasing in frequency with increasing elevation (see Figure 2.5). While some studies suggest a more complex scenario, with several notches and respective frequency dependence (Iida et al., 2007), all come to the same conclusion; changes in the spectrum, which can be matched to specific elevations, are caused by the pinnae (Roffler and Butler, 1968a). However, even if the HRTF produces unique spectral patterns for various elevations, monaural extraction of sound source positions is still a difficult task for the mammalian brain. It is generally accepted that the regular pattern of spectral notches, caused by the shape of the pinna, renders a simple cue that humans use for differentiation of sound source positions in the median plane (Van Opstal, 2016). This ability drastically decreases if the pinna cavities are changed in shape (Musicant and Butler, 1984; Humanski and Butler, 1988). However, this method needs a broadband signal spectrum to function; it has been shown (e.g., Pratt, 1930; Roffler and Butler, 1968b; Blauert, 1969) that humans are not able to localize a pure tone in the median plane. Furthermore, every individual has its own shape of head and pinnae (Xie, 2013) and the human brain has to learn to associate the spectral notches with certain source elevations. However, human listeners can adapt to new HRTFs, so to say, new anatomy, over multiple experimental sessions (Minnaar et al., 2001).

2.2.4 The minimum audible angle

The most common way to quantify the ability of a mammal to localize sources in the horizontal or median plane in psychoacoustic studies is the *minimum audible angle* (MAA) (Mills, 1958), i.e., the minimum angular distance between two sources of

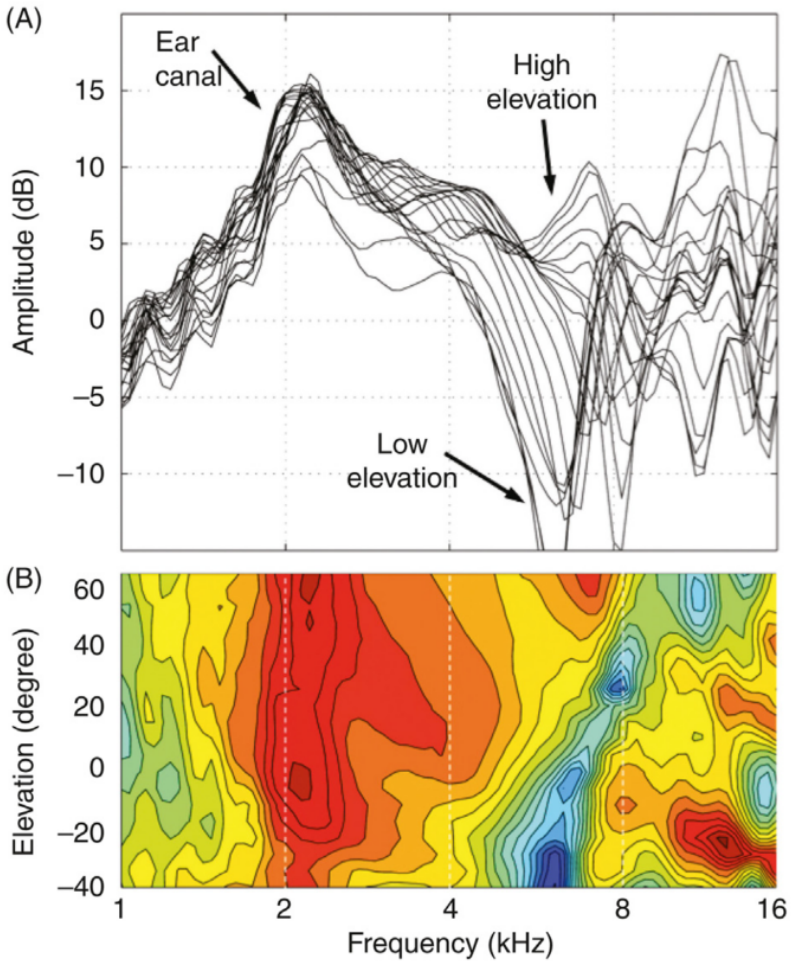

FIGURE 2.5: Measured head-related transfer functions of human subject. **A)** Amplitude spectra at elevations between -40° and 60° in 5° steps. **B)** Same data, plotted in color scale. Both panels show the elevation-dependent notch (dark blue) caused by the pinna and increasing in frequency with increasing elevation. Taken with permission from Van Opstal (Van Opstal, 2016, Figure 7.15).

sound, still allowing to discriminate them as two different sources. If two emitting sources are closer than this angle, they are perceived as only one source.

The advantages of this method are short training periods and simple (binary) required responses of the subject (May et al., 1995). Increasing head size is thought to be helpful since it creates larger acoustic cues and, therefore, possibly decreases the MAA. On the one hand, some data agree with this assumption; MAAs in the horizontal plane are around 1-2° for humans, 5° for cats and 12° for Norway rats. On the other hand, MAAs for horses and cattle are around 25-30°, which can not be explained by head size alone but other factors such as the influence of vision (Heffner and Heffner, 2016). MAAs in the median plane are usually worse due to the absence of binaural cues (Section 2.2.1); for humans, the values increase up to 4-7° for zero elevation and higher values at higher elevation (Wettschurek, 1973; Perrott and Saberi, 1990; Nachtigall, 2016).

2.2.5 Role of bone conduction

The sound propagation pathway to the inner ear in humans is mostly through air. Acoustic waves travel unidirectionally through the ear canal, vibrate the tympanic membrane, and are amplified by the middle ear ossicles (malleus, incus and stapes) to balance the impedance mismatch between air and the fluid-filled inner ear of around 36 dB (Au and Fay, 2012). This path is, therefore, often termed *air conduction* (AC), especially to differentiate it from the so-called *bone conduction* (BC), a process in which the fluids of the cochlea are set into motion through vibrations of the skull and surrounding tissues from various directions (Henry and Letowski, 2007). The tympanic bone, which houses the middle ear, and the periotic bone, which houses the inner ear, have large contacts with each other and the periotic is in close contact to other skull bones. As a result, the ear is not acoustically isolated from the skull and sound waves can travel through the skull (Nummela et al., 2007). By now, BC in humans is a widely accepted phenomenon; bone-anchored hearing devices and BC headphones are the results of decades of industrial research on this topic[8] (Cremers, Snik, and Beynon, 1992; Tjellström and Håkansson, 1995; Wazen et al., 2001; Walker et al., 2005; Buroojy, 2008). BC is quite low for out-of-body sound sources, consequentially likely having a negligible contribution to sound source localization, due to the high impedance ratio between air and the head. However, there seems to be some spatial information present in BC signals; Catheline et al. previously showed via a time-reversal experiment with a dry skull that in-skull elastic wave propagation conducts information about spatial positioning of a sound source (Catheline et al., 2007). That is, the skull essentially acts like an antenna. However, the results of

[8]The first device for utilizing BC was developed in 1924 by Hugo Gernsback (Gernsback, 1924). He filed a patent for an acoustical instrument capable of recording sound and emitting vibrations into the bone tissue of a human subject's skull. He intended to "provide simple and practical means by which hearing may be affected by sound vibrations transmitted directly into the osseous tissue."

this study are purely physical and their implications for auditory or psychoacoustic research remain to be determined. While BC is usually shadowed by AC and considered irrelevant for auditory cues, there are cases in which BC can be perceived as equally loud, or even louder. Some natural sound sources are inside the body, such as the heart or the speech organ; mechanical waves induced by these organs can result in salient bone-conducted signals at the two ears. This is the reason why someone's own voice sounds different when listening to a recording of it since the BC component is missing on the recording but heard when speaking (Taschke and Hudde, 2006).

2.3 Underwater sound source localization

Sound source localization for human divers is a more difficult problem; the middle ear in terrestrial mammals, serving as an acoustic pressure gain device (see Section 2.2.5), does not serve any purpose. Humans, therefore, rely on BC instead of waterborne sound passing through the middle ear (Hollien, 1969; Hollien and Feinstein, 1975) when localizing sound sources underwater. In such an environment, MAAs in the horizontal plane are three times larger than in air (Feinstein, 1973) and probably even larger in the median plane. The explanation is quite simple; the capabilities of both binaural cues are drastically decreased. Since the density of skin, muscles, and other soft tissues is quite similar to the density of water, ILDs are small and are mostly caused by the skull. ITDs are much smaller because of two things: Firstly, sound travels five times faster in water than in air[9], hence, acoustically, the head has the size of a golf ball (Bauer and Torick, 1966), and, secondly, sound does not refract around the head, but travels directly to the two ears since the head is acoustically transparent for most frequencies. ITDs in water can, therefore, be more precisely (than Equation 2.2) computed by taking the difference between the two direct paths to the ears, i.e.,

$$ITD = \frac{2r}{c} \cdot \sin\varphi, \tag{2.5}$$

which is illustrated in Figure 2.6. In addition, monaural cues caused by reflections on the pinna/water interface are nonexistent due to the low impedance ratio (Savel and Drake, 2000). Nevertheless, it should be noted that humans can improve their underwater sound localization abilities through training (Feinstein, 1973; Stouffer, Doherty, and Hollien, 1975).

[9]Depth, temperature, and salinity often give a complex pattern of the underwater sound speed profile (Wartzok and Ketten, 1999). These variations are neglected.

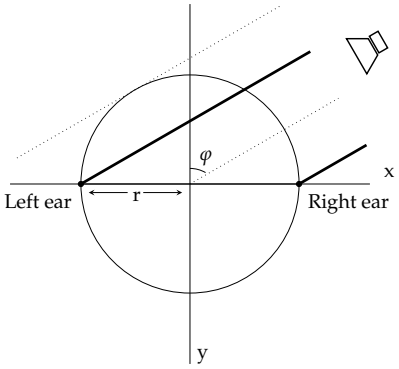

FIGURE 2.6: "Sine" model of ITD in the horizontal plane (Equation 2.5). If the densities of the head and the surrounding medium are roughly the same, the difference in distance between a sound source and the two ears only depends on the difference in direct distance.

2.4 Dolphin hearing and their localization abilities

Section 2.3 discussed the unfavorable circumstances of underwater sound source localization and, at the same time, having ears that are designed to work in air. It is therefore obvious that the ancestors[10] of the oceanic dolphins (*Delphinidae*) had to quickly adapt to aquatic life around 50 million years ago (Branstetter and Mercado III, 2006). Their previous most important sense on land - vision - was rendered basically useless due to the high attenuation of light and sometimes gloomy water. Sound, however, is ubiquitous underwater. Hence, audition had to become the primary tool to localize prey, navigate, and avoid predators. Changes in function and shape of the parts of their anatomy that contribute to the task of sound source localization were inevitable (Au, 2004) and, after 35 million years of "trial and error" (Dobbins, 2007), marine mammals have evolved impressive hearing and sound localization abilities out-performing the ones of humans and even human-made sonar systems (Sigurdson, 1997). Two examples are the highest audible frequency and highest sensitivity to sounds; dolphin audiograms show high hearing sensitivities between 10 and 100 kHz throughout most species (Hemilä, Nummela, and Reuter, 2010). Some, such as the Atlantic bottlenose dolphin (*Tursiops truncatus*), even hear frequencies up to 150 kHz (Au, 2012), while in comparison, humans are known to hear only up to 20 kHz (decreasing with age). The sound pressure of the quietest, but still hearable, sound of optimum frequency, i.e., frequency of highest sensitivity, is around 20 μPa, which is equivalent to an intensity of 1 pW/m^2 for humans (Evans, 1982). This value is roughly 75 times lower for dolphins, i.e., around 0.013 pW/m^2 (Johnson, 1967; Hemilä, Nummela, and Reuter, 1999).

[10] The ancestors of all odontocete cetaceans, i.e., toothed whales, are the Eocene archaeocete whales who lived during or near the Eocene-Oligocene transition (Fahlke et al., 2011).

The reason why odontocetes are of particular interest in auditory research is not only their high-frequency/high-sensitivity hearing but because they have been shown, unlike baleen whales, to use echolocation (Au, 2012), emitting biosonar sounds louder than any other sound made by an animal[11] for various localization tasks. This bat-like sonar system is so fascinating to humans that research on echolocation in dolphins is one of the most studied fields in experimental biology (Thomas, Moss, and Vater, 2004). Early research has shown that dolphins are capable of navigating through a maze of thin metal rods, discriminating various species of fish (Kellogg, 1958), identifiying complex geometric objects (Bel'kovich et al., 1969), and are even able to avoid obstacles while blindfolded (Norris et al., 1961; Norris, 1968a). Even complex acoustic sceneries do not pose a problem to dolphins. Researchers observed nocturnal cooperative feeding of several spinner dolphins (*Stenella longirostris*) (Benoit-Bird and Au, 2009). The pod of dolphins forced an ensemble of mesopelagic biomass to cramp together into a decreasing volume by chasing them and forcing them to coalesce for protection and, unfortunately for the fish, making themselves an easier target for the dolphins. Such a task can only be accomplished by acoustically surveying the position of the fish as well as the pod members at the same time. Biosonar echoes reflected from many targets overlap direct echolocation signals from all dolphins, leading to a cacophony of clicks. The dolphin auditory system seems to be able to analyze such a confuse auditory scene with high precision, but little is known about how they can achieve such tasks (Mooney, Yamato, and Branstetter, 2012). This is an excellent example of how dolphins solved an ill-posed problem, as discussed in Section 2.1. As far as it is humanly possible to judge, echolocation almost seems supernatural. It, therefore, does not come by surprise that it has been used as a superpower for the comic book hero "Daredevil" (Michelinie and Miller, 1980)[12]. It is unknown if dolphins process biosonar echoes similar to the ones of Daredevil, although researchers have attempted, in a rather bizarre experiment, to recreate what dolphins could "see" using echolocation (Kassewitz et al., 2016). All fiction aside, their echolocation abilities are remarkable and, using the words of Erulkar, "those animals that use echolocation for their survival and existence represent the epitome of adaptation for sound localization" (Erulkar, 1972). Most mammals have a similar ratio between interaural distance and maximum hearing frequency (see Sections 2.2.1 and 2.2.4), but this ratio is smaller for dolphins (and echolocating bats); they hear higher frequencies than similar-sized animals that do not echolocate. Heffner, therefore, concludes that the evolutionary selective pressure for echolocation is a reason for their high-frequency hearing (Heffner and Heffner, 2016).

[11] The sperm whale (*Physeter macrocephalus*), which is the largest toothed whale, produces echolocation clicks over 236 dB (re 1μPa per volt at 1m) (Møhl et al., 2003).

[12] "Daredevil has an uncanny radar-sense, like a bat. He emits probing, high-frequency waves. Waves which break against any solid object, and, breaking, send back signals audible only to Daredevil. From these signals, his brain instantly forms silhouette images of everything around him. In this manner, he 'sees' in every direction."

While the auditory capabilities of odontocete cetaceans, such as high-frequency hearing and echolocation, are well known, many questions remain unanswered or are still under debate: What auditory cues do they use to localize sound? How does sound propagate to the ears? What is the role of specific parts of the anatomy, e.g., the bones? What follows should be a short overview of the current state of knowledge of these topics.

2.4.1 MAA

Behavioral experiments on the ability of dolphins to localize sound sources have resulted in some interesting findings; Renaud and Popper measured the MAA of an Atlantic bottlenose dolphin in the horizontal plane to be around 2-3° for pure tones between 6 and 100 kHz (Renaud and Popper, 1975). These values decreased down to 0.7° for broad-band source signals, resembling echolocation clicks. The surprising twist in these results is that MAAs do not increase for sources in the median plane (∼0.9°). This finding is not straight-forward, because it is presumed that dolphins, having two ears, also rely on binaural cues for sound source localization. One would consequently assume that the MAA increases in the median plane due to the absence of ILD and ITD, just like it is the case for humans (see Section 2.2.4).

2.4.2 Binaural cues

The auditory cues that enables dolphins to localize sources in the horizontal plane with such a high resolution are not fully understood. It has been shown that dolphins are capable of using ITDs as small as 7 μs due to the interaural distance and possible delay lines due to low-celerity soft tissues. To be able to achieve MAAs of 1°, the dolphin would have to be able to use ITDs as small as 1.3 μs; a value several times smaller than the measured values (Branstetter and Mercado III, 2006). This result suggests that it is more likely for dolphins to rely on ILD in the horizontal plane, due to their high level of sensitivity to intensities and the high degree of sound shadowing produced by the dolphin's head - mostly by internal structures such as bones or air sacs (Supin and Popov, 1993; Moore, Pawloski, and Dankiewicz, 1995).

2.4.3 The head-related transfer function ... or more?

Things are even more startling in the median plane, where dolphins can equally well resolve sound source positions. Following Section 2.2.3, dolphins would require a highly salient HRTF to explain this phenomenon. Sound would have to reflect off, or diffract through, different structures of varying densities, producing highly frequency-dependent spectral notches. Such a "human pinna analog" has yet to be found, but the lower jaw bone and the mandibular fats have been suggested to play an important role (Ketten, 2000; Aroyan, 2001). Due to the restrictions on

doing in-vivo measurements on live dolphins, the HRTF of dolphin has never been experimentally measured. Most attempts to model HRTFs suffered from various limitations; Krysl and Cranford calculated HRTFs for only three frequencies and with highly varying results depending on the point of evaluation at the ears (Krysl and Cranford, 2016), and Taylor used very coarse spacing of the sound sources (Taylor, 2013). Neither of these studies showed salient spectral notches that would enable a dolphin to localize sources with such a high precision.

It is likely that marine mammals developed specializations to overcome the limited auditory localization mechanisms of terrestrial mammals. Underwater sound sources, let it be from prey or predator, occur in any position in 3D space. Being able to localize them independently of their position, even in the median plane, surely would provide a large selective advantage to a marine animal (Branstetter and Mercado III, 2006). If the dolphin's anatomy includes structures that somehow compensate for the absence of pinnae, or if they are capable of extracting from their HRTF more information than terrestrial mammals in sound localization tasks, or both, still needs to be investigated. Research has shown that the neural circuitry of dolphins involved in auditory processing is much larger and contains more neurons than in humans (Wilson, 2002). Also, the auditory nerve has more fibers and is twice as large (Bullock and Gurevich, 1979; Ridgway, 2000), but brain sizes do not differ (Marino, 1998). The benefits of a larger auditory area in the brain are unknown, but there is little doubt that this grants the species "sophisticated auditory processing", which is not automatically similar to what humans can do (Branstetter and Mercado III, 2006). However dolphins process the HRTF in their brains, understanding how sound propagates through which part of their head, especially the ones that could contribute to spectral filtering (e.g., bones), is crucial to understand their excellent localization abilities in the median plane and come one step closer to a thorough description of a dolphin's HRTF.

2.4.4 Sound propagation pathways through the head

The heads of marine mammals are rather complex structures and differ from heads of terrestrial mammals in many ways (Dierauf and Gulland, 2001; Barroso, Cranford, and Berta, 2012). An illustrative comparison of a dolphin skull and a human skull is shown in Figure 2.7. Skulls of cetaceans show strong telescoping, i.e., an elongation of the beak, and strong deformation of the cranium (Ketten, 1992). They also have a consistent asymmetry, similar to other animals that are known to be auditory predators, such as the boreal owl (Ketten, 2000; Norberg, 1978). Both of these features have been linked to high-frequency sound production and hearing (Fahlke et al., 2011; MacLeod et al., 2007).

Also, the outer ear complex has almost completely vanished; the jutting pinnae of terrestrial mammals, hindering fast underwater locomotion, have been lost in

FIGURE 2.7: Illustration of skulls of an Atlantic bottlenose dolphin (*Tursiops truncatus*) and a human (*Homo sapiens*). Unlike human skulls, dolphin skulls are asymmetric and show strong telescoping. Drawings by Massimo Demma, taken with permission from Cozzi, Huggenberger, and Oelschläger (Cozzi, Huggenberger, and Oelschläger, 2016, Figure 3.3).

favor of hydrodynamics, and the external auditory ear canal has been filled with cellular or wax-like debris (Ketten, 2000; Supin, Popov, and Mass, 2012), since the previously discussed impedance mismatch rendered the middle ear functions of terrestrial mammals useless (see Section 2.3). The hearing organ itself, the cochlea, which produces input to the central nervous system, is embedded in a bony structure, namely the *tympano-periotic complex* (TPC), which is isolated from the skull through air sacs between the periotic bone and the other skull bones (Herzing and Johnson, 2015). Much work has been conducted on the functionality of dolphin inner ears (Mead, 1975; McCormick et al., 1970; McCormick et al., 1980; Ketten, 1992; Ketten, 2000) but will not be further discussed in this thesis. In should be noted, however, that they do not show profound deviations from the mammalian bauplan so that its basic functionality is likely the same as in terrestrial mammals (Cozzi, Huggenberger, and Oelschläger, 2016).

The focus lies, instead, on the *sound propagation pathways* (SPP) towards the inner ear, since we are still in our "infancy of understanding" (Herzing and Johnson, 2015) SPP in a dolphin's head. Possible underlying mechanisms were described by Branstetter and Mercado III as "bewildering" (Branstetter and Mercado III, 2006). There is a lack of empirical physiological data, anatomical data, or numerical simulations that fully describe the involved mechanisms (Taylor, 2013). Due to the low density difference between a cetacean head and water, sound could hypothetically reach the inner ear from any direction (Haan, 1957), but behavioral studies (Au and Moore, 1984; Thomas, Moss, and Vater, 2004) and numerical simulations (Cranford, Krysl, and Hildebrand, 2008; Aroyan, 2001) show a more complex picture; SPP seems to vary depending on source position and frequency.

The most widely accepted theory has emerged in the 1960's, which states that

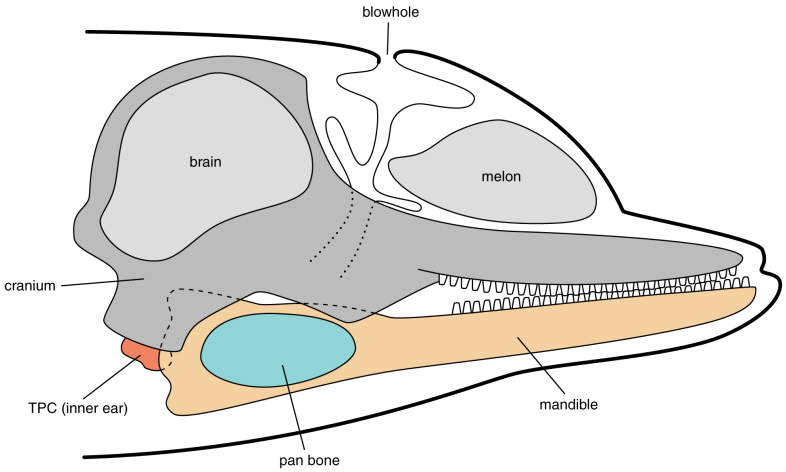

FIGURE 2.8: Structures in a dolphin's head. The cranium (dark gray) which houses the brain is traversed by the trachea, which connects the lungs with the blowhole. The mandible (light brown) with its thin end, the pan bone (turquoise), stretches back to the inner ear (red).

sound propagates through the thin posterior end of the jaw bone (often termed pan bone) and that fat bodies, connecting the pan bone and the TPC, act as a waveguide for incoming sound (Norris, 1968b; Norris, 1968a; Norris and Harvey, 1974; Ketten, 2000). A generalized sketch of the head of a dolphin is shown in Figure 2.8, and the position of these fats is visualized via 3D reconstruction of a head of a pygmy killer whale (*Feresa attenuata*) in Figure 2.9. These fats are only found in the heads of cetaceans and their evolutionary development coincides with skull asymmetry and an enlargement of the pan bones. It is therefore believed that all of these changes are related to hearing (Fahlke et al., 2011). Since then, this theory, often termed "jaw bone theory", has been validated through experimental (Brill et al., 1988; McCormick et al., 1970) and numerical (Aroyan, 2001) results. For example, Brill et al. showed that acoustically shielding the lower jaw tremendously decreases the animal's ability to localize sound.

Also, new theories that extend the jaw bone theory have been proposed: While high-frequency sounds could propagate through the jaw bone, low-frequency sounds (below 30 kHz) could propagate through bone-free fat channels just below the eyes and posterior to the lower jawbone (Brill, Moore, and Dankiewicz, 2001; Ketten, 1994; Popov and Supin, 1990). Cranford, Krysl, and Hildebrand simulated SPP in a head of a Cuvier's beaked whale and proposed a previously undescribed "gular pathway" for sound reception (Cranford, Krysl, and Hildebrand, 2008). This theory describes sound entering the head from below and between the mandibular walls rather than through the posterior mandible. Some studies propose that the teeth play an important role in sound reception; due to their periodic placement, they could act as an acoustic metamaterial, resonating and amplifying sound for specific

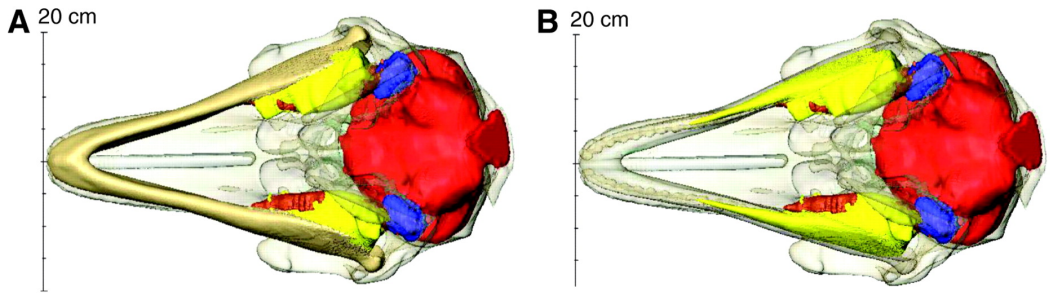

FIGURE 2.9: Ventral views of three-dimensional reconstructions of the head of a pygmy killer whale (*Feresa attenuata*). **A:** This view illustrates the extent of the mandible (light brown), brain (red), TPC (blue), and mandibular fats (yellow). The bone of the skull is transparent and grey. **B:** Here, the mandible is transparent, i.e., highlighting the mandibular fat inside the mandible. Taken with permission from Montie, Manire, and Mann (Montie, Manire, and Mann, 2011).

frequencies (Dible, Flint, and Lepper, 2009; Graf et al., 2009). Other studies suggest that the morphology of the mental foramens found in the mandible helps sound enter the fatty tissues (Ryabov, 2010). Healthy discussions in the scientific community of animal bioacoustics about the various approaches and specific research questions did not help find an overall conclusion yet[13]. The only conclusion to be made from the current state of research is that there could be several SPPs and that it has yet to be worked out what part of the head plays the most important role for any cetaceans species (Taylor, 2013).

2.4.5 Role of bone conduction

While much research has focused on the acoustical properties of the mandibular fats (e.g., Koopman et al., 2006; Gray and Rogers, 2017) and other soft tissues, bone-conducted sound and its role in SPPs has not gotten much buzz. This is, to some degree, surprising; the theory of jaw bone hearing (see Section 2.4.4) suggests that sound passes through fat channels along and through the thin posterior end of the jaw bone. This theory inexorably implies that elastic waves traveling through and along the jaw bone also contribute to the received sound at the ears and should not be neglected in this type of studies. In fact, McCormick et al. hypothesized that the primary mechanism for dolphin hearing should be bone conduction (McCormick et al., 1970). This thought makes, to some degree, sense from a human point of view, since BC is the primary mechanism for human underwater hearing (see Section 2.3). Ketten also theorizes some influence of bone conduction in marine mammal hearing despite the isolation of the skull from the TPC (Ketten, 2000).

[13] Whitlow Au, researcher emeritus at the Hawai'i Institute of Marine Biology, was cited in an article on *nature.com* that the theory of teeth playing an important role in a dolphin's auditory ability is " [...] just a wild hypothesis." (Ledford, 2007).

Few attempts have been made to numerically simulate SPPs in odontocete heads. However, BC has either been neglected or not thoroughly discussed: Aroyan models the jaw bone (and cranium) of a common dolphin as an acoustic medium, i.e., only simulating compressional waves and neglecting elastic waves. Consequently, he suggests that further research should incorporate elastic waves to shed more light on SPPs (Aroyan, 2001). Cranford, Krysl, and Hildebrand show that a complex wave propagation pattern including flexural waves along the mandible bone of a Cuvier's beaked whale likely contributes to the received pressure at its two ears (Cranford, Krysl, and Hildebrand, 2008), but it remains unclear how big of an influence the elastic nature of the mandible has on this pattern.

In conclusion, these studies suggest that further research (numerically and experimentally) is necessary to fully understand the influence of bone-conducted sound on SPPs in odontocete heads, and, consequently, the HRTF of a dolphin.

2.5 The contribution of this thesis

Considering the high density of bones compared to soft tissues, it can be expected that the skull of a dolphin has a big influence on the perceived sound pressure at the ears. This thesis numerically evaluates if the shape and the elastic properties of the skull cause frequency-dependent notches in the HRTF, possibly serving as a "human pinna analog" (Chapter 5). If dolphins cannot or do not use their HRTF in a similar way as humans, their brain needs to be capable of another, more sophisticated auditory processing technique. Therefore, the full waveforms of bone-conducted sound waves are measured on the pan bones of a common dolphin. It is determined whether and to what extent they could contribute to the task of localizing a sound source in the horizontal and median plane (Chapter 6). Finally, numerical simulations show the influence of mandibular fats, and their interaction with bone-conducted waves on sound propagation pathways through a dolphin's head and, consequently, on acoustic source localization methods (Chapter 7).

Chapter 3

Wave propagation physics

This chapter contains the mathematical formulation of acoustic and elastic wave propagation as well as a discussion of the acoustic source localization method "time reversal", its theory, strengths, and limitations in the context of how it used in this work. What follows is a discussion of material parameters used to describe elastic media. Furthermore, this chapter is concluded by a short presentation of two computational methods that are applied in this thesis to solve the wave equations, i.e., the spectral-element method and the finite-element method.

Summary

Sound propagation in an acoustic medium can be described by the inhomogeneous linear wave equation. It relates the changes of pressure in time, to the density of the medium and a possible source term. For an impulsive source, the solution to this equation is called Green's function, which describes how sound changes from source to receiver. Solutions to more complex source terms can be found through convolution of the source term with the Green's function. Due to the reciprocity of the wave equation, source and receiver are interchangeable in the Green's function notation. The source localization method of "time reversal", utilizes this property; one can record wave fields on a closed surface surrounding the source, reversing them in time, and back-propagating them from the point at which they were originally recorded. This procedure focuses the wave field at the original source location. Resolution of this algorithm varies with the positioning and spacing of the receiving elements, as well as with the inhomogeneities of the medium. Wave propagation in solid media introduces new concepts, such as shear elasticity, and new material parameters, e.g., Young's modulus and Poisson's ratio. The governing differential equation is also invariant in time; hence, time reversal can be applied to waves propagating in complex elastic media. Solving both wave equations sometimes requires discretization of the wave field. The finite-element method does this by replacing the unknown field with a finite sum over linear basis functions. The spectral-element method extends this method by using a special set of basis functions, i.e., Lagrange polynomials.

3.1 The acoustic wave equation

3.1.1 The linear acoustic wave equation

The acoustic wave equation in an ideal fluid can be derived, as done in many books on fundamental acoustics (Kinsler et al., 1999; Ginsberg, 2017; Jensen et al., 2000), from several hydrodynamic equations, i.e., the continuity equation, Newton's second law[1], and the relation between pressure and density. Here and in the following equations, ρ is the density, t denotes time, p the pressure, and c is the propagation velocity of the acoustic wave.

The *linear acoustic wave equation* reads

$$\nabla^2 p - \frac{1}{c^2}\frac{\partial^2 p}{\partial t^2} = 0, \tag{3.1}$$

introducing the Laplace operator[2] $\nabla^2 p = \nabla \cdot \nabla p$. So far, Equation 3.1 only applies to regions devoid of any sources of energy. However, it is straightforward to include them, leading to the *inhomogeneous linear wave equation*, i.e.,

$$\boxed{\nabla^2 p - \frac{1}{c^2}\frac{\partial^2 p}{\partial t^2} = \frac{\partial q}{\partial t}.} \tag{3.2}$$

Here, q is a forcing term introducing a mass production per unit volume and unit time. This could be, e.g., an explosion or a loudspeaker (Kinsler et al., 1999). Again, other possible sources such as body forces caused by a moving source in the fluid, turbulences or gravity are neglected.

Without loss of generality, Equation 3.2 can be written in the frequency domain as

$$\frac{1}{\rho}\nabla^2 p + \omega^2 \kappa p = -i\omega q, \tag{3.3}$$

with compressibility $\kappa = \frac{1}{c^2\rho}$.

3.1.2 The Green's function as a solution to the wave equation

Let us consider the source term to be an impulse in time ($t = t_0$) and space (at position $\mathbf{x}_0$), i.e., $\frac{\partial q}{\partial t} = \delta(\mathbf{x} - \mathbf{x}_0)\delta(t - t_0)$ with the Dirac distribution δ and the position vector $\mathbf{x}$. The solution to this problem is called Green's function and denoted G, solving Equation 3.2 and, consequently, Equation 3.3. If the source is more complex than a delta distribution, the solution can be found by convolving the Green's function with the source function (Boschi and Weemstra, 2015). Generally speaking, the Green's

[1] To be more precise, propositions from his second law in his famous work *Principia* (Guicciardini, 2005; Pourciau, 2011).

[2] It should be noted that outside of the anglo-saxon literature it is common to write the Laplace operator as Δ.

function $G(\mathbf{x}_A, \mathbf{x}_B, t)$ describes the wave field $s(\mathbf{x}_A, t)$ perceived at point $\mathbf{x}_A$, if an impulse source is introduced at point $\mathbf{x}_B$, requiring both points to be in an arbitrary volume bounded by a (non-physical) surface. If the source at point $\mathbf{x}_B$ is of more complex shape, e.g., some arbitrary source function $h(\mathbf{x}_B, t)$, the obtained pressure at point $\mathbf{x}_A$ can be described in the time domain through

$$s(\mathbf{x}_A, t) = h(\mathbf{x}_B, t) * G(\mathbf{x}_A, \mathbf{x}_B, t). \tag{3.4}$$

Here, $*$ denotes convolution. This operation corresponds to a multiplication in the frequency domain, hence

$$s(\mathbf{x}_A, \omega) = h(\mathbf{x}_B, \omega) G(\mathbf{x}_A, \mathbf{x}_B, \omega). \tag{3.5}$$

3.1.3 The reciprocity of the Green's function

One property of the Green's function deserves special attention, and that is its reciprocity[3]. Following Wapenaar and Fokkema (Wapenaar and Fokkema, 2006), consider the volume $\mathbb{V}$ enclosed by an arbitrary surface $\partial\mathbb{V}$ and two different scenarios denoted by subscripts A and B. In both cases, the forcing term is defined as an impulsive source at point $\mathbf{x}$. The resulting pressure at points $\mathbf{x}_{A/B}$ can be expressed by the Green's functions $G(\mathbf{x}, \mathbf{x}_{A/B}, \omega)$, respectively solving Equation 3.3 for each scenario:

$$q_A(\mathbf{x}, \omega) = \delta(\mathbf{x} - \mathbf{x}_A), \tag{3.6}$$

$$q_B(\mathbf{x}, \omega) = \delta(\mathbf{x} - \mathbf{x}_B), \tag{3.7}$$

$$p_A(\mathbf{x}, \omega) = G(\mathbf{x}, \mathbf{x}_A, \omega), \tag{3.8}$$

$$p_B(\mathbf{x}, \omega) = G(\mathbf{x}, \mathbf{x}_B, \omega). \tag{3.9}$$

Equations 3.6-3.9 can be combined, using the acoustic reciprocity theorem of the convolution type (Wapenaar and Fokkema, 2006, Equation 5), to obtain the expression

$$\begin{aligned} &G(\mathbf{x}_B, \mathbf{x}_A, \omega) - G(\mathbf{x}_A, \mathbf{x}_B, \omega) = \\ &= \frac{1}{i\omega\rho} \oint_{\partial\mathbb{V}} d^2\mathbf{x} \left[G(\mathbf{x}, \mathbf{x}_B, \omega) \nabla G(\mathbf{x}, \mathbf{x}_A, \omega) - G(\mathbf{x}, \mathbf{x}_A, \omega) \nabla G(\mathbf{x}, \mathbf{x}_B, \omega) \right] \cdot \hat{\mathbf{n}}, \end{aligned} \tag{3.10}$$

[3]The first notable mention of reciprocity was made by Lord Rayleigh in 1877: "The reciprocal property is capable of generalization so as to apply to all acoustical systems whatever capable of vibrating about a configuration of equilibrium [...] and is not lost even when the systems are subject to damping." (Strutt, 1877).

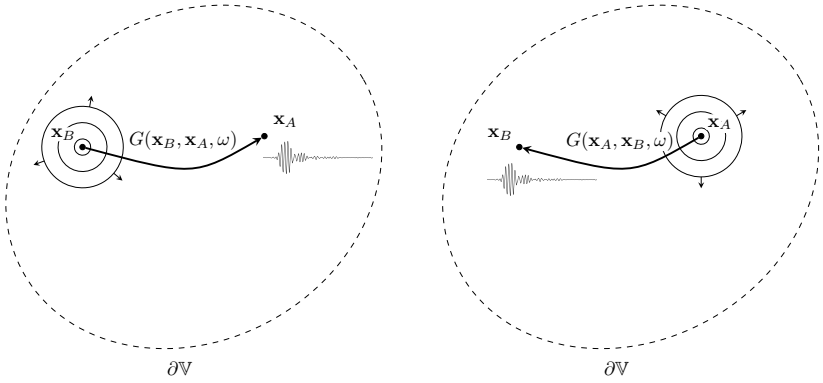

FIGURE 3.1: Illustration of the reciprocity theorem. **Left:** The Green's function $G(\mathbf{x}_B, \mathbf{x}_A, \omega)$ describes how sound propagates from a point of emission $\mathbf{x}_B$ to the receiver at point $\mathbf{x}_A$. **Right:** The Green's function $G(\mathbf{x}_A, \mathbf{x}_B, \omega)$ describes how sound propagates from a point of emission $\mathbf{x}_A$ to the receiver at point $\mathbf{x}_B$. Both Green's functions are equivalent, as long as the same source function are emitted.

with the unit vector $\hat{\mathbf{n}}$ normal to $\partial\mathbb{V}$. Using the radiation condition of the Green's function (Bleistein, 2012), the right-hand side of Equation 3.10 is zero, independent of how $\partial\mathbb{V}$ is shaped, as long as it encloses $\mathbf{x}_A$ and $\mathbf{x}_B$. Thus, the acoustic Green's function shows reciprocity regarding source and receiver position in frequency and time domain:

$$G(\mathbf{x}_B, \mathbf{x}_A, \omega) = G(\mathbf{x}_A, \mathbf{x}_B, \omega), \tag{3.11}$$

$$G(\mathbf{x}_B, \mathbf{x}_A, t) = G(\mathbf{x}_A, \mathbf{x}_B, t). \tag{3.12}$$

This phenomenon is illustrated in Figure 3.1; the signal recorded at $\mathbf{x}_A$ due to a source emitted at $\mathbf{x}_B$, is equivalent to the signal recorded at $\mathbf{x}_B$ if the same source function is emitted at $\mathbf{x}_A$.

3.2 Time reversal

3.2.1 Time reversal as a source localization tool

The following discussion closely reproduces the appendix of the submitted work by Reinwald et al. (Reinwald et al., 2018).

It is well known that, if attenuation is neglected, the imaginary part ($\Im$) of the acoustic Green's function (i.e., impulse response) G associated with a source at $\mathbf{x}_A$ and a receiver at $\mathbf{x}_B$ (or vice-versa) can be obtained by the frequency-domain relationship

$$\frac{\rho c}{\omega}\Im[G(\mathbf{x}_A, \mathbf{x}_B)] = -\int_{\partial\mathbb{V}} \mathrm{d}^2\mathbf{x}\ [G^*(\mathbf{x}, \mathbf{x}_B)G(\mathbf{x}, \mathbf{x}_A)]\,, \tag{3.13}$$

(e.g., Boschi and Weemstra, 2015, Equation 103), where G is the 3-D Green's function and $\partial\mathbb{V}$ is an arbitrary closed surface surrounding $\mathbf{x}_A$ and $\mathbf{x}_B$. The superscript * stands for complex conjugation, so that the integrand at the right-hand side of Equation 3.13 is the Fourier transform of the time-domain cross correlation of $G(\mathbf{x}, \mathbf{x}_B, t)$ and $G(\mathbf{x}, \mathbf{x}_A, t)$.

Think now of $\mathbf{x}_B$ as the location of an acoustic source (e.g., Boschi and Weemstra, 2015); $G(\mathbf{x}, \mathbf{x}_B, \omega)$ is the Fourier transform of an impulse generated at $\mathbf{x}_B$ and recorded by a receiver at $\mathbf{x}$; $G^*(\mathbf{x}, \mathbf{x}_B, \omega)$ is the Fourier transform of the same signal, reversed in time. Imagine that the time-reversed signal be then emitted from $\mathbf{x}$ and recorded at another point $\mathbf{x}_A$: this amounts to convolving (in the frequency domain, multiplying) the time-reversed signal with the Green's function $G(\mathbf{x}_A, \mathbf{x}, \omega)$. Equation 3.13 then shows that by repeating time reversal and propagation ("backward in time") for all points $\mathbf{x}$ on $\partial\mathbb{V}$, and summing all the resulting traces at $\mathbf{x}_A$, the imaginary part of the Green's function between $\mathbf{x}_B$ and $\mathbf{x}_A$ is obtained. Note that the imaginary part of the frequency-domain G coincides, in the time domain, with the inverse Fourier transform

$$F^{-1}\left\{\Im\left[G(\mathbf{x}_A, \mathbf{x}_B, \omega)\right]\right\} = G(\mathbf{x}_A, \mathbf{x}_B, -t) - G(\mathbf{x}_A, \mathbf{x}_B, t), \tag{3.14}$$

i.e., as t grows from -∞ to 0, a time-reversed Green's function, followed by a regular G with its sign reversed (e.g. Fink, 2006).

This procedure is usually referred to as acoustic *time reversal* (TR), because the wave field so obtained is essentially a time-reversed and backward propagated version of the original impulse response G (Fink, 2006); as such, it will naturally focus at the original source location, where it will show a very prominent maximum. An important consequence of this is that TR can be used as a source localization tool. This procedure usually consists of four steps:

1. A source at an *unknown* location $\mathbf{x}_B$ emits an arbitrary signal.
2. Wave fields are recorded by an array of receivers $\mathbf{x}_i$, ideally forming a closed surface $\partial\mathbb{V}$.
3. All of these wave fields $s(\mathbf{x}_i, t)$ are reversed in time and emitted at the point at which they were originally recorded.
4. The back-propagating waves then travel, as if a film showing steps 1) and 2) was played in reverse. By looking for the maximum of the resulting wave field in space at t=0, the source location can be determined.

This procedure is illustrated in Figure 3.2. Here, steps 1) and 2) coincide with the left panel of Figure 3.2, steps 3) and 4) with the right panel of Figure 3.2, and $\mathbb{A}$ is any form of heterogeneity in the compressibility or the density of the media. Such

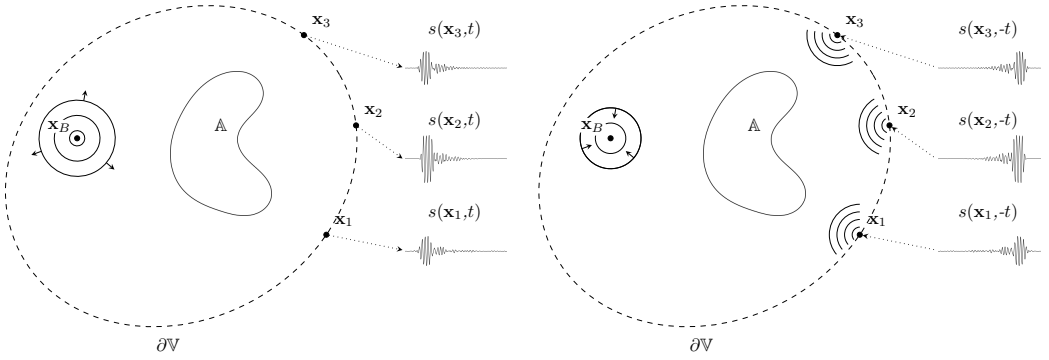

FIGURE 3.2: Illustration of time reversal as a source localization tool. **Left:** A signal is emitted at point $\mathbf{x}_B$, propagates through a volume bounded by the surface $\partial\mathbb{V}$ including all inhomogeneities $\mathbb{A}$ and is recorded at all surface coordinates $\mathbf{x}_{1/2/3/\ldots}$ in $\partial\mathbb{V}$. **Right:** These signals are then reversed in time and emitted at the point at which they were originally recorded. The waves travel back to the original source position where they eventually focus and thereby recreate the original source function.

changes introduce a secondary source term due to its scattering effect on the wave field, but do not introduce new energy into the medium (Cassereau and Fink, 1992). The reciprocity of the Green's function, therefore, still holds true; the Green's function does not only describe the direct wave between $\mathbf{x}_A$ and $\mathbf{x}_B$ but all scattered waves from such heterogeneities, which can even have a positive effect on the TR source localization procedure (see next section).

3.2.2 Time-reversal source localization in practice

Just like any imaging system in optics or acoustics, diffraction limits the resolution for TR source localization in a homogeneous medium to half a wavelength (Fink et al., 2009). The focal spot, also often referred to as the point spread function, i.e., the spatial focusing of the time-reversed and back-propagating wave at $t = 0$, is usually not narrower than this limit. Consequently, increasing the wavelength of an acoustic source increases the resolution of TR source localization. Subwavelength details are usually not incorporated in the recorded signals since they are due to evanescent waves, which can only be recorded in the near field due to their exponential decrease with propagation distance (Rosny and Fink, 2007). In practice, there are some other limitations to the time invariance of the acoustic wave equation:

- The vorticity of a fluid medium can lead to a deflection of the focal spot in space, breaking reciprocity (Roux and Fink, 1995). However, for the extent of this thesis, all fluids are considered to be flowless.
- Additionally, many materials dissipate energy, e.g., in the form of heat. Dissipation adds a first-order time derivative term into the wave equation, breaking

TR invariance, but spatial reciprocity remains valid. The back-propagating wave still refocuses with maximum amplitude at the source position and the variance in time can be accounted for through more sophisticated algorithms (Tanter, Thomas, and Fink, 2000; Tanter et al., 2001). Hence, TR is used widely with dissipative media.

While in principle G is accurately reconstructed (the time-reversed wave field focuses at the original source location with a focal spot size of $\lambda/2$) only if recordings made at a dense, uniform array of receivers are reversed in time and propagated backwards, it is generally difficult in practice to record the wave field at many positions, completely surrounding the area of interest (Fink et al., 2009). Instead, experiments are usually carried out using *time-reversal mirrors* (TRM), i.e., receiver arrays of finite angular aperture, which consequently leads to a decrease in resolution, i.e., increase in focal spot size, since the integral in Equation 3.13 is not calculated along the full path of the closed surface $\partial\mathbb{V}$ anymore, but discretized to a sum of all recordings at a finite number of positions.. In imaging physics, the resolution of a system is roughly proportional to $\frac{\lambda D}{a}$, where D is the distance to the source and a is the aperture, i.e., the spatial extent of the TRM. Generally speaking, the larger the TRM (larger a), the higher the resolution. Heterogeneities that cause multi-path wave propagation through multiple scattering at boundaries between different media can drastically increase apparent aperture size and TR resolution compared to the case of a homogeneous medium, possibly beating diffraction limit (Tsogka and Papanicolaou, 2002; Derode, Roux, and Fink, 1995; Derode, Tourin, and Fink, 2001).

In this thesis, TR is carried out using either one or two receivers. It was shown (Catheline et al., 2007) that a pair of receivers, deployed at ear locations on a human skull, are enough for the time-reversed, backward-propagated signal to sharply focus at the source. Considering this two-receiver setup (subscripts L (left receiver) and R (right receiver), Equation 3.13 can thus be simplified to

$$\Im[G(\mathbf{x}_A, \mathbf{x}_B)] \propto G^*(\mathbf{x}_L, \mathbf{x}_B)G(\mathbf{x}_L, \mathbf{x}_A) + G^*(\mathbf{x}_R, \mathbf{x}_B)G(\mathbf{x}_R, \mathbf{x}_A), \tag{3.15}$$

where, for the sake of simplicity, absolute amplitude informations are dropped since only the maxima of the expressions are of interest. Equation 3.15 is only valid for impulsive signals, but it is straightforward to generalize it to an arbitrary signal $s(\omega)$. Write s as the convolution $s(\mathbf{x}_1, \mathbf{x}_2, \omega) = h(\omega)G(\omega, \mathbf{x}_1, \mathbf{x}_2)$, with h an arbitrary "source time function" independent of the source and receiver positions $\mathbf{x}_1$ and $\mathbf{x}_2$. If one multiplies both sides of Equation 3.15 by $h^*(\omega)$,

$$h^*(\omega)\Im[G(\mathbf{x}_A, \mathbf{x}_B)] \propto s^*(\mathbf{x}_L, \mathbf{x}_B)G(\mathbf{x}_L, \mathbf{x}_A) + s^*(\mathbf{x}_R, \mathbf{x}_B)G(\mathbf{x}_R, \mathbf{x}_A). \tag{3.16}$$

The convolution of s^* with G at the right-hand side of Equation 3.16 should be interpreted, again, as backward propagation of the time-reversed recorded signal

s; Equation 3.16 stipulates that, by this procedure (in the assumption that sufficient information about the wave field be recorded by a pair of receivers alone), a source of arbitrary complexity (with respect to time) can be reconstructed: the time-reversed signal will focus at the source, where a receiver would approximately record the original source time function $h(t)$, reversed in time.

In this work, a slightly different approach is taken (Catheline et al., 2007). Let us multiply both sides of Equation 3.15 by $|h(\omega)|^2$,

$$|h(\omega)|^2 \Im[G(\mathbf{x}_A, \mathbf{x}_B)] \propto s^*(\mathbf{x}_L, \mathbf{x}_B) s(\mathbf{x}_L, \mathbf{x}_A) + s^*(\mathbf{x}_R, \mathbf{x}_B) s(\mathbf{x}_R, \mathbf{x}_A). \tag{3.17}$$

Note that the products at the right-hand side of Equation 3.17 can be interpreted, in the time domain, as both the convolution of $s(\mathbf{x}_{L/R}, \mathbf{x}_A, t)$ with the time-reversed counterpart of $s(\mathbf{x}_{L/R}, \mathbf{x}_B, t)$, and the *cross correlation* of $s(\mathbf{x}_{L/R}, \mathbf{x}_A, t)$ and $s(\mathbf{x}_{L/R}, \mathbf{x}_B, t)$ (Draeger and Fink, 1999; Derode et al., 2003). As opposed to Equation 3.16, the right-hand side of Equation 3.17 does not allow one to reconstruct, from the data, the signal as originally emitted at $\mathbf{x}_B$ (because $s(\mathbf{x}_{L/R}, \mathbf{x}_A)$ are unknown and cannot be computed). Equation 3.17 can be relevant, however, if the time function $h(t)$ is known, while the location of the source is to be determined. This applies, for instance, to echolocating species, that identify and analyze echoes of signals that they have themselves emitted. Echolocation can presumably be learned by training, which is equivalent to forming a "library" of observed echoes $s(\mathbf{x}_{L/R}, \mathbf{x}_\mathbf{A})$ associated with a given emitted signal and known target locations $\mathbf{x}_A$: each time a relevant signal is perceived, the echolocating agent would then systematically compare it to all recorded traces $s(\mathbf{x}_{L/R}, \mathbf{x}_A)$, each corresponding to a different value of $\mathbf{x}_A$ eventually covering the entire solid angle. Imagine that this comparison be implemented via cross correlation: this is equivalent to implementing the right-hand side of Equation 3.17, and the same equation implies that cross correlation should be maximum when $\mathbf{x}_A$=$\mathbf{x}_B$; the sharpness of focusing at the source, and thus the accuracy of source localization, is strictly related to how well a time-reversed, backward propagated wave field would focus at the original source. Importantly, however, the proposed algorithm does not involve any wave propagation modeling, but is based entirely on signal processing of measurements at one or two receivers.

3.3 Elastic wave propagation

Unlike liquids or gases, wave propagation in solids is of more complicated nature; a solid medium not only possesses volume elasticity, which corresponds to the elasticity of acoustic media, but also shear elasticity. Waves induce elastic deformation along the propagation path described by the elastodynamic wave equation. Here, porosity or anisotropy of the medium is neglected, as well as effects of temperature on the medium.

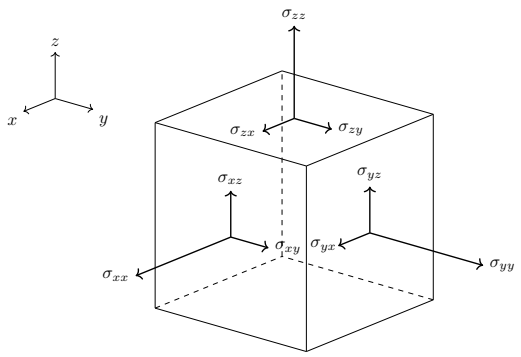

FIGURE 3.3: Illustration of the stress tensor. The stress tensor of a unit volume consists of three symmetric components (σ_{xx}, σ_{yy}, and σ_{zz}), describing forces perpendicular to the surfaces and 6 other components tangential to the surfaces.

3.3.1 Elastodynamic wave equation

Following Yilmaz (Yilmaz, 2001), consider an infinitesimally small volume around a point in a solid medium, and 3D cartesian coordinates (x, y, z). When a force is applied to the volume, the resulting stress, which is also defined as a force per unit area, can be described through the stress tensor σ:

$$\sigma_{ij} = \begin{pmatrix} \sigma_{xx} & \sigma_{xy} & \sigma_{xz} \\ \sigma_{yx} & \sigma_{yy} & \sigma_{yz} \\ \sigma_{zx} & \sigma_{zy} & \sigma_{zz} \end{pmatrix} \tag{3.18}$$

Here, σ_{xx} is, for example, the stress normal to the surface lying in the y-z plane, i.e., pointing in x-direction, while σ_{xy} and σ_{xz} are tangential to that surface. The same definitions hold true for the other matrix elements. In general, the first subscript denotes the direction of normal to the surface, and the second subscript denotes the direction of the stress described by this tensor component. This is schematically shown in Figure 3.3. Respecting conservation of angular momentum (Malvern, 1969; Goldstein, 2011), the stress tensor is symmetrical, i.e., $\sigma_{ij} = \sigma_{ji}$.

The relation between stress and deformation can be expressed through the linearised Hooke's law:

$$\sigma_{ij} = c_{ijkl} e_{kl}. \tag{3.19}$$

Here, the strain tensor e_{kl} is defined as

$$e_{ij} = \frac{1}{2}(\partial_i u_j + \partial_j u_i). \tag{3.20}$$

where c_{ijkl} is the elasticity tensor and ∂_i describes the derivative of the deformation of the solid with respect to coordinate i. Since strain and stress tensor share the same symmetry, c is also symmetric in the first two indices, i.e., $c_{ijkl} = c_{jikl}$. Furthermore,

energy considerations imply symmetry for the first and the last index (Aki, 1980):

$$c_{ijkl} = c_{jikl} = c_{ijlk} = c_{klij}. \tag{3.21}$$

The stress-strain relationship from Equation 3.19 can, therefore, be rewritten as

$$\sigma_{ij} = c_{ijkl}\partial_k u_l. \tag{3.22}$$

Following Backus (Backus, 1970) and Pike and Sabatier (Pike and Sabatier, 2001), the elasticity tensor of an isotropic elastic medium only depends on the two parameters λ and μ, usually referred to as Lamé parameters:

$$\begin{aligned} c_{ijkl} &= \lambda\delta_{ij}\delta_{kl} + \mu(\delta_{ik}\delta_{jl} + \delta_{il}\delta_{jk}) = \\ &= \begin{pmatrix} \lambda+2\mu & \lambda & \lambda & 0 & 0 & 0 \\ \lambda & \lambda+2\mu & \lambda & 0 & 0 & 0 \\ \lambda & \lambda & \lambda+2\mu & 0 & 0 & 0 \\ 0 & 0 & 0 & 2\mu & 0 & 0 \\ 0 & 0 & 0 & 0 & 2\mu & 0 \\ 0 & 0 & 0 & 0 & 0 & 2\mu \end{pmatrix} \end{aligned} \tag{3.23}$$

with the Kronecker delta $\delta_{ij} = 1$ when $i = j$ and $\delta_{ij} = 0$ when $i \neq j$. Inserting Equation 3.22 into Newton's law (Pike and Sabatier, 2001), one obtains the time-domain elastodynamic wave equation for the displacement vector $\mathbf{u}$:

$$\boxed{\rho\ddot{u}_i = \partial_j(c_{ijkl}\partial_k u_l) + f_i,} \tag{3.24}$$

or in the frequency domain

$$\rho\omega^2 u_i + \partial_j(c_{ijkl}\partial_k u_l) = -f_i. \tag{3.25}$$

Here, ρ denotes density and f_i the i component of a vector describing forces such as gravity or seismic sources in the Earth.

3.3.2 Elastic material parameters

The combination of the two Lamé parameters, describing the elasticity of a material, i.e., how a material deforms due to external stress, is quite abstract, and difficult to grasp. Therefore, two other parameters are usually used to describe the mechanical properties of elastic media:

- Young's modulus E, unit: pressure, describes the stiffness of the medium and is calculated by dividing the stress along a specific axis by the strain along the

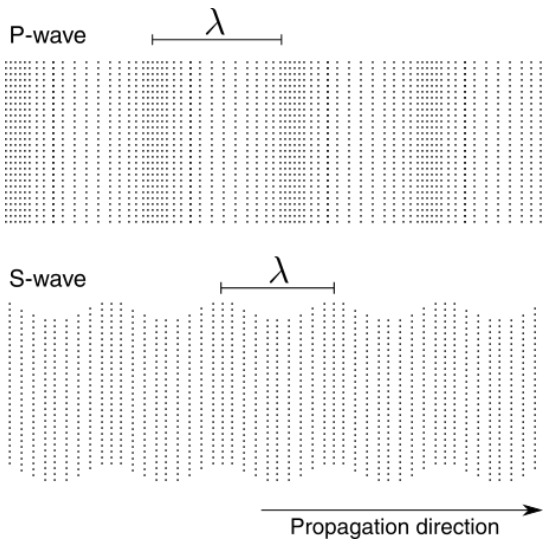

FIGURE 3.4: P-wave and S-wave schemes in 2D. **Top:** P-wave scheme. Particle motion is parallel to propagation direction and consists of alternating compression and dilatation. **Bottom:** S-wave scheme. Particle motion is transversely polarized with respect to propagation direction and consists of alternating transverse motion. This illustration only shows the 2D case, where one polarization of S-waves is possible. In the real world, another polarization perpendicular to the propagation direction is possible, i.e., perpendicular to the surface of this page.

same axis. It relates to the Lamé parameters through

$$E = \frac{\mu(3\lambda + 2\mu)}{\lambda + \mu}. \tag{3.26}$$

- Poisson's ratio ν, unit: dimensionless, is the negative ratio between transverse strain and axial strain. When the medium is stretched in length, it usually contracts in width. For Poisson's ratio of 0.5, the medium contracts by exactly the amount needed for the volume to remain unchanged, limiting the value to this maximum. It relates to the Lamé parameters through

$$\nu = \frac{\lambda}{2(\lambda + \mu)}. \tag{3.27}$$

Body waves, i.e., waves traveling inside a medium, can have three polarizations, since there are three spatial dimensions (Pike and Sabatier, 2001). The fastest (or "primary") P-wave is a longitudinal compressional wave, which is polarized parallel to propagation direction. It is followed by two slower (or "secondary") transverse S-waves, polarized perpendicular to the propagation path, both of them traveling at the same velocity. A schematic illustration of the two types of waves is shown in Figure 3.4. The velocity of these two types of waves can be deducted from the

Young's modulus, Poisson's ratio and density of the material, i.e.,

$$c_P = \sqrt{\frac{\lambda + 2\mu}{\rho}}, \tag{3.28}$$

$$c_S = \sqrt{\frac{\mu}{\rho}}. \tag{3.29}$$

It can be seen from Equation 3.28 and 3.29 that the P-wave velocity c_P is always larger than c_S (roughly 60%):

$$\frac{c_S}{c_P} = \sqrt{\frac{1 - 2\nu}{2(1 - \nu)}}. \tag{3.30}$$

In the absence of shear ($\mu = 0$), such as in a fluid, no S-waves propagate through the medium and the Poisson's ratio ν takes its maximum value of 0.5.

Apart from body waves, there are also surface waves, which travel along the surface of the elastic medium. They are especially interesting for seismology; since they propagate in only two instead of three dimensions, they receive less geometrical spreading and are larger in amplitude than body waves. Ground shaking and damage to structures due to earthquakes is mostly caused by these types of waves (Stein and Wysession, 2009). There are two main types of surfaces waves: Firstly, Rayleigh waves, which travel as ripples similar to those on the surface of water, and, secondly, Love waves, which can be described as horizontal shear waves. Another type of waves which deserves attention is Lamb[4] waves. They propagate along plates of relatively small thickness with respect to the wavelength, and their properties, unlike body waves, are quite complex due to dispersion and multi-mode characteristics (Ing and Fink, 1998). While an infinite medium supports two wave modes (P- and S-wave), plates have infinite pairs of Lamb wave modes, whose velocities depend on plate thickness and frequency. One mode, which is symmetrical about the midplane of the plate, and another, which is antisymmetric about the midplane (Lamb, 1917). Generally speaking, if the thickness of a plate is small compared to the wavelength, Rayleigh waves are a specific type of Lamb waves.

3.3.3 Time reversal using elastic waves

The derivation of TR as a source localization tool was presented in the context of the inhomogeneous acoustic wave equation (Equation 3.3), but can easily be expanded to the elastodynamic wave equation (Equation 3.24 and 3.25), since it is also time-invariant (Manen, Curtis, and Robertsson, 2006; Cassereau and Fink, 1992; Wapenaar and Fokkema, 2006). Hence, TR has grown to become a widely used method in acoustics, with applications to biomedical imaging (Catheline et al., 2008), seismic modeling (Manen, Robertsson, and Curtis, 2005), underwater source localization

[4] They are named after the English mathematician Horace Lamb.

(Edelmann et al., 2002), earthquake localization (Larmat et al., 2006) or transforming everyday objects into tactile objects (Ing et al., 2005). In the framework of this thesis, numerical simulations showed that seismic surface waves could be time-reversed to focus the wave field at the correct earthquake epicenter (Boschi, Molinari, and Reinwald, 2018). This has been achieved through well known surface-wave Green's functions, i.e., robust phase-velocity maps of Rayleigh and Love waves (Kästle et al., 2018), and separating the signals into narrow frequency bands (Tanimoto, 1990; Tromp and Dahlen, 1993). Other studies successfully conducted TR source localization using lamb waves (Ing and Fink, 1998; Park, Kim, and Sohn, 2009; Xu and Giurgiutiu, 2007). Hence, it is not necessary to perfectly measure or numerically compute all waves, barring no wave type that exists in the setup, to make use of TR. However, a thorough understanding of what types of waves are present surely will guide the researcher in interpreting results.

3.4 Computational methods of simulating wave propagation

The physics of wave propagation is described through various partial differential equations as seen in Sections 3.1 and 3.3. However, for complex media, there are no analytical solutions. Solving these equations often requires discretization of the wave field and calculating the solutions using (large) computers. There are numerous methods of numerically simulating wave propagation in 3D elastic media, such as finite-difference schemes (e.g., Igel, Nissen-Meyer, and Jahnke, 2002; Kristek and Moczo, 2003), their optimal operator variants (e.g., Takeuchi and Geller, 2000) or discontinuous Galerkin methods (e.g., Dumbser and Käser, 2006). In the framework of this thesis, there are two in particular that are used via specific software packages: The *finite-element method* (FEM) and the *spectral-element method* (SEM). Both methods will now be introduced in the context of the one-dimensional elastic wave equation. For a more thorough description of the methods and comparisons with other methods, the reader is referred to the excellent textbook of Igel (Igel, 2017). The following mathematical derivations are based on this book.

3.4.1 The finite-element method (FEM)

For the sake of simplicity, consider the one-dimensional version of the elastic wave equation (Equation 3.24), written as

$$\rho \ddot{u} = \partial_x \mu \partial_x u + f. \tag{3.31}$$

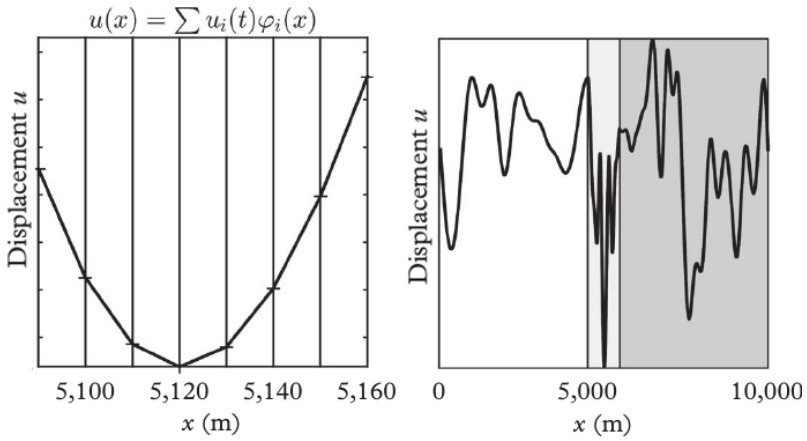

FIGURE 3.5: Principle of finite-element discretization. **Left**: The equation shows the interpolation scheme using the sum over basis functions φ_i. The plot shows a close-up of the displacement field. Vertical lines indicate element boundaries and crosses represent points at which the displacement field is evaluated. Inside the elements the displacement field is described by a linear function. **Right:** The displacement field u during a spectral-element simulation. Different shades of gray represent different wave velocities in the medium. Taken with permission from Igel (Igel, 2017, Figure 6.2).

FEM does not solve the displacement field $u(x,t)$ directly, but instead replaces it by a finite sum over linear basis functions φ_i:

$$u(x) \approx \hat{u}(x) = \sum_{i=1}^{N} u_i(t)\varphi_i(x). \tag{3.32}$$

Here, the unknowns are the coefficients u_i, corresponding to the displacement at node points x_i. Furthermore, the wave equation can be expressed in its weak form (see e.g., Carcangiu, Montisci, and Forcinetti, 2015), multiplying Equation 3.31 by a test function φ_j with the same basis, and integrating over the entire physical domain $\mathbb{V}$. The system of equations then reads

$$\int_{\mathbb{V}} \rho \ddot{\hat{u}} \varphi_j dx + \int_{\mathbb{V}} \mu \partial_x \hat{u} \partial_x \varphi_j dx = \int_{\mathbb{V}} f \varphi_j dx, \tag{3.33}$$

which needs to be solved for the approximate displacement field $\hat{u}$. Using finite differences to replace the time derivative, and considering appropriate initial conditions, e.g., $\mathbf{u}(t=0) = 0$, the solution of the displacement vector $\mathbf{u}$ at the next time step $t + dt$ can be calculated through

$$\mathbf{u}(t+dt) = dt^2 (\mathbf{M}^T)^{-1} \left[\mathbf{f} - \mathbf{K}^T \mathbf{u}\right] + 2\mathbf{u}(t) - \mathbf{u}(t-dt). \tag{3.34}$$

Here $\mathbf{M}$ and $\mathbf{K}$ are mass and stiffness matrices, respectively. An illustrative example of a 1D FEM simulation is shown in Figure 3.5. In a nutshell, FEM requires the user to 1) divide the domain in a finite number of elements, which are connected through

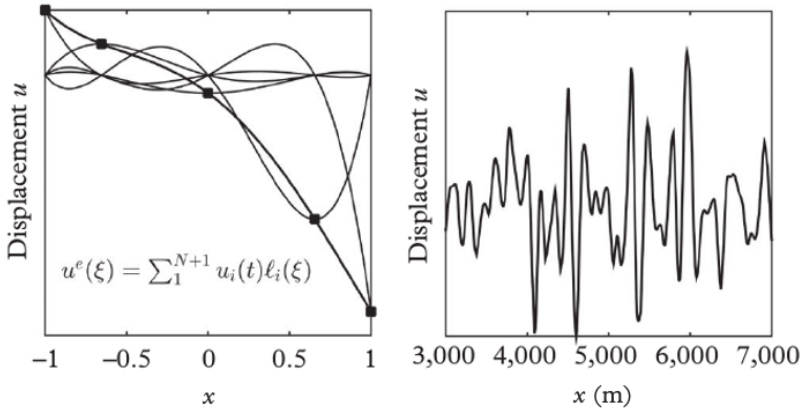

FIGURE 3.6: Principle of spectral-element discretization. **Left**: The equation shows the interpolation scheme using Lagrange polynomials. The plot shows a close-up of the displacement field inside one element. The solution at all 5 points (black dots) is exactly interpolated using Lagrange polynomials. **Right**: The displacement field u during a spectral-element simulation. Taken with permission from Igel (Igel, 2017, Figure 7.3).

nodes, 2) assign each node specific material parameters, and 3) solve the complete system of linear equations. A very detailed discussion about the theory of FEM is written by Zienkiewicz and Taylor (Zienkiewicz and Taylor, 2005), but is not part of this thesis.

3.4.2 The spectral-element method (SEM)

SEM, which is a special form of FEM, is currently one of the most widely used numerical methods for wave propagation simulations. One of the reasons is that it solves one of the most significant problems of FEM, the large linear system of equations, by using a specific set of basis functions; the basis functions φ_i are chosen to be the Lagrange polynomials $\ell(\xi)$ with N points per element and space variable ξ:

$$\varphi_i \rightarrow \ell_i^{(N)}(\xi) := \prod_{k=1,k\neq 1}^{N+1} \frac{\xi - \xi_k}{\xi_i - \xi_k} \tag{3.35}$$

The spacing of these points is not regular but is shaped by collocation points called Gauss-Lobatto-Legendre (GLL) points. These points make integration easy by using Gauss quadrature. Straight-forward parallelization of the algorithm (instead of complicated matrix inversion techniques) is possible by using interpolation and integration schemes for the mentioned GLL points (Igel, 2017). One of the essential advantages of these points is that the mass matrix that needs to be inverted becomes diagonal (see Equation 3.34), which makes inversion very efficient and quick (as long as the elements are rectangular in 2D, or hexahedral in 3D). The result is that SEM algorithms are incredibly efficient and highly parallelizable.

Figure 3.6 shows a snapshot of a 1D displacement wave field simulated with SEM on the right. The left picture shows the approximation of the unknown displacement function u, i.e., a zoom into the displacement field, by a sum over Lagrange polynomials of a fourth order, i.e., 5 points per element. The higher the order, the more points inside the element at which the solution is exactly calculated (Reinwald, 2015).

Chapter 4

Super-resolution in near-field acoustic time reversal

This chapter is a research article submitted under the title *Super-resolution in near-field acoustic time reversal using reverberated elastic waves in skull-shaped antenna* to the journal Acta Acustica united with Acustica in 2018. The full text of the article is reproduced here with no addition and no modifications except in the form.

This chapter discusses the potential of elastic waves propagating in a skull-shaped object for near-field acoustic time reversal by reconstructing sound source positions at below-wavelength distances. The resolution is compared with the theoretical far-field diffraction limit.

Summary

Signals are recorded by passive sensors glued on a replica of a human skull, measuring solely its mechanical vibrations, and not sensitive to airborne sound. The sound source is placed along the horizontal and median plane at distances to the skull between 5 and 100 cm. Source positions are reconstructed for signals with frequencies in the physiological hearing range with a resolution indirectly proportional to the distance between source and skull across all measurements in the far-field. Measurements in the near-field show -3 dB widths smaller than half a wavelength (super-resolution) with highest resolutions of down to $\lambda/15$ measured in front of the orbital cavities. It is suggested that anatomical details give rise to complex features of the skull's Green's function, that in turn enhance resolution in a direction-dependent manner.

4.1 Introduction

It is well known (Benade, 1990) that anatomy contributes to the task of auditory source localization, as its effects on an acoustic signal, described by the head-related transfer function (HRTF) (Wenzel et al., 1993; Hu et al., 2016), can be seen as a spectral filter and depend on the location of the signal's source. Human auditory source localization mostly relies on differences in the phase and amplitude of signals perceived by the two ears, as well as "spectral cues", or frequency-dependent effects associated with the shape of the pinnae and, possibly, other features of the body (Van Opstal, 2016).

Building on the work of Catheline et al. (Catheline et al., 2007), we explore here the specific role of elastic waves mediated in a skull-shaped object mimicking bone-conducted sound. While this study does not address the issue of whether and how bone conducted sound is employed by the human auditory (ears/brain) system, our goal is to determine whether these reverberated signals contain specific information about the reconstruction of the position of an auditory source, especially in the near-field. This could be relevant to current efforts in the study of bone conduction sound (Wazen et al., 2001; Walker et al., 2005; Stenfelt, 2011; Littler, Knight, and Strange, 1952; Stenfelt and Goode, 2005). Using the principle of acoustic time reversal (Fink, 1999; Fink, 2006), we convert the signal recorded by two receivers into the spatial coordinates of a source in the horizontal and sagittal plane, and evaluate the resolution with which the source position is thus reconstructed.

Catheline et al. (Catheline et al., 2007) showed via a time reversal experiment with a dry skull that in-skull elastic wave propagation provides information about spatial positioning of a sound source. They found that their time reversal algorithm, using elastic waves alone, received at two or only one recording transducer mimicking the ear, successfully reconstructed the source position(s), for single as well as multiple sources. The spatial resolution of this method was found to decrease with increasing distance between the skull and the sound source. This is in good agreement with the far-field diffraction law, which provides a relationship between the spatial resolution and the distance separating the antenna (skull) from the source. Our objective is to expand the early work of Catheline et al. (Catheline et al., 2007) and Ing et al. (Ing et al., 2005) to (1) analyze the resolution of the same algorithm for a skull-shaped antenna specifically in the near-field, i.e., the sound source is placed closer than one wavelength to the skull, and (2) to evaluate the directionality of the algorithm, i.e. evaluate changes in resolution with respect to angular position of the sound source.

In this study, we conduct a suite of experiments on a simple setup, equivalent to the setup used in Catheline et al. (Catheline et al., 2007), consisting of two recording transducers glued to a replica human skull. Sound is generated by a small speaker deployed at a variety of distances and azimuths. Our results show in particular that, in the near-field, the resolution with which we reconstruct the source position

changes as a function of azimuth with respect to the skull and is clearly influenced by complex features of the skull such as the orbital cavities. Furthermore we achieve super-resolution throughout all angles for sources very close to the skull.

Similarly minded experiment have been conducted in recent years e.g. in the context of optics, where imaging with evanescent waves allows to surpass the classical diffraction limit; the super-resolution of near-field microscopes is piloted by their probe size (Pohl, Denk, and Lanz, 1984; Lewis et al., 1984). In this context, a source (Hell and Wichmann, 1994; Dickson et al., 1997; Betzig, Trautman, et al., 1991) or scatterers (Errico et al., 2015) smaller than a wavelength, placed within the medium can be detected in the far-field with super-resolution as well. Time reversal experiments can also surpass the diffraction limit when resonators are placed near a source (Lerosey et al., 2007; Rupin, Catheline, and Roux, 2015) or when an acoustic sink is used (Rosny and Fink, 2002). To a lesser degree, near-field details can sometimes be extracted from the far-field using sophisticated algorithms such as inverse filter (Conti, Roux, and Kuperman, 2007) or MUSIC (Simonetti, 2006). Experiments with metamaterials, super-lenses and hyper-lenses (Pendry, 2000) demonstrate moderate sub-diffraction imaging down to a quarter of the optical wavelength. All these techniques use different terminology but they all require some near-field measurements.

Because very few studies in psychoacoustics have explored human sound localization performances for nearby sources (Parseihian, Jouffrais, and Katz, 2014), we are unable to determine whether the resolution achieved by our algorithm reproduces the performance of human listeners using bone conducted sound. While we do find that elastic waves contain sufficient information to successfully reconstruct source positions in the near-field, we cannot yet establish whether a similar capability is achieved by the human auditory system.

4.2 Methods

The experimental setup is based on the previously conducted experiment of Catheline et al. (Catheline et al., 2007): We use a skull-shaped object (for simplicity from now on called skull) made of the epoxy resin. The skull is mounted on a rotatable rod with a reference (horizontal) plane chosen approximately as a plane passing through the area of the ethmoid bone above the vomer and through the zygomatic arch and process of the temporal bone. A conventional loudspeaker (RS Pro TRG040008) is deployed sequentially at a discrete set of positions in the horizontal and vertical plane. The loudspeaker shows a flat frequency response between 200 Hz and 8 kHz. The distance between the source (loudspeaker) and the skull (the point on the surface of the skull closest to the speaker), denoted D, varies from 5 to 100 cm, while the source position at each distance varies with angle φ between -50° (i.e. down,left) and +50° (i.e. up, right). The experiment is conducted in an anechoic chamber. Equipment

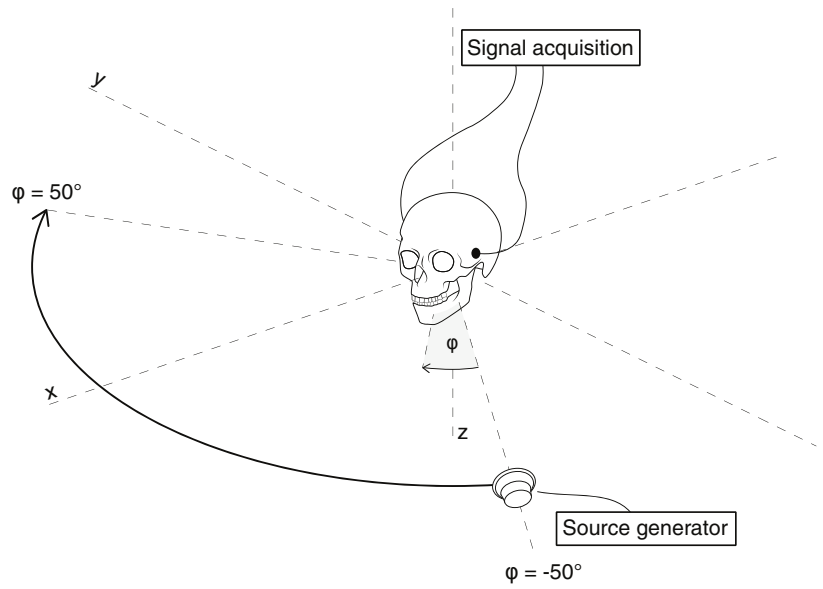

FIGURE 4.1: Sketch of the experimental setup in the horizontal plane. A loudspeaker is connected to a source generator (PC) and emits a chirp signal at each angle φ ranging from -50° to 50° along a half circle at various distances to the skull. The resulting vibration of the skull is recorded through two passive sensors glued to the hypothetical ear locations. They are connected to the signal acquisition system, consisting of a sound card connected to a PC.

which could possibly reflect sound is covered with multiple layers of sound dampening material. Two passive sensors (Murata PKS1-4A), with a working bandwidth ranging between 100 Hz and 15 kHz and a diameter of 1 cm, are glued close to the hypothetical ear locations on both sides of the skull. They are used as receivers to record the elastic vibrations and are connected to a sound card (Soundscape SS8IO-3) which has a 140 dB dynamic range and a 44.1 kHz sampling frequency.

A sketch of the experimental setup in the horizontal plane is shown in Figure 4.1.

We checked that the sensors solely measure the vibration of the skull and are unresponsive to airborne sound. This ensures that the time reversal algorithm will utilize only elastic waves. Additionally, the influence of the foam platform used to place the loudspeaker at certain distances has been tested to have no influence on sound emission of the loudspeaker.

The first part of the experiment consists of recording the signals at the sensors for each speaker position. The speaker emits a chirp signal $c(t)$ with a duration of 1 s and a linear frequency distribution between 0 Hz and 6 kHz. The function in time for such a chirp of duration T, minimum frequency f_0 and maximum frequency f_1 reads

$$c(t) = sin\left[\Phi_0 + 2\pi\left(f_0 t + \frac{k}{2}t^2\right)\right], \tag{4.1}$$

with the initial phase Φ_0 at time $t = 0$ and the chirpyness $k = \frac{f_1 - f_0}{T}$ (in our case

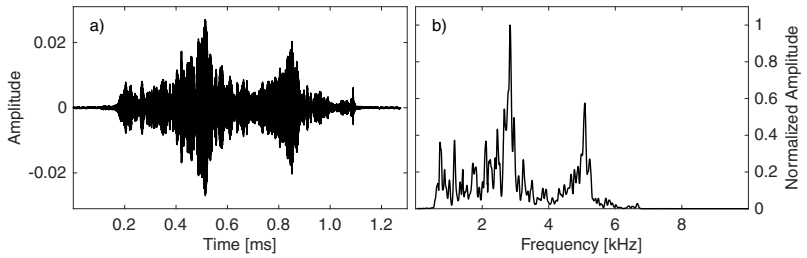

FIGURE 4.2: **a)** Exemplary waveform of a recorded signal at one of the sensors. **b)** Frequency spectrum of the same signal.

$k = 6000Hz/s$), also known as the rate of frequency range across the chirp. For each distance D the source positions in the horizontal plane are defined by the azimuth φ.

The recorded signal s at one of the sensors' location r, writes

$$s(\varphi_0, r, t) = c(t) * G(\varphi_0, r, t), \tag{4.2}$$

where $*$ denotes convolution, φ_0 is the source position (azimuth) and $G(\varphi_0, r, t)$ is the acoustic impulse response of the skull, which is also the Green's function of the signal emitted at φ_0 and recorded at r, assuming without loss of generality that emitter and receiver are punctual. A representative waveform of a signal recorded with one of the sensors and its normalized frequency spectrum is shown in Figure 4.2. Note that the spectra of all impulse responses (only one shown here) show strong similarity to the results from Catheline et al. (Catheline et al., 2007) where a real dry skull was used and its resonance frequencies were confirmed with other studies of dry skulls and cadaver heads (Stenfelt and Goode, 2005; Håkansson et al., 1994). This proves that, in the first approximation and for the purposes of our study, the epoxy skull replica employed here is sufficiently similar to a real skull. It should be noted that, firstly, epoxy can have mechanical properties similar to those of bone tissue (Bernard, Grimal, and Laugier, 2014; Bernard et al., 2016); secondly, the most important role in our experiments is presumably played by the outer shape of the skull, driving wave propagation in air around the skull: and the replica is designed to have realistic external shape.

Following Fink (Fink, 2001), the received signal $s(\varphi_0, r, -t)$ is time-reversed, i.e flipped with respect to time. It must then be backward propagated to any possible location φ_i. This is equivalent to convolving $s(\varphi_0, r, -t)$ with the Green's function $G(\varphi_i, r, t)$. Since we do not have access to $G(\varphi_i, r, t)$, but we do have a library of recordings of $s(\varphi_i, r, t)$ for all possible values of φ_i, we implement

$$\begin{aligned} T_i(\varphi_0, r, t) &= s(\varphi_0, r, -t) * s(\varphi_i, r, t) = \\ &= c(-t) * G(\varphi_0, r, -t) * c(t) * G(\varphi_i, r, t). \end{aligned} \tag{4.3}$$

The term $G(\varphi_0, r, t) * G(\varphi_i, r, -t)$ is the transfer function of such a time reversal

algorithm and, in terms of signal analysis, represents a matched filter (Fink, 2001). This convolution coincides with the cross-correlation of $G(\varphi_0, r, t)$ and $G(\varphi_i, r, t)$ ((Draeger and Fink, 1999; Derode et al., 2003)). For each source position φ_0, the signal processing procedure consists of implementing Equation 4.3, i.e. analytically cross-correlating the signals, and of finding the maximum value, with respect to time, of the time-reversed wave field T_i for each φ_i. The resulting function $F(\varphi_i)$ is dubbed "spatial focusing function" (shortly, focusing function), as this procedure is equivalent to evaluating whether (and with what resolution) the time-reversed and backward-propagated wave field is able to reconstruct the original source position φ_0. The focusing function is next normalized with respect to its maximum; It is then reasonable to assume that, the closer $F(\varphi_i)$ is to 1 (i.e., identical Green's functions) for a given value of φ_i, the closer φ_i is to the original source φ_0. This method can be interpreted as a pattern recognition system, that identifies, from an acoustic reference library, the Green's function corresponding to the actual position of the source, and so determines the position of the source.

The invariance under time reversal is lost if the propagation medium has frequency-dependent attenuation. This introduces a first-order time derivative in the governing propagation equation. However, the theorem of spatial reciprocity is still valid, i.e. there is a loss of amplitude in the time-reversed vs. forward propagating wave field, but this does not affect source-localization resolution (does not affect the location of the focus of the time-reversed wave field) provided that signal-to-noise ratio of recorded data is sufficiently high. We have accordingly chosen to carry out our experiments at frequencies that are well caught by our receiving system. We take both sensors into account by computing the mean of the focusing functions of the two signals. In order to investigate the role of different frequency contents, the originally measured signals are successively filtered with varying low-pass filters with maximum frequency f_{max}.

Following e.g. (Ing et al., 2005; Blomgren, Papanicolaou, and Zhao, 2002; Tsogka and Papanicolaou, 2002), we estimate the spatial resolution of our time reversal algorithm by analyzing the -3 dB width Δp of $F(\varphi_i)$ for each given source position (angle φ and distance D between the source position and the skull) and various smallest wavelengths $\lambda_{min} = c/f_{max}$ (with c = speed of sound in air). We compare our resolution estimates against the apparent aperture A of our skull-shaped antenna, as defined by Catheline et al. (Catheline et al., 2007), through the far-field diffraction law

$$A = \frac{D \cdot \lambda_{min}}{2\Delta p}. \tag{4.4}$$

While resolution as defined here is known to follow the diffraction-law in the far-field (Catheline et al., 2007), that is not the case in the near-field, where Equation 4.4 is only used here for the sake of comparison.

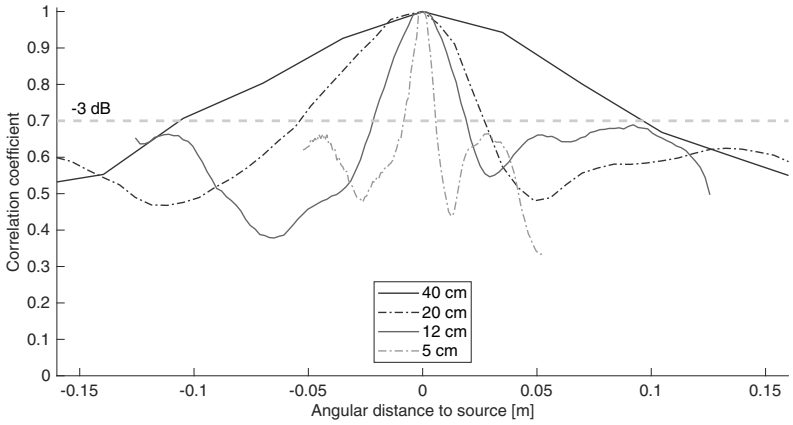

FIGURE 4.3: Normalized focusing functions along the curvilinear abscissa for sources in front of the center of the skull ($\varphi = 0°$) and at different distances to the skull. The distance of the measurement points to the skull decreases from 40 cm, down to 20 cm, 12 cm and 5 cm (different curves). There is a clear trend of increasing resolution (decreasing -3 dB width of the curves) with decreasing distance.

4.3 Results

4.3.1 Verification of diffraction law

In this section, we reproduce the results of Catheline et al. (Catheline et al., 2007) and verify that our far-field data are consistent with the diffraction law (Equation 4.4). The source position is chosen to be at $\varphi = 0°$, which is in front of the center of the skull. We calculate the normalized focusing function $F(\varphi_i)$ along the curvilinear abscissa in the horizontal plane as described previously, for each distance to the skull. This is shown in Figure 4.3 as a function of the curvilinear abscissa. The -3 dB (correlation coefficient of 0.7) widths of the curves are in good agreement with the diffraction law, confirming the findings of Catheline et al. (Catheline et al., 2007), where the width of the curve is directly proportional to the distance between skull and sound source. Additionally it can be seen that the maximum peak to ground level (frequently named contrast) of our time reversal scheme lies below -3 dB. This has been confirmed for all measurements and ensures that calculating the resolution is not hindered by a low-contrast focusing function. Figure 4.4 shows the -3 dB widths of the focusing functions of the signals for sources with different maximum frequencies f_{max} and at different distances in front of the skull ($\varphi = 0°$). We calculate the values of A using Equation 4.4 and the values shown in Figure 4.4. They are found to be approximately 10 cm for all distances and maximum frequencies proving that the apparent aperture in the far-field is independent of distance or maximum frequency.

Measurements in the sagittal plane (not shown here) show smaller slopes of the linear fits evaluated in the same way as in Figure 4.4 across all results. Compared

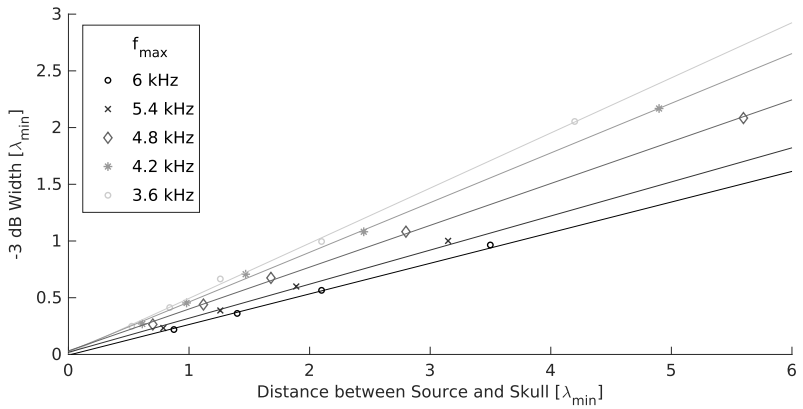

FIGURE 4.4: -3 dB width values of the focusing functions for sources at different distances to the skull (x-axis) and maximum frequencies f_{max} of the signal. The slope of each linear fit, which corresponds to the apparent aperture A in Equation 4.4, is approximately 10 cm for all curves.

to the case of the horizontal plane, therefore the apparent aperture size is larger for these measurements (15 cm). This may be related to the different diameters of the skull, close to 10 and 15 cm, in the horizontal and sagittal planes, respectively.

The measurement points in the near-field (at distances smaller than one wavelength) lie on the same linear fit (i.e. same apparent aperture) as the points for measurements in the far-field although Equation 4.4 does not hold true in the near-field. In the near-field, i.e. for sources closer than one minimum wavelength away from the skull, source positions can still be resolved with the same angular resolution which results in super-resolution in space, i.e. -3 dB widths below 0.5 λ_{min} (see Figure 4.4). While one could infer that the diffraction limit also holds true in the near-field, our results are purely empirical; any values below the previously formulated diffraction limit are not represented in Equation 4.4. We speculate that they can be ascribed to the near-field contribution of evanescent waves.

Our far-field data is in agreement with Equation 4.4 and the previous findings of Catheline et al. (Catheline et al., 2007). In addition, we are able to achieve the same angular resolution as stated in the far-field diffraction law in the near-field (sound sources at below-wavelength distances) leading to super-resolution.

4.3.2 Directional variation in resolution

We furthermore investigate the directional variation of resolution of the time reversal analysis in the horizontal plane. The angular variations in resolution of our time reversal scheme in the near-field are visualized in Figure 4.5 showing the values of A (top) and Δp (bottom) with respect to the source azimuth φ for different source distances (5 cm, 12 cm and 20 cm and 100 cm). All data is filtered to have a maximum frequency of 3 kHz. The reason for an offset of around $2-3^\circ$ to the center ($\varphi = 0^\circ$)

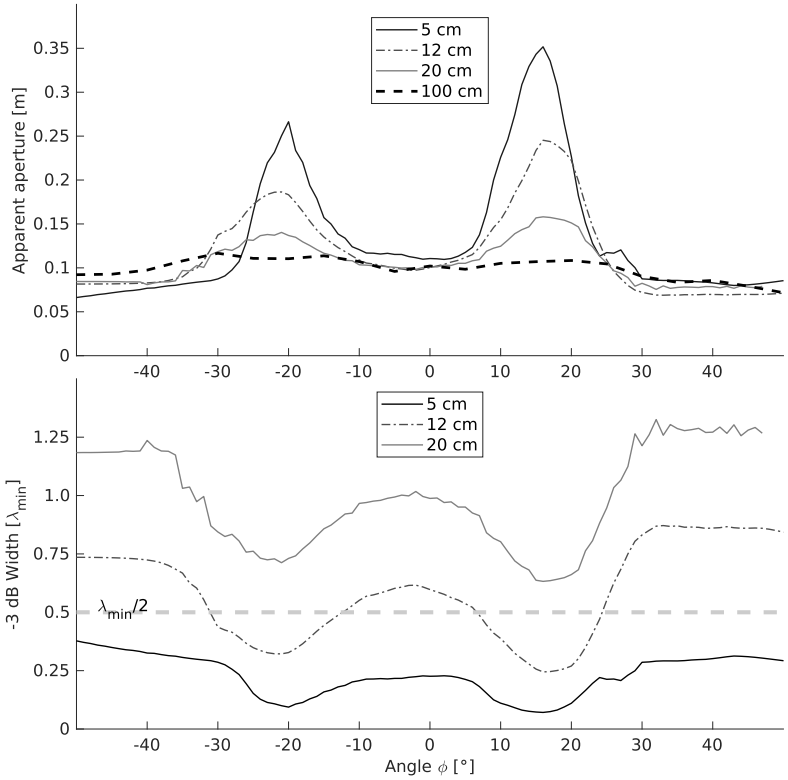

FIGURE 4.5: Angular variations of resolution for different source distances. **Top:** Variation in apparent aperture for different source distances. Maxima are at -20° and 15° whereas the values decrease for source positions close to the center and further away from the center. **Bottom:** Variation in -3 db widths for different source distances. Super-resolution is accomplished throughout all angles at a distance of 5 cm and for certain angles at a distance of 12 cm. Highest resolution (smallest -3 dB width) is accomplished for source positions directly in front of the orbital cavities. This effect is (relatively) enhanced the closer the source to the skull.

is due to a limited accuracy in the manual placement of the center position and the center of the rotation axis.

In the far-field, the apparent aperture does not vary with azimuth (see 100 cm data in Figure 4.5) and is equal to the value of 10 cm obtained from Figure 4.4 throughout all far-field measurements at source azimuth $\varphi = 0°$.

In the near-field, the largest apparent aperture values lie roughly in front of the two orbita, at -20° and 15°, and are up to more than three times larger compared to the aforementioned far-field value, whereas source positions in front of the nasal bone or along the process of the temporal bone show values closer to 10 cm. The closer the source to the skull, the more prominent the angular directionality of the apparent aperture. Hence, the maximum apparent aperture is more than three times larger than the skull diameter in the horizontal plane.

-3 dB widths are smaller than half a wavelength (super-resolution) throughout all azimuths at a distance between source and skull of 5 cm, down to $\lambda_{min}/15$ (i.e. for φ =-20° and 15°). This shows that the skull-shaped antenna enables sub-wavelength focusing of near-field sources and, furthermore, anatomical details of the skull may give rise to differences in resolution at certain positions due to the presence of evanescent waves. They can be described as a non-propagative spatial fluctuation field that decreases exponentially over roughly one wavelength (Rosny and Fink, 2007) and can be created at a boundary between two media through certain incident angles of a propagating wave (Fink, 1992). Usually, their effect is not measured in the far field and the far-field diffraction law (Equation 4.4) does not account for such effects, limiting the resolution of time reversal. However, if near-field components of the wavefield are measured and incorporated in the time-reversal algorithm, sub-wavelength information, that is carried by evanescent waves, is incorporated in the time-reversal process, leading to super resolution (Lerosey et al., 2007).

All these results are also approximately achieved via a one-sided evaluation of the signals, i.e. when only one receiver is used.

In summary, our data shows large variations in resolution in the near-field, depending on the position of the source relative to the geometric complexities of the skull.

4.4 Conclusion

In this study we measured elastic wave signals in a replica of a human skull due to an incident airborne sound emitted by a source at various distances and orientation with respect to the skull. Our goal was to investigate the physical limits of a sound-localization algorithm that uses full waveform information and the information contained in elastic waves propagating in the skull bone. While we do not at all claim to directly reproduce the sound localization "algorithm" that exists in the

human ear-brain system, our quantification of these limits may be considered as a point of comparison in near-field psychoacoustics experiments.

We showed that the resolution of a time reversal scheme using a skull-shaped antenna with one or two receivers is consistent with the diffraction law in the far-field. The apparent apertures in the horizontal and sagittal planes are roughly consistent with the horizontal and vertical extent of the skull. Interestingly, the apparent aperture in the near-field is markedly increased (more than 3 times its value in the far-field) in the horizontal plane and at specific angles. In that case we can achieve super-resolution that may be associated to the non-negligible contribution of evanescent waves in the near-field.

Our results suggest that anatomical details of the skull give rise to complex features of the radiated sound field in the near-field, enabling sub-wavelength focusing and directional changes in resolution. We clearly find the influence of small anatomical geometric complexities such as the orbital cavities to positively influence resolution using elastic waves. We believe that it will be useful, in future studies, to explore the performance of our algorithms in other frequency ranges and for other biological models (e.g., echolocating species such as dolphins or bats).

As noted by Parseihian et al. (Parseihian, Jouffrais, and Katz, 2014), very few studies in psychoacoustics have explored human sound localization performances for nearby sources (e.g., Brungart, Durlach, and Rabinowitz, 1999). It appears to us that further experimental work is needed to more robustly evaluate how well humans localize nearby sources and if our findings can be related to psychoacoustic studies in the near-field.

Acknowledgements

This project has received funding from the European Union's Horizon 2020 research and innovation programme under the Marie Sklodowska-Curie grant agreement No 641943 (ITN WAVES).

Chapter 5

3D model of a dolphin skull and the skull-related transfer function

This chapter presents the various steps in creating a 3D model of the skull of a common dolphin, such as scanning the specimen and segmenting the scans. A suitable set of material parameters that best describes the vibrational response of the mandible is determined through experimental and numerical modal analysis. The model is then used in frequency-domain numerical simulations using the finite-element method to determine the influence of bone-conducted sound on sound pressure levels at the two ear positions. More precisely, the question is answered if the skull of a dolphin alone can induce salient spectral notches, as pinnae do in humans, that the animal could use to differentiate source elevations in the median plane.

Summary

The skull specimen is scanned via an industrial micro CT scanner. The resulting images are segmented to define the extents of the bone. Here, mandible and cranium, as well as the teeth, are considered to be isotropic and homogeneous for easier meshing and decreased computational cost. A comparison between numerical and experimental modal analysis results in a suitable set of material parameters that, applied to the 3D model of the mandible, lets the model vibrate and bend at similar resonant frequencies as the real mandible. Frequency-domain finite-element modeling is used to compute the skull-related transfer function of the modeled skull in the median plane. Depending on how bone tissue is modeled, sound pressure levels computed at the ears vary largely. Adding acoustic waves to a previously rigid mandible increases sound pressure levels mostly for positive source elevations and frequencies larger than 10 kHz. Further incorporating shear waves increases sound pressure levels coming directly from the front of the skull. However, no clear spectral notches, which could explain the dolphin's ability to differentiate source elevations, are found in the skull-related transfer function. Either soft tissues, which have not been incorporated in this study, introduce such cues, or dolphins possess indeed auditory processing techniques not known to humans.

5.1 Introduction

As a terrestrial species, humans are designed to live in an inherently two-dimensional space. Accordingly, they have evolved indirect and simple auditory cues to localize sound sources in the horizontal plane via intensity and time differences between the two ears (see Chapter 2). In the median plane, i.e., the plane that separates the left from the right half of the head, these cues are absent. Humans are able to localize median-plane sources (Middlebrooks, 2015), with much poorer accuracy in comparison with horizontal-plane ones (Wettschurek, 1973; Perrott and Saberi, 1990; Nachtigall, 2016). The only way we can differentiate different source elevations is through the direction-dependent spectral filtering of our anatomy. Growing up as an individual, the human brain has learned to associate the frequency of certain simple notches in the HRTF (see Figure 2.5), caused by the asymmetry of the pinna, with certain elevations (Brown, 1994; Batteau, 1967).

Despite the absence of pinnae, dolphins have been shown to be equally sensitive to changes in the elevation or azimuth of signals similar to their echolocation clicks (Renaud and Popper, 1975). Being able to localize sources independently of their position with very high accuracy would provide a large selective advantage to a marine mammal (Branstetter and Mercado III, 2006), but dolphins would require a highly salient HRTF to explain this phenomenon. Sound would have to reflect off, or diffract through different structures of varying densities and celerities, producing frequency-dependent spectral notches, but a "pinna analog" in a dolphin's head has yet to be found.

This study investigates the acoustic response of a skull (mandible and cranium) of a short-beaked common dolphin (*Delphinus Delphis*). In a first step, the skull is modeled in 3D, and the assigned material parameters are validated using modal analysis of the mandible. Then, the model is used to calculate sound pressure at the two ear positions. More precisely, the question is answered if the skull of a dolphin alone can induce salient spectral notches, as pinnae do in humans (see Chapter 2), that the animal could use to differentiate source elevations in the median plane. In this thesis, the spectral colorations of sound due to the skull are termed *skull-related transfer function* (SRTF), since it represents how the skull spectrally filters the sound. This term can be seen as an analog to the HRTF.

In the framework of this chapter, the skull is modeled in three different ways to isolate and compare the influence of certain types of bone-conducted sound waves. As discussed in Chapter 3.3, compressional as well as shear waves are present in an elastic medium. The SRTF is calculated either considering both compressional and shear waves (elastic case), or only compressional waves (acoustic case), or no waves at all (rigid case). A comparison between the elastic, acoustic, and rigid case can quantify the relevance of elastic waves on sound pressure distribution in the vicinity of the ears and the resulting SRTF.

The increase in computational power in the last 20 years and, consequently, the ability to create large-scale realistic 3D models has led to new findings on sound propagation pathways in marine mammals' heads; Aroyan showed that the anatomical structure of the pan bones and mandibular fats in the head of a common dolphin focuses certain sounds towards the ear positions, but the numerical study was limited to compressional waves, i.e., no shear waves were modeled in the bones (Aroyan, 2001). Cranford carried out vibro-acoustic finite-element simulations on a head of a Cuvier's beaked whale (Cranford, Krysl, and Hildebrand, 2008), using a toolkit presented in earlier work (Krysl, Cranford, and Hildebrand, 2008). Their results showed a complex wave propagation pattern including flexural waves along the mandible bone that likely contributes to the received pressure at the two ears. However, the question remained unanswered if these waves are present due to the elastic nature of the bone. Krysl and Cranford calculated HRTFs for only three frequencies and with highly varying results depending on the point of evaluation at the ears (Krysl and Cranford, 2016).

5.2 COMSOL Multiphysics

All simulations in this chapter are conducted using the Acoustics and the Acoustic-Structure Interaction modules of the commercial finite-element software package COMSOL Multiphysics® (Comsol, 2018). This software houses a finite-element code, capable of solving complex physical problems. It supports transient, eigenfrequency, frequency domain, modal analysis, and boundary mode analysis in acoustic and solid media and solves the system of differential equations using numerical solvers such as *PARDISO* (Schenk et al., 2001), which is based on LU decomposition of the mass matrix.

5.3 Creating a 3D model of the skull

Creating 3D models of real-life objects requires a complex workflow, including numerous software packages. The goal, here, is to create a 3D model of the skull (cranium and mandible) of a short-beaked common dolphin and to find a suitable set of material parameters. The typical workflow of such a task is shown in Figure 5.1. Each of these steps is presented within the scope of modeling the dolphin skull.

5.3.1 X-ray CT scan and segmentation

Scan the skull: The specimen - the skull of a short-beaked common dolphin - was received on loan by the National Museum of Natural History, known in French as the Muséum national d'Histoire naturelle (MNHN), and scanned at the x-ray tomography platform "AST-RX", installed in the MNHN. Since operating, AST-RX has been

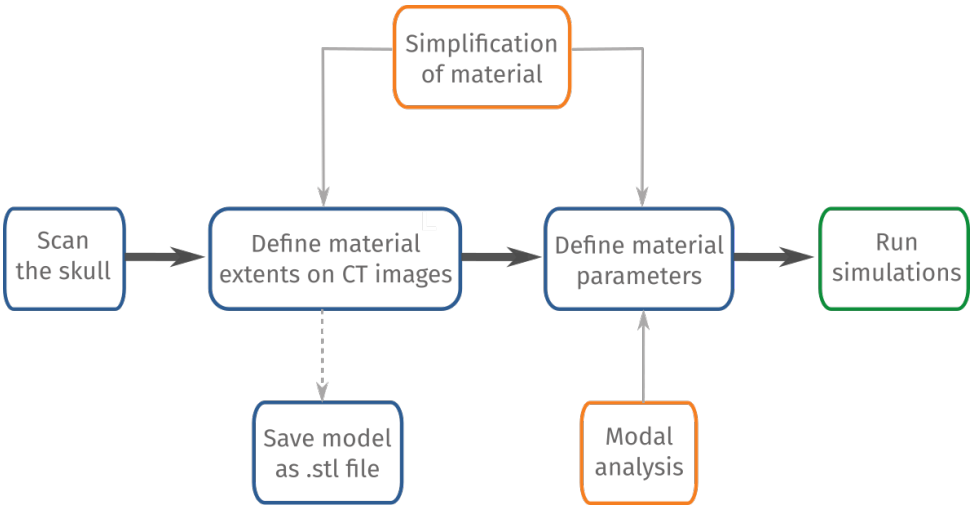

FIGURE 5.1: Work flow of 3D modeling. This scheme illustrates the different steps (blue) needed to create a 3D model of a real-life object and the various considerations that need to be incorporated (orange).

used by researchers to scan various objects, such as organs, insects, meteorites, and bones (Sanz et al., 2013). The platform's equipment consists of a "v|tome|x L 240-180" industrial micro CT scanner, which is a versatile high-resolution system for 2D X-ray inspection and 3D computed tomography, manufactured by GE Sensing & Inspection Technologies® (see Figure 5.2). The dolphin skull was scanned on this machine with a microfocus RX source at 240 kV/320 W, detector 400x400 mm, and a matrix of 2024x2024 pixels. Scan parameters were as follows: voltage = 150 kV; current = 310 μA; exposure: 333 ms. Data were reconstructed using datos|x reconstruction software (Phoenix|x-ray, release 2.0), and exported into a 16-bit TIFF image stack of 4106 virtual slices in coronal view. Each slice has a square voxel size of 200 μm. An example of the resulting raw images is shown in the top panel of Figure 5.3. The voxels obtained by a CT scan are displayed in grayscale, according to the relative radiodensity, i.e., mean attenuation, of the tissues. Less attenuating media are shown bright, whereas more attenuating media are shown dark.

Define material extents on CT images: The next step is to segment the images and define the extent of the bone material. Segmentation can be seen as the process of assigning a material label to every pixel in an image. However, this step already requires knowledge of the capabilities of the software used in later steps and about the material itself; bone can, e.g., feature high porosity and variations in density. Usually, the shaft of long bones is made of very dense, cortical, bone, whereas the center is comprised of cancellous, trabecular, bone (Currey, 2013). One of the fundamental questions in bone modeling is to what degree porosity and density differences can and should be modeled. In this work, bones and teeth are simplified to an isotropic elastic material, without porosity or varying density. This has several reasons: if

FIGURE 5.2: External view of the "v|tome|x L 240-180" industrial micro CT scanner, MNHN, Paris. Image taken from Sanz et al. (Sanz et al., 2013).

cortical bone, trabecular bone, and teeth were modeled separately, the required discretization of finite elements in the later simulation steps would result in many more elements, sometimes of very small volume at complex geometric areas. Increasing the number of elements, i.e., the degrees of freedom of the system, drastically increases computational time. Also, tiny features, several orders of magnitude smaller than the wavelength, most likely do not affect the vibrational response of the mandible. Hence, 3D models for FEM should be simplified as much as possible (Lu, 2013). An example of how a slice is segmented into "bone domain" and "acoustic domain" is shown in the bottom panel of Figure 5.3. After segmentation, the same software package (Materialise Mimics®) is utilized for the 3D reconstruction of the model. A photograph of the real mandible, and a visualization of the final 3D model as a result of segmentation and 3D reconstruction is shown in Figure 5.4. The resulting 3D model does not contain material parameters, textures, or any other information other than the three-dimensional shape of the object, and is saved as a .stl file. STL, which is an abbreviation of "stereolithography", is a file format that only contains the surface geometry of the object through unstructured triangulated elements and their vertices in a Cartesian coordinate system (Burns, 1993). The same procedure (scanning and defining material extents), using the same simplifying assumptions, is simultaneously done for the cranium.

5.3.2 Modal analysis (Experimental vs Computational)

Define material parameters: Once the 3D model is created (and saved), one needs to define the type of material and its mechanical properties. The parameters that are used depend on the softwares' capabilities, as well as on the simplifying assumptions

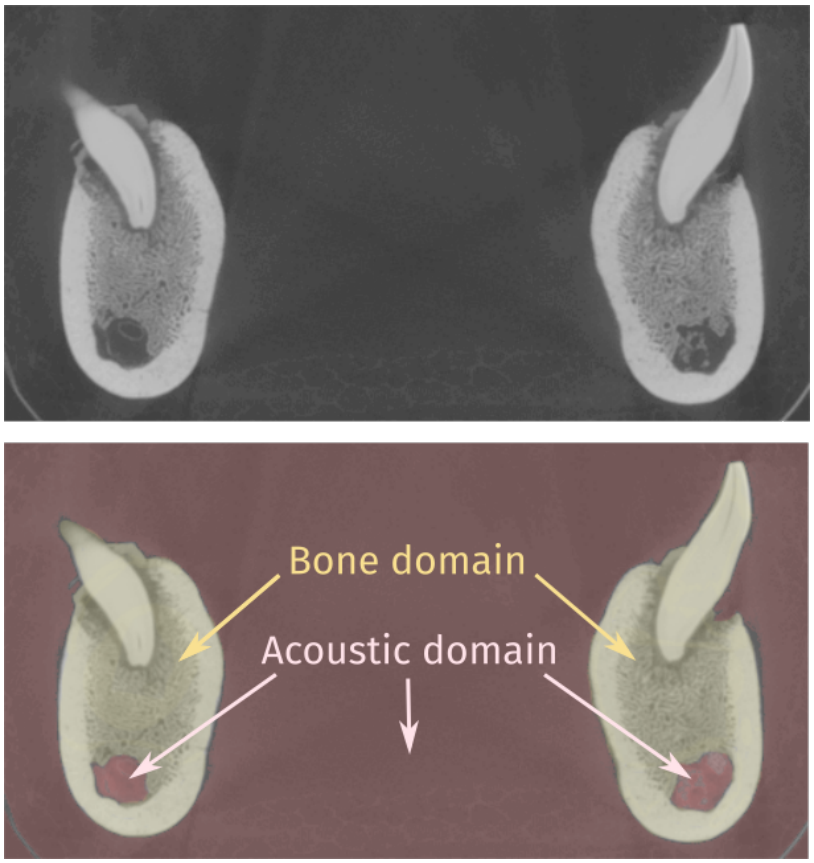

FIGURE 5.3: Segmentation of the bone. **Top:** Coronal slice through the two sides of the mandible bone, including teeth. Density differences between trabecular and cortical bone are visible in different grayscales. **Bottom:** Using the same slice as above, the mandibular foramen, which is usually filled with fats, is modeled acoustic (red), whereas all parts of the bone, as well as the teeth, are modeled solid (yellow).

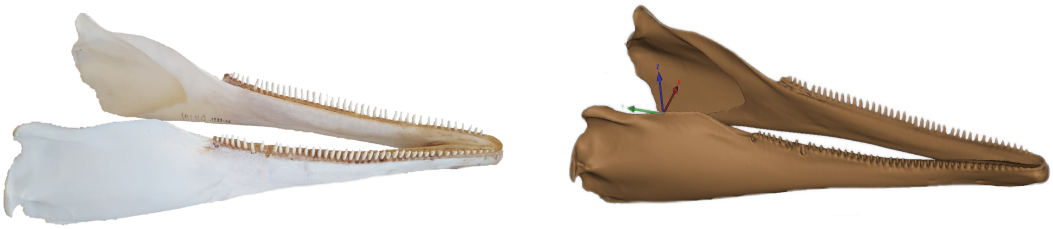

FIGURE 5.4: Comparison between real mandible and 3D model. **Left:** Cropped photograph of the real mandible. **Right:** Visualization of the 3D model. Teeth and bone are considered to be a homogeneous, isotropic medium. The model captures all essential parts of the geometry of the real mandible.

TABLE 5.1: Material parameters from other studies

Material Parameter	(Krysl and Cranford, 2016)	(Cranford et al., 2014)	(Song et al., 2016)
Young's modulus [GPa]	20	15	21.27
Poisson's ratio	0.2	0.2	0.21
Density [kg/m^3]	2600	2000	2000

that are made. Considering an isotropic elastic material as previously defined, the material can be described by the parameters presented in Section 3.3.2, in particular: Young's modulus E, Poisson's ratio ν, and density ρ. There have been quite a few studies modeling bony structures of the head of a dolphin as an isotropic elastic medium, but, surprisingly, the material parameters which have been used vary largely; while some studies entirely neglect the elastic properties of the bone, and model the skull as an acoustic medium (Aroyan et al., 1992; Wei, Zhang, and Au, 2014), others use notably different values (Krysl and Cranford, 2016; Song et al., 2016; Cranford et al., 2014), as listed in Table 5.1.

The goal of the following analysis is to find the best set of material parameters, which models the bone in a way so that it behaves similarly to the real skull. Considering the simplified geometry of the model, the object of this study is not to determine the material parameters of the bone.

One of the fundamental properties of a structure reflecting material properties is its eigenmodes. An eigenmode, or normal mode, is the natural vibration of an object such that all parts move at the same frequency and with a fixed phase relation. The frequencies at which this motion takes place are known as the object's resonant, or normal frequencies, since small external forces at these frequencies can resonate and produce large amplitude oscillations of the object[1]. The word "normal" refers to the mathematical definition of orthogonality, i.e., the modes are orthogonal to each other. This means that the vibration of an object in one mode will never excite another (Zienkiewicz and Taylor, 2005). Finding these eigenmodes is usually referred to as "modal analysis" and carried out using FEM or via measurements of the vibration of the object due to external excitation. A thorough description of the theory of modal analysis using FEM and experiments can be found in Appendix A.

Resonant frequencies of the mandible are measured experimentally using a SIMO (single-input, multiple-output) approach; a small impact hammer induces an excitation by striking the mandible and releasing force as fast as possible. Ideally, the excitation resembles an impulse, which would result in a flat spectrum of the force signal throughout all frequencies. This property is convenient for modal analysis because the object would then vibrate in all frequencies, but strongest in its resonant frequencies. It has been shown that, while hammer strikes are not able to recreate a

[1] In 1940, the Tacoma Narrows Bridge in Washington, USA, collapsed due to aeroelastic flutter. The wind blew at one of the resonant frequencies of the bridge, resulting in the disastrous collapse (Petroski, 1985).

perfect impulse, they do an excellent job of inducing large enough amplitudes in a wide range of frequencies, suitable for modal analysis of small and light structures (Lu, 2013; Packard, 1997). The vibration of the object can be measured by accelerometers or laser vibrometers. Depending on where the hammer struck, and where the vibration is measured, some modes may not be seen, because either impact or receiver position lies on the nodes of an eigenmode. One can avoid this problem by repeating hammer strikes or measuring the vibration at multiple positions. It has been suggested in the literature that only changing one of the positions, e.g., only striking the hammer at many positions, is enough to accurately describe the vibrational response of the object and find the fundamental resonant frequencies (Avitabile, 2001).

In the framework of this work, three different sets of material parameters, taken from Table 5.1, are applied to the 3D model of the mandible. Each set was used in other computational work on dolphin heads but differed from each other notably in at least one parameter. Eigenmodes are calculated via the software package COMSOL®. In the following, the calculated eigenmodes are described by the respective motion of the mandible. They are identical for each material parameter set and only differ in the calculated resonant frequencies. Then, for each set of material parameters, the resonant frequencies are compared with experimentally obtained values to determine the best choice of material parameters so that the numerical model of the mandible bends and vibrates similar to the real mandible.

The shape of the mandible is rather simple; it can be described as a hollow rod, bent in the center and flattened at the ends. Such an object surely has distinct low-frequency eigenmodes. Just imagine holding a dowsing rod; bending the rod by pressing the two ends closer to each other and then releasing pressure describes one of the eigenmodes of such an object. Four distinct low-frequency eigenmodes of the mandible are found in the simulations. The first, shown in Figure 5.5, exactly describes the motion described for the dowsing rod. The other three are shown in Figures 5.6-5.8. In all four figures, the motion of the mandible is depicted in the two instants of maximum deformation and a difference phase of 180°.

For the experimental modal analysis, the mandible is suspended in a free-free condition through fine strings at the tip. The excitation source is a manually induced impulse via an impact hammer (*Brüel & Kjaer* Type 8203), which is connected to a PC oscilloscope (Picoscope Type 5444-B) that measures the force signal of the impact. Three miniature charge accelerometers (*Brüel & Kjaer* Type 4374) are glued to the mandible, and are also connected to the same oscilloscope. Signals are converted to acceleration and amplified through a conditioning charge amplifier (*Brüel & Kjaer* Type Nexus 2692-A). For each strike with the hammer, the data acquisition system stores the signal of the impact (source) and the vibration of the mandible measured by the accelerometers (signal) with a sampling rate of 2 MHz. A photograph of the experimental setup is shown in Figure 5.9, and a screenshot of what can be seen on

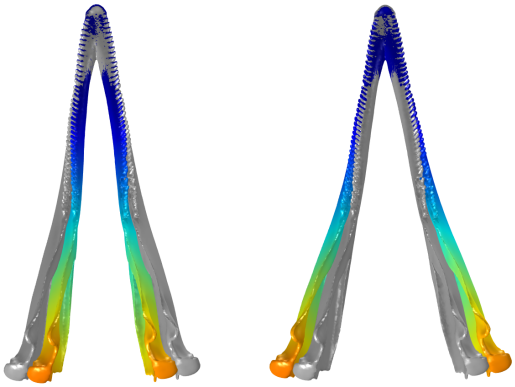

FIGURE 5.5: Motion of the mandible at the first calculated eigenmode. The two ends move contrary to each other in the horizontal plane.

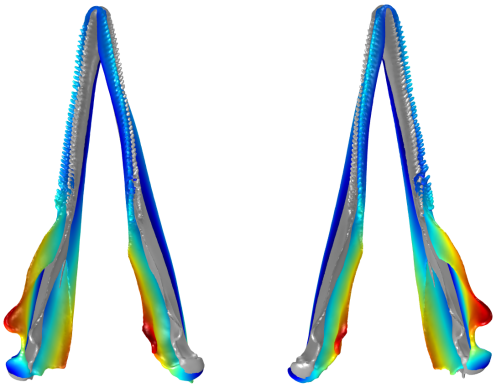

FIGURE 5.6: Motion of the mandible at the second calculated eigenmode. Symmetric torsion of the two ends around the longitudinal axes of the two arms of the mandible.

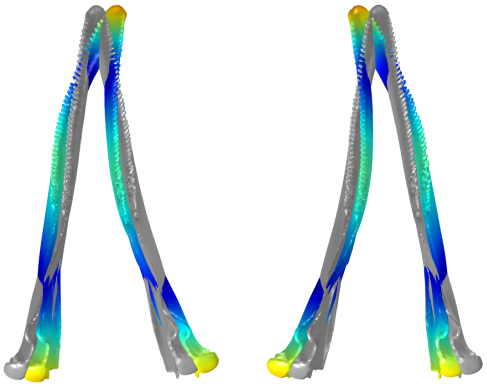

FIGURE 5.7: Motion of the mandible at the third calculated eigenmode. The mandible bends in the horizontal plane through same-directional motion of the tip and the ends

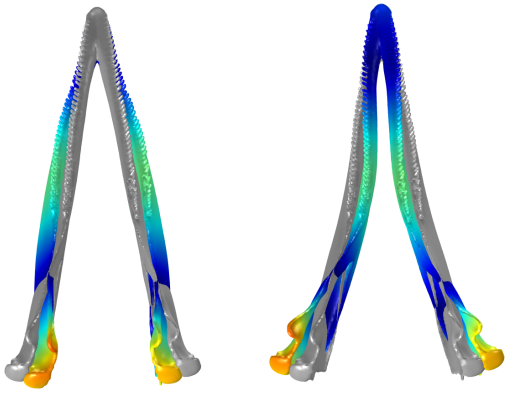

FIGURE 5.8: Motion of the mandible at the fourth calculated eigenmode. The mandible bends in the horizontal plane through opposite-directional motion of the center and the ends.

the acquisition screen after a hammer strike is shown in Figure 5.10. Signals are recorded for 16 different impact positions, repeating the same strike ten times for each position. The impact and accelerometer positions are shown in Figure 5.11. The *frequency-response function* (FRF) $h(f)$ for each strike position and one of the three accelerometers can then be obtained by averaging the spectra of the ten recorded signals and removing the effect of the limited bandwidth of the strike, i.e.,

$$h(f) = \frac{1}{10} \sum_{i=1}^{10} \frac{s_i(f)}{y_i(f)}. \tag{5.1}$$

Here, $s_i(f)$ are the spectra of the signals and $y_i(f)$ are the spectra of the hammer strikes. Subscript i iterates over ten signals which are averaged to obtain one FRF. The experimentally measured FRFs for all strike and accelerometer positions are shown in Figures 5.12- 5.14, each Figure showing the results for one accelerometer. High amplitude peaks correspond to the natural frequencies. It is obvious that each FRF has its own shape, and some modes are not excited with certain combinations of source and receiver positions. However, there is overwhelming evidence in the data that, as expected, there are four distinct resonant frequencies of the mandible at 44, 142, 283, and 315 Hz (red lines in Figures 5.12-5.14). Some missing modes can be explained by the positions of the impact, and the respective mode shape; Point #6, which lies on the center of the "arms" of the mandible does not show modes 1 and 2. This observation makes sense, considering the motion of the respective modes, showing no displacement at this point (Figure 5.5,5.6). The same holds true for Point #8 which is located at the tip of the mandible and, therefore, does not show any motion for the first two eigenmodes.

The next logical step is to compare the experimentally measured resonant frequencies with the ones obtained from simulations. A comparison of these values is shown in Table 5.2. The best correlation of resonant frequencies is found with the

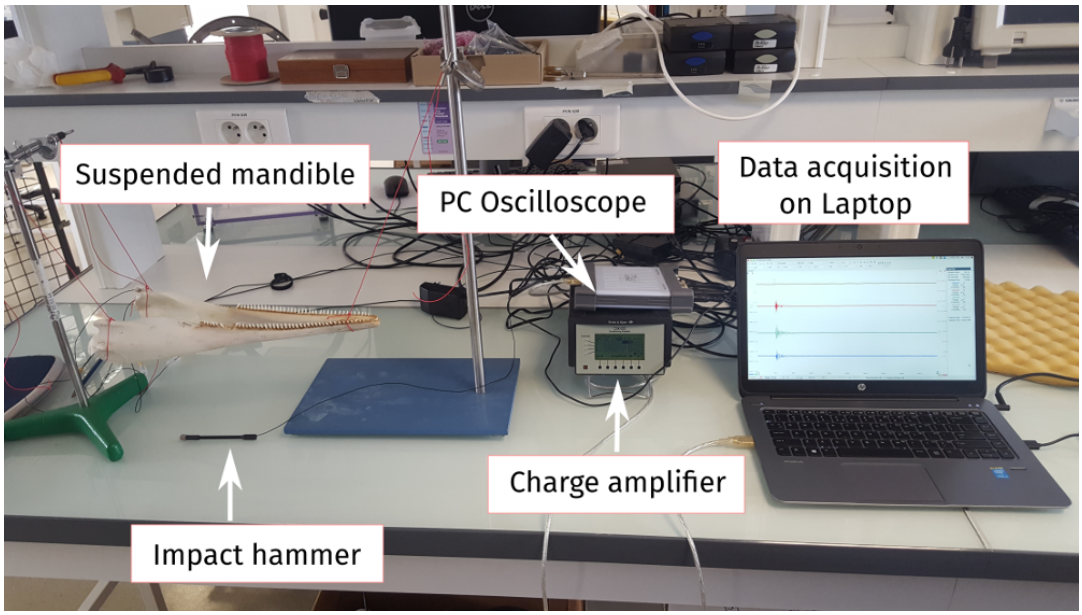

FIGURE 5.9: Photograph of experimental setup. The necessary equipment for experimental modal analysis consists of the object to be tested (suspended mandible), the impact hammer, a PC oscilloscope to record the data, a charge amplifier to amplify the signals and a laptop for data acquisition.

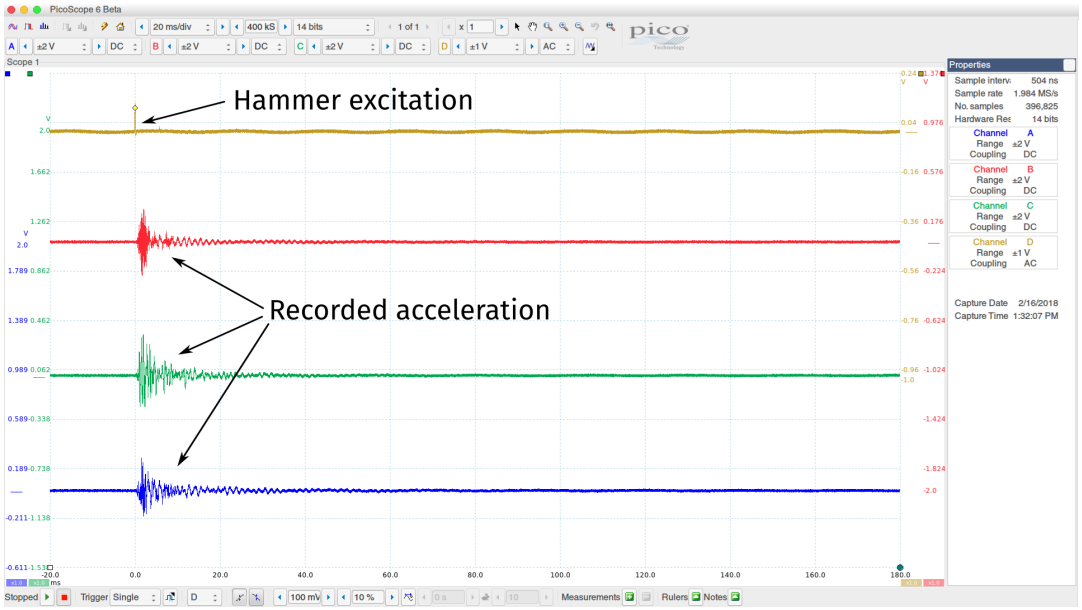

FIGURE 5.10: Screenshot of the GUI used for data acquisition. The GUI of the software package "PicoScope 6" shows the waveform of the hammer excitation (light brown), and of the three accelerometers. Furthermore, it lets the user set the sampling rate, duration of the recorded signals and trigger method.

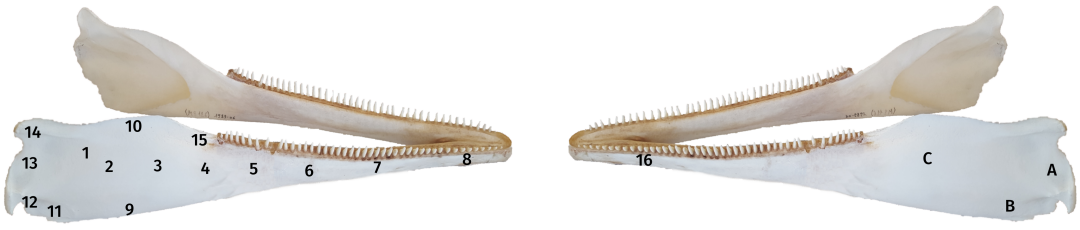

FIGURE 5.11: Excitation and accelerometer positions. The mandible is struck with a hammer on 16 different positions (numbers 1-16). Accelerometers are glued to three positions (letters A-C).

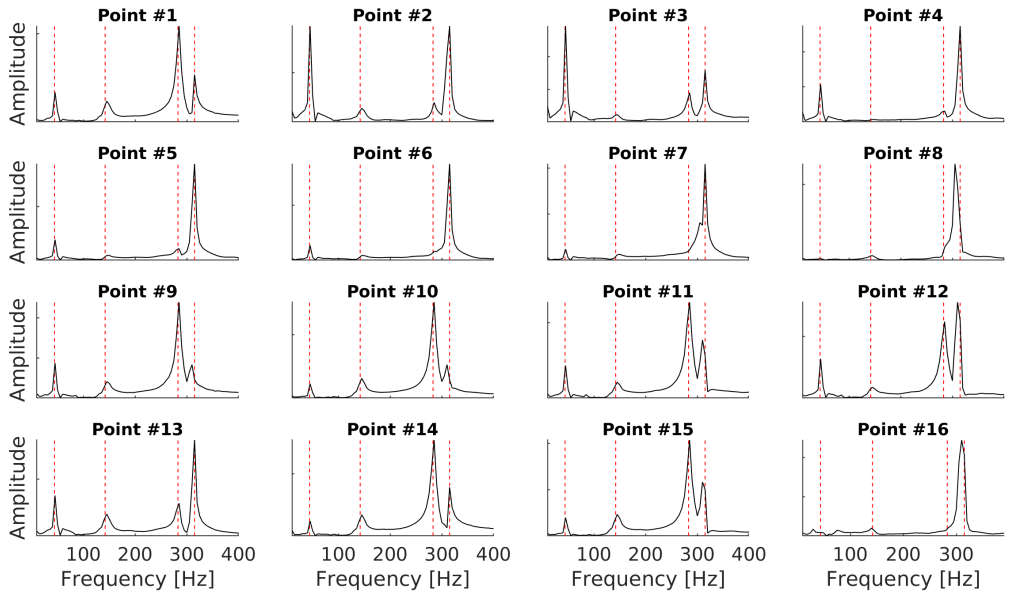

FIGURE 5.12: Frequency response functions for all impact points 1-16 and accelerometer position A show four prominent peaks at 44, 142, 283, and 315 Hz (red lines).

TABLE 5.2: Experimental and numerical resonant frequencies

Mode	Experiment	(Krysl and Cranford, 2016) (Error)	(Cranford et al., 2014) (Error)	(Song et al., 2016) (Error)
1	44 Hz	44.6 Hz (1.2%)	38.51 Hz (12.4%)	49.7 Hz (13.0%)
2	142 Hz	160.0 Hz (12.6%)	157.6 Hz (11.0%)	203.9 Hz(43.6%)
3	283 Hz	285.2 Hz (0.8%)	220.9 Hz (22.0%)	312.1 Hz (10.3%)
4	315 Hz	341.0 Hz (8.2%)	264.1 Hz (16.1%)	388.0 Hz (23.2%)

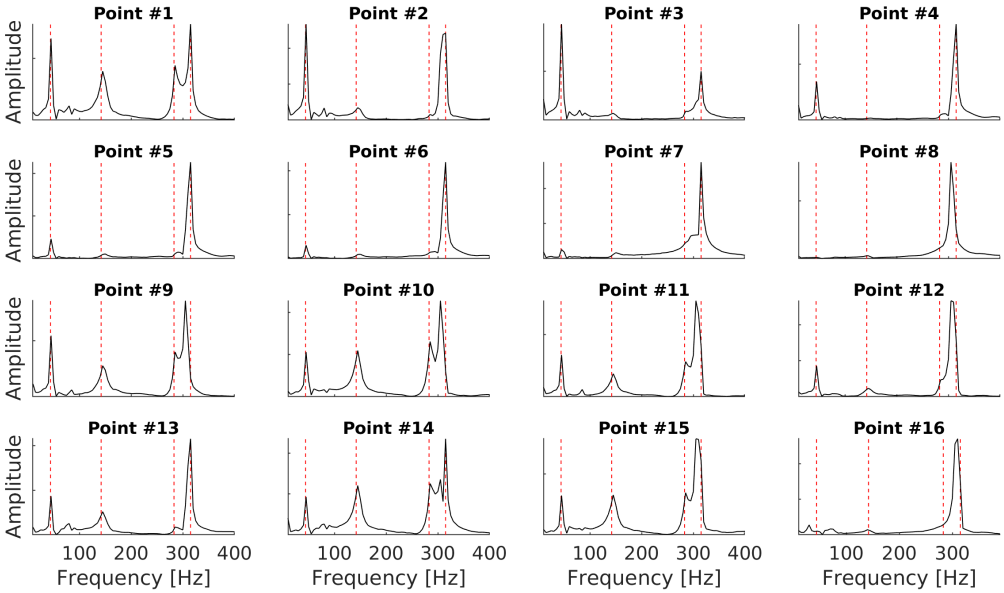

FIGURE 5.13: Same as Figure 5.12 but for accelerometer position B.

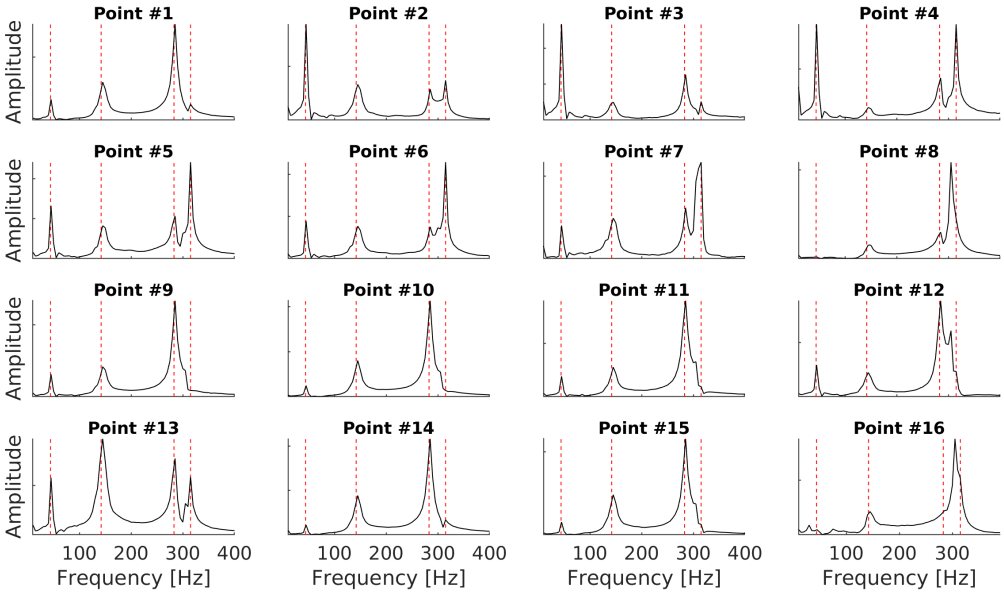

FIGURE 5.14: Same as Figure 5.12 but for accelerometer position C.

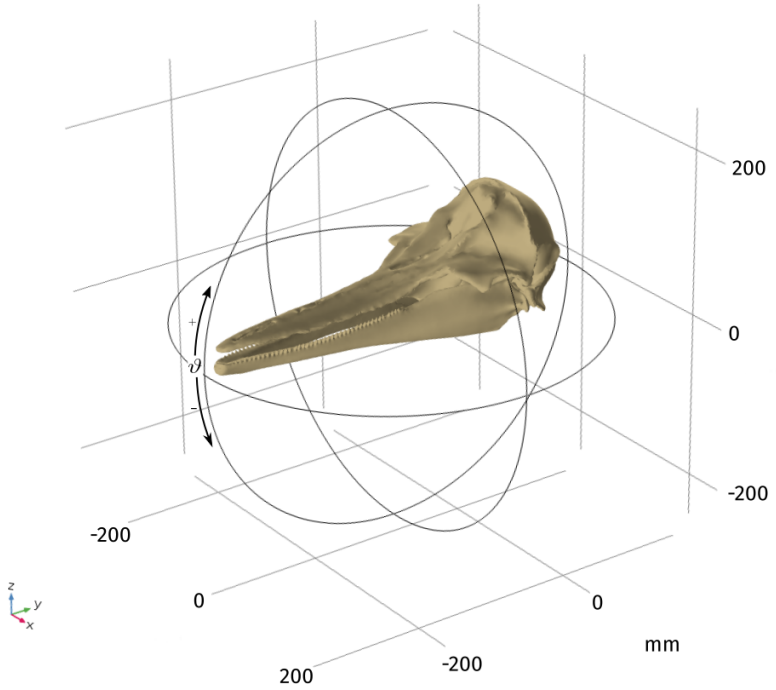

FIGURE 5.15: Geometry of the simulation domain. The skull (brown) lies in the center of a sphere (black wireframe).

parameters from Krysl and Cranford. Surely, with more time and research at hands, a more sophisticated model could be made, which then more precisely recreates the eigenmodes of the real bone. For the framework of this thesis and the limitations due to the computational complexity of FEM, the material parameters of the best fitting model are chosen and applied to the 3D model. Let's recall Figure 5.1: Finding a suitable set of material parameters, including experimental verification through modal analysis is the final step in the process. Despite the somewhat simplified mechanical properties, the created 3D model does not only resemble the shape of the real mandible but also bends and vibrates similarly. Following Krysl et Cranford, the chosen parameters are also applied to the cranium, assuming similar bone structure and density.

5.4 Skull-related transfer function in the median plane

The model is now used in frequency-domain finite-element simulations to compute the skull-related transfer function in the median plane.

5.4.1 Simulation domain

The simulation domain is defined as an acoustic sphere, with a radius of 250 mm, surrounding the skull as shown in Figure 5.15. The entire domain is meshed using a

free triangular mesh, limiting the maximum element size to 3 mm in water, and 1 mm in bone, ensuring at least six elements per smallest wavelength. Each simulation has 22 million degrees of freedom and runs for approx. 30 minutes on two CPUs of type Intel(R) Xeon(R) CPU E5-2695 v3 using two sockets and 28 cores in total.

5.4.2 Governing equations

On the outer spherical perimeter of the water domain, i.e., the shell of the sphere, an incident monotonous and continuous plane wave is prescribed. The acoustic pressure p is defined as

$$p = p_0 e^{-i\mathbf{k}\mathbf{x}} e^{-\alpha \mathbf{x}} \tag{5.2}$$

with wave vector $\mathbf{k}$, position vector $\mathbf{x}$ in 3D space, and attenuation coefficient α =0.025 Np/(MHz·m) (Li et al., 2015; Jensen et al., 2009). The maximum pressure amplitude p_0 of the plane wave is set to 1 Pa and absorbing boundary conditions are imposed. This condition ensures that there are no scattering effects due to the boundary of the sphere.

The incident plane wave is set to have frequencies between 2 and 76 kHz (spacing of 2 kHz), arriving from various elevations ϑ (between -90° and 90°, spacing of 5°). Here, $\vartheta = -90°$ is below, $\vartheta = 90°$ above, and $\vartheta = 0°$ directly in front of the skull.

Sound pressure in the water domain is modeled by means of the Helmholtz equation, which is equivalent to Equation 3.3, i.e.,

$$\frac{1}{\rho}\nabla^2 p + \frac{\omega^2 p}{\rho c^2} = 0, \tag{5.3}$$

with angular frequency ω, density $\rho = 1000\,\mathrm{kg/m^3}$, and speed of sound c = 1483 m/s. Wave propagation in the bones and the coupling between bone and water domain is simulated in three different ways:

- In what is dubbed the *elastic case*, bones are defined as isotropic elastic media, which requires specification of their density, Young's modulus, and Poisson's ratio. Coupling at acoustic/solid interfaces is implemented by setting the boundary load $\boldsymbol{F}$ (force/unit area) on the acoustic/solid boundaries to $\boldsymbol{F} = -\boldsymbol{n}_s p$, where $\boldsymbol{n}_s$ is the outward-pointing unit normal vector seen from inside the solid domain. On the fluid side, the normal acceleration experienced by the fluid is required to coincide with the normal acceleration of the solid, i.e.,

$$-\boldsymbol{n}_a \cdot (-\frac{1}{\rho_0}\nabla p) = a_n \tag{5.4}$$

where $\boldsymbol{n}_a$ is the outward-pointing unit normal vector seen from inside the acoustics domain, and the normal acceleration a_n is equal to $(\boldsymbol{n}_a \cdot \boldsymbol{u}) \cdot \omega^2$, where $\boldsymbol{u}$ is the calculated harmonic-displacement vector of the mandible. In this case, there are

TABLE 5.3: Material parameters for different bone models

Material parameter	Elastic and attenuated	Elastic	Acoustic	Rigid
Density [kg/m^3]	2600	2600	2600	-
Poisson's ratio	0.2	0.2	-	-
Young's modulus [GPa]	20	20	-	-
Speed of sound [m/s]	-	-	2923	-
Q factor	30	-	-	-

two variants, one including and the other neglecting attenuation in bone. Attenuation is introduced through the Q factor, modeling intrinsic frictional damping of the material (Dimarogonas, 1996; Lazan, 1968).

- In the *acoustic case*, bones are defined as acoustic media; compressional waves in the medium are described through Equation 5.3. Boundary conditions that ensure correct coupling between water and bones are applied.

- In the *rigid case*, no waves are allowed waves to travel through the bones and the acoustic/solid interface is regarded as a rigid wall; the bones are not affected by sound, but the presence of the structure will nonetheless affect sound pressure in water. This behavior is achieved by setting a fixed constraint on all the solid boundaries, that is, $\boldsymbol{u} = 0$. This reduces the above condition ($a_n = 0$) to the sound rigid boundary condition

$$\boldsymbol{n}_a \cdot (-\frac{1}{\rho_0}\nabla p) = 0. \tag{5.5}$$

A list of parameters values that were assumed in each case is shown in Table 5.3. In all cases, the resulting *sound pressure level* (SPL) in dB, which describes the diffracted field, is defined in the acoustic domain as

$$SPL = 20 \cdot log_{10}(\frac{p_{rms}}{p_{ref}}). \tag{5.6}$$

Here, p_{rms} is the root mean square (rms) of pressure p over one cycle and $p_{ref} = \frac{1}{\sqrt{2}} = \approx 0.707$ Pa is the rms pressure due to the incident plane wave pressure $p_0 =$ 1 Pa. This value consequently sets the SPL to 0 dB in the case of a freely traveling plane wave without acoustical interference with an object. Therefore, the scalar SPL quantifies the increase (positive SPL) or decrease (negative SPL) of pressure due to waves interacting with the bones. In the following, SPLs are calculated by the average SPL over the surface of cubes of 8 cm^3, positioned at the hypothetical locations of the TPCs, i.e., the ears, and shown in Figure 5.16.

The spectrum of the SPL for each elevation at each ear is the corresponding SRTF since it represents how the skull spectrally filters the sound.

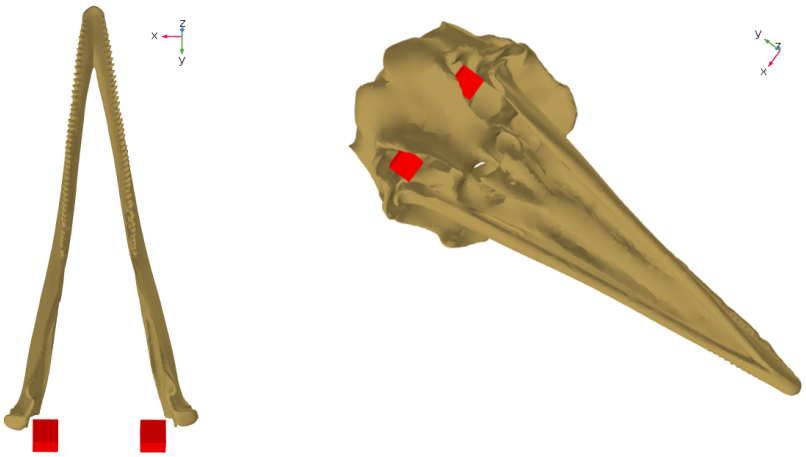

FIGURE 5.16: Boxes (in red) are placed at the approximate positions of the TPCs. SPLs are averaged over the surface of these boxes.

5.4.3 Results

An example of a SPL distribution for the elastic and attenuated case is shown in the right panel of Figure 5.17, corresponding to a simulated plane wave seen in the left panel of Figure 5.17 with a frequency of 52 kHz and a source azimuth of $\vartheta = 0°$, i.e., coming directly from the front of the skull. The wavefield is highly influenced by the skull, especially in its vicinity; there is a strong shadowing effect behind the skull. Some parts of the skull introduce positive SPL on their surface.

SRTFs at the left and the right ear do not show any large differences for all cases; as an example, left SRTF, right SRTF, and their average for the elastic and attenuated case are shown in Figure 5.18. The difference in dB is shown in Figure 5.19. Here, the largest positive difference, i.e., the SPL is larger at the left ear, is around 1.5 dB and the largest negative difference, i.e. the SPL is larger at the right ear, around 2 dB. Since these difference are very sparsely and randomly populated along both axes, SRTFs are considered to be identical at the two ears. The following results are, therefore, evaluated for the average SRTF.

SRTFs for all elevations and cases are shown along the diagonal of Figure 5.20. Differences between the SRTFs of the various cases are shown in the respective off-diagonal entries. On the one hand, all boxes above the diagonal show differences larger than 1 dB: The large positive difference between the acoustic and rigid case (Figure 5.20l) shows that simulating acoustic wave propagation inside the bone (instead of no waves at all) tremendously increases SPLs at the ears, mostly for positive source elevations (above the horizontal plane) and frequencies larger than 10 kHz. Additionally simulating shear waves increases SPLs coming directly from the front of the skull ($-5° < \vartheta < 10°$) (Figure 5.20g). Further incorporating attenuation in the bone (Figure 5.20b) does not increase SPL throughout a certain range of elevations or frequencies. On the other hand, all boxes below the diagonal show differences

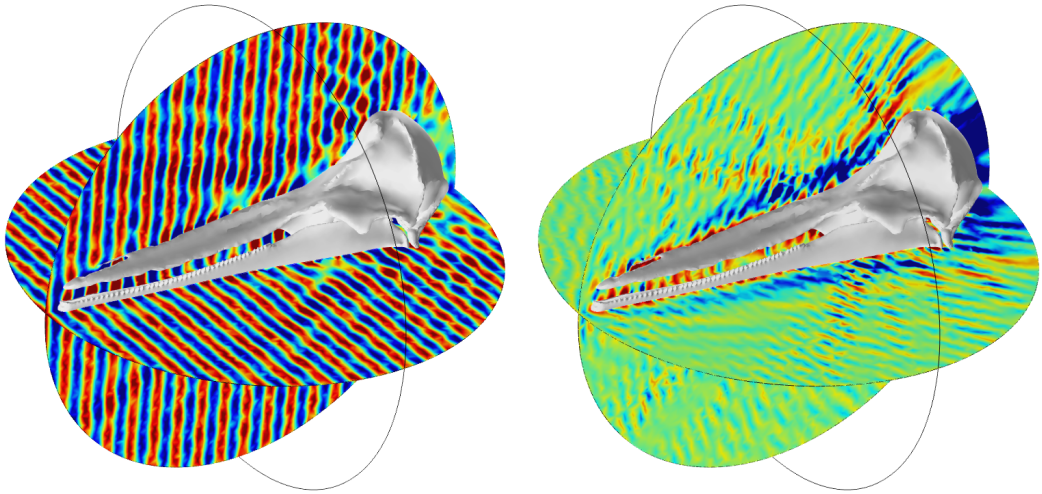

FIGURE 5.17: Exemplary visualizations of the propagating plane wave with a frequency of 52 kHz and source elevation $\vartheta = 0°$, and the resulting SPL, both shown for the elastic and attenuated case. Mandible and cranium are illustrated in gray. **Left:** Snapshot of the plane wave propagating in the water domain. Colors are set to a maximum (dark red and dark blue) of $\pm$ 1 Pa. **Right:** Resulting SPL. Colors are set to a maximum (dark red and dark blue) of $\pm$ 6 dB. If there was no skull, the plane wave would freely travel through the sphere, and the SPL would be zero (light green) throughout.

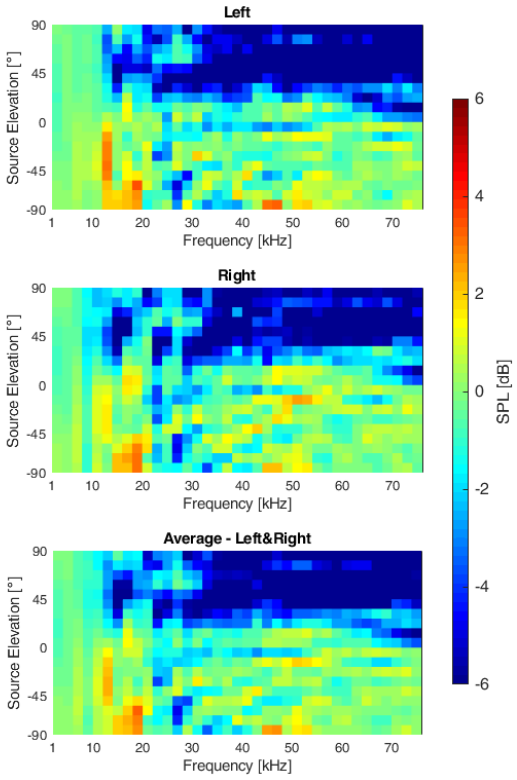

FIGURE 5.18: SRTFs for the elastic and attenuated case at the left ear (**top**), right ear(**middle**), and their average (**bottom**). The average SRTF corresponds to Figure 5.20a.

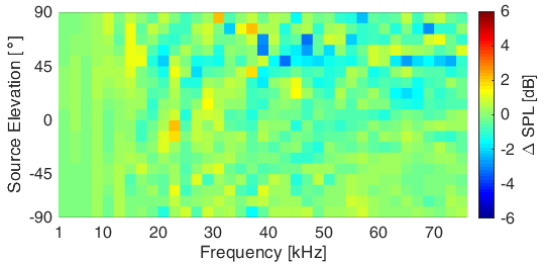

FIGURE 5.19: Differences between SRTFs at the left and right ear for the elastic and attenuated case.

smaller than -1 dB: Figure 5.20o shows that SPLs decrease only for plane waves coming directly below the skull when compressional waves are simulated in the bone. Shear waves introduce lower SPLs mostly for frequencies between 10 and 45 kHz and a source elevation above 45° (Figure 5.20j). Modeling attenuation in bone decreases SPLs for plane waves coming from above the skull and frequencies between 30 and (the maximum simulated frequency of) 76 kHz.

5.5 Discussion

As with every numerical study, modeling complex media such as a dolphin's head, or even just the bones, comes with certain limitations. Mandible and cranium are not homogeneous in density and feature various compositions of trabecular and cortical bone. The material parameters used in this study are, therefore, not physical. However, other studies suggest that the high density cortical bone is most relevant for the acoustic behavior of the bone and its material parameters are confirmed via CT scans to be similar to the ones used in this study (Aroyan et al., 2000; Aroyan, 1996). Poroelasticity of the bone, which varies in the mandible, would more precisely describe the bone, and the influence of porosity on propagating elastic waves should be topic of further research.

Skull asymmetry in odontocete cetaceans has been suggested to be relevant for hearing (Fahlke et al., 2011), possibly leading to different SRTFs at the left and the right ear in the median plane. This cannot be confirmed from the presented results; while left ear and right ear SRTFs do vary to a small degree, the differences are rather sparsely and randomly distributed in frequency and source elevation (see Figure 5.19). It cannot be concluded that these variations are due to the asymmetry of the skull or due to the asymmetric placement of the ears (see Figure 5.16). However, it seems unlikely from the presented results that the skull and its asymmetry alone could cause SPL differences that would enable the animal to localize sources via binaural cues in the median plane (see Figure 5.18).

In contrast to the known asymmetry of cetacean skulls, TPCs are symmetric, i.e., there are little to no functional or structural differences between the left and the right

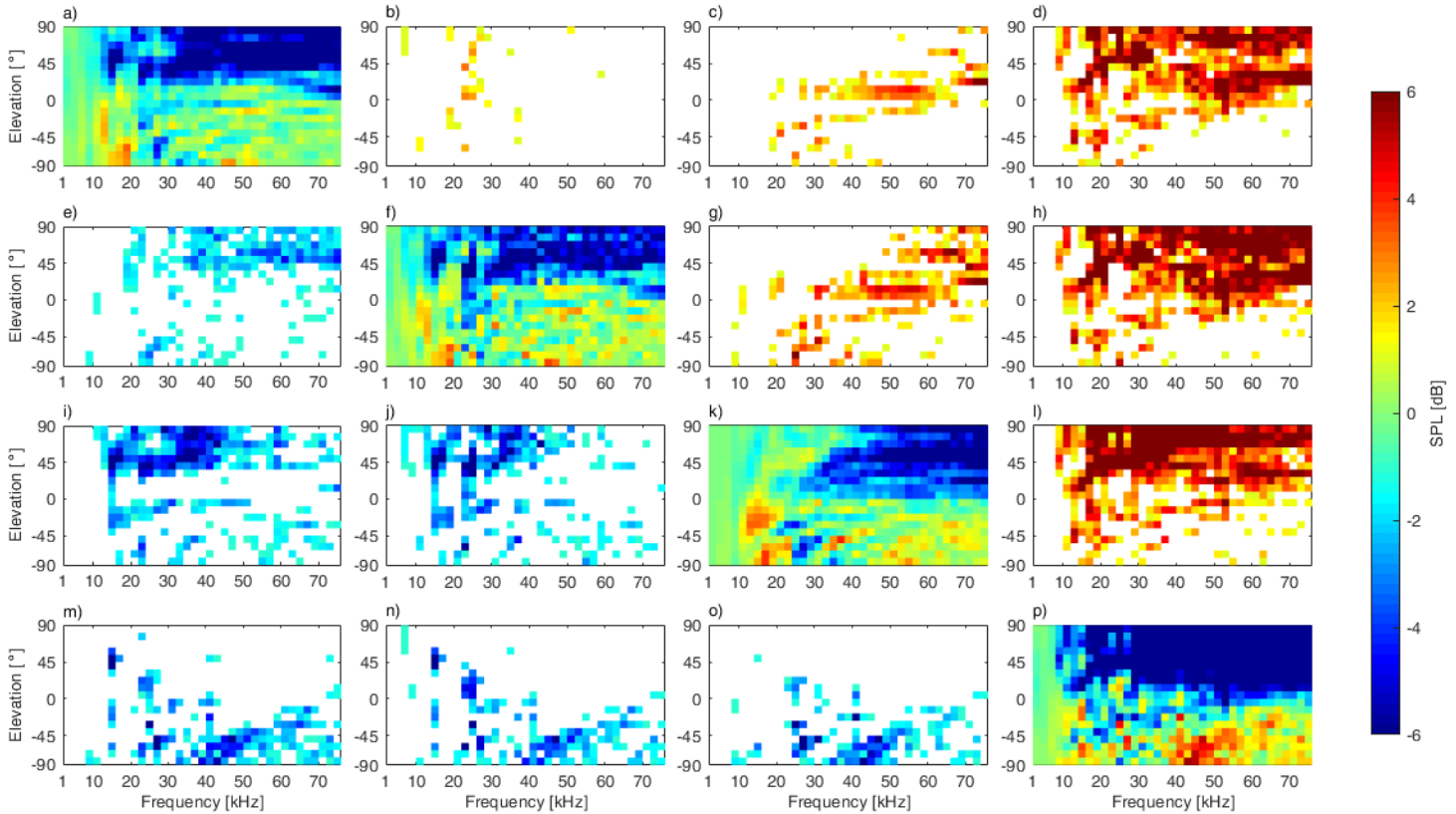

FIGURE 5.20: SRTFs for all cases and their differences. Each diagonal entry of this figure corresponds to a particular case and shows the SRTF; from top left to bottom right: **a)** elastic and attenuated; **f)** elastic, **k)** acoustic; **p)** rigid. Each off-diagonal entry shows differences between results associated with the corresponding two cases. Below the diagonal, only large negative differences are shown (pixels with values larger than -1 dB are masked out); on the contrary, above the diagonals only large positive differences (more than 1dB) are shown. **b),e)** Elastic and attenuated minus Elastic. **c),i)** Elastic and attenuated minus Acoustic. **d),m)** Elastic and attenuated minus Rigid. **g),j)** Elastic minus Acoustic. **h),n)** Elastic minus Rigid. **l),o)** Acoustic minus Rigid.

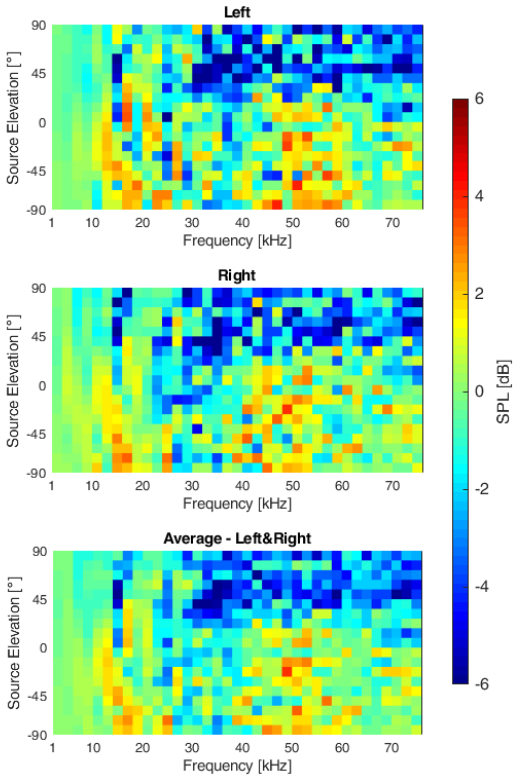

FIGURE 5.21: Same as Figure 5.18, but evaluated at a single point.

TPC (Ary et al., 2016). In this study, they have been modeled as two cubic boxes of similar volume and at the approximate positions of the real TPCs (Ketten, 2000). SPLs are averaged over the surface of these boxes. The simplifying assumption is that the sound pressure perceived by the TPC can be modeled by the average pressure incident on a box, roughly the size of the TPC. This approach neglects the various parts of the TPC (e.g., bones of varying thicknesses, joints, and soft tissues), its frequency-dependent vibration, and its complex shape (Cranford, Krysl, and Amundin, 2010). However, this is not part of this study since the SRTF should be independent of the inner ear functionalities and HRTFs are usually measured before entering the inner ear (Xie, 2013). As a comparison, the SRTF can be calculated at a single point, in the center of the boxes. The equivalents to Figures 5.18 and 5.19 are shown in Figures 5.21 and 5.22 for this method. The diffracted field becomes more diffuse, but the results support the previous assumptions; there are neither clear differences between left and right SRTF, nor salient spectral notches in the SRTFs. The truth may lie somewhere in between the two approaches, but cannot be further evaluated in this study due to the absence of a TPC model. However, even if such a 3D model would be available, it would maybe even be impossible to model the highly complex mechanical processing of sound by the TPC.

It should be acknowledged that the present study is conducted on a rather simplified model, missing soft tissues such as skin, muscles, and fats. Since all of these parts

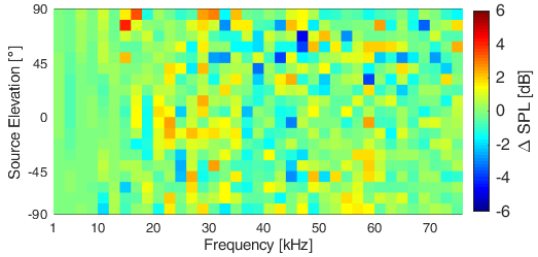

FIGURE 5.22: Same as Figure 5.19, but evaluated at a single point.

are surely somehow relevant for sound conduction (Supin and Popov, 1993; Aroyan, 2001), this study is not an attempt to recreate a complete model of a dolphin's HRTF. Calculating the SRTF and comparing it using various modeling approaches of bone should rather give insight on how sound pressure distribution and the consequent SRTF at the ears changes due to the various types of waves simulated in bone. This work, and the calculated SRTFs should help future studies isolate the influence of certain parts of the head on the HRTF.

Comparing the calculated SRTF with pressure distributions from previous numerical simulations shows differences that need to be explained by certain soft tissue components of the head; numerical simulations by Krysl and Cranford, using a 3D model of a full head, show asymmetric single-frequency HRTFs (Krysl and Cranford, 2016) which are not present in the calculated SRTFs. This could be explained by, e.g., asymmetric positioning of the ears or asymmetries of soft tissues, which are not simulated in this study. Cranford, Krysl, and Hildebrand show highest received pressure amplitudes for plane waves coming from the front, decreasing with higher and lower source elevation (Cranford, Krysl, and Hildebrand, 2008). This cannot be seen in the SRTF. While the results, indeed, show decreasing SPLs with increasing elevation above the horizontal line, sound is not shadowed when coming from below. If, and how, soft tissues, located in the lower head, could attenuate compressional waves needs to be determined in future simulations using 3D models of full heads.

5.6 Conclusion

The different types of elastic waves in a dolphin's skull should not be neglected when studying the animal's hearing or localization abilities, since they affect the SPL at the ear positions. However, independent of how the bone is modeled, the isolated skull of a dolphin does not cause any clear spectral notches, as seen in the HRTF of humans (see Figure 2.5), that could enable high-resolution sound source localization by the animal. If the soft tissues do not serve as a "pinna analog", i.e., create notches in the HRTF, and the bones indeed affect sound the most, a dolphin would have to rely on the SRTF to localize sound in the median plane, which seems unlikely due to the absence of spectral notches.

It can be concluded that there are two possibilities; either it is, indeed, the soft tissues inside the head, especially the mandibular fats, that introduce such cues in the HRTF, or dolphins are capable of extracting from their HRTF more information than terrestrial mammals in sound localization tasks. Research has shown that the neural circuitry of dolphins involved in auditory processing is much larger and contains more neurons that in humans (Wilson, 2002). In addition, the auditory nerve has more fibers and is twice as large (Bullock and Gurevich, 1979; Ridgway, 2000) but brain sizes do not differ (Marino, 1998). The benefits of a larger auditory area in the brain are unknown, but there is little doubt that this grants the species "sophisticated auditory processing" not automatically similar to what humans are able to do (Branstetter and Mercado III, 2006). Chapter 6 presents an application of source-localization algorithms to experimental data obtained from the same skull, which shows that there is enough information contained in the full waveforms of bone-conducted sound to unambiguously localize source elevations.

Chapter 6

Bone-conducted sound in a dolphin's mandible

This chapter is a research article submitted under the title *Bone-conducted sound in a dolphin's mandible: Experimental investigation of elastic waves mediating information on sound source position* to the Journal of the Acoustical Society of America in 2018. The full text of the article is reproduced here with no addition and no modifications except in the form. The part "Summary and conclusions" is renamed to "Conclusion" to better integrate into the structure of this thesis.

The results of Chapter 5 suggest that there are no salient spectral patterns due to the isolated skull. One possible explanation of a dolphin's observed ability to localize sources in the median plane is that there is a more complex mechanism than assigning specific spectral notches to specific elevations. This chapter is a first-ever experimental investigation on the full waveforms of bone-conducted sound in a short-beaked common dolphin's mandible. It is determined whether and to what extent they could contribute to the task of localizing a sound source in the horizontal and median plane. This analysis is based on a time-reversal algorithm.

Photographs that were taken during the setup of the experiment are shown in Appendix B.

Summary

Experiments are conducted in a water tank by deploying, on the horizontal and median plane of the skull, sound sources that emit synthetic clicks between 45 and 55 kHz. Elastic waves propagating through the mandible are measured at the pan bones and used to localize source positions via binaural cues, as well as a correlation-based full-waveform algorithm. The full waveforms, and, most importantly, their reverberated coda, can used to localize sources in both planes. The resolution of coda time reversal in the median plane coincides with the one in the horizontal plane. While further experimental work is needed to substantiate this speculation, the results suggest that the auditory system of dolphins might be able to localize sound sources by analyzing the coda of biosonar echoes.

6.1 Introduction

The acoustic environment of marine mammals is very different than that of humans and other terrestrial mammals. Water is much denser than air, and sound travels five times faster through water than through air and is less strongly attenuated; also, the energy carried by acoustic waves is more efficiently transferred to bone tissue from water than from air; finally, marine mammals have lost external ears through evolution, as those features would be highly disadvantageous in terms of locomotion and hydrodynamics.

Marine mammals use audition, and, in many cases, echolocation, to navigate and hunt. For about two centuries (Hunter and Banks, 1787), they have been known to complete such tasks with remarkable accuracy and efficiency. The specific contribution of dolphin's anatomy to audition-related tasks was first evaluated by Kenneth Norris in a suite of groundbreaking studies (Norris, 1964; Norris, 1968b; Norris, 1968a; Norris and Harvey, 1974). A dolphin's mandible is very thin, almost "translucent," at its posterior end (0.5 mm to 3.0 mm thickness, depending on the species), and is overlain by an oval fatty volume, which connects the posterior jaw bone, also named pan bone, with the tympano-periotic complex (TPC). Norris suggested that sound propagates through the thin pan bone, entering the fats which possibly act as a low-impedance wave guide that directs sound towards the inner ear. This is still the most widely accepted theory of the sound propagation pathway for hearing in cetaceans (Mooney, Yamato, and Branstetter, 2012; Brill, Moore, and Dankiewicz, 2001; Au, 2012; Au and Hastings, 2008) and is supported by experimental (Norris and Harvey, 1974; Brill et al., 1988) and numerical (Aroyan, 2001) results.

It has been suggested by experiments (Blauert, 1997; Renaud and Popper, 1975; Moore, Pawloski, and Dankiewicz, 1995) that dolphins locate sound sources via binaural cues known to be employed by terrestrial animals, i.e. interaural time differences (ITD), which describe the delay of a signal arriving at the two ears at two different times, and interaural level differences (ILD), which describe the difference in intensity between the signals perceived at the two ears. While ITD are relatively easy to reproduce theoretically, ILD effects are more complex, as they cannot be modeled by simply accounting for differences in source-receiver distance: they are importantly affected by sound shadowing due to the impedance mismatch between the subject's head and the surrounding propagation medium (Mooney, Yamato, and Branstetter, 2012), while a significant fraction of acoustic energy traveling from one ear to the other is diffracted by the head's surface, thus following a complex propagation path. In any case, binaural cues are only relevant as long as a sound originates from somewhere else than the median plane. Because median-plane sources are equidistant from both ears, no phase or amplitude (if the subject's anatomical features are symmetric with respect to the median plane, as they most often are) differences exist between the signals perceived at the two ears, i.e. zero ITD and

ILD (e.g. Butler, Humanski, and Musicant, 1990; Hartmann, 1999). ITD and ILD are naturally nonzero whenever the source is not on the median plane, so that the ears lay at different distances from the source.

The only (rare) cases of median-plane sources generating nonzero ITD/ILD are species characterized by asymmetrically positioned ears, e.g., the barn owl (Keller, Hartung, and Takahashi, 1998). Other species, including humans, are not very effective at differentiating sound source positions within the median plane (Butler and Belendiuk, 1969; Heffner and Heffner, 1992; Van Opstal, 2016), or, more generally, within a "cone of confusion" (e.g. Van Opstal, 2016). Their (limited) ability at this task must be explained in terms of non-binaural cues (e.g., acoustical clues not simply related to a difference between right and left signals). It has been suggested that sound-localizing animals learn to interpret certain acoustical cues associated with their anatomy in order to solve this ambiguity (Van Opstal, 2016; Macpherson and Sabin, 2013; Hartmann, 1999; Blauert, 1969; Batteau, 1967). Anatomy can be thought of as a spectral filter (the head-related transfer function, or HRTF), which will change depending on source position: because the back of our head is different from our face, it interacts differently with an incoming wave field, which consequently sounds different to our ears. The HRTF associated with a human skull has been found to provide, in principle, sufficient information for a source to be localized with fairly high accuracy, independent of the location of the source, even when data from only one ear are used (Catheline et al., 2007); yet, psychoacoustics studies (Van Opstal, 2016) have shown that the performance of the, e.g., human ear-brain system at localizing median-plane sources is relatively poor: we are much more effective at discriminating sources within the horizontal plane. Other terrestrial species show the same limitations. It has also been found experimentally that humans are relatively poor at source localization tasks if only one ear is used; subjects with unilateral hearing loss apparently learn to function with one ear only, but their performance at sound localization has been found to remain significantly poorer than that of subjects with no hearing loss (Agterberg et al., 2011; Van Opstal, 2016). It is inferred that, while humans and other terrestrial species certainly use HRTF information in sound-localization tasks, they exploit only a subset of the information provided by the HRTF itself. The consensus is that the only monaural cues that they are actually capable of using are certain "notches" of the frequency spectrum perceived by the ears, or "spectral cues," whose amplitude, and location along the frequency axis, are controlled by the complex shape of the pinnae and depend on the position of the source (Van Opstal, 2016, Chapter 7).

Cetaceans are also characterized by a salient HRTF (Au and Fay, 2012; Aroyan, 2001; Supin and Popov, 1993); how and to what extent they make use of it, is still unclear. Simple physical considerations suggest that anatomical features characterized by relatively strong density contrasts with respect to the surrounding medium (water) most significantly contribute to characterizing the HRTF, and thus to sound

localization. Since the density of soft tissues found in marine mammal bodies is close to that of water (Norris and Harvey, 1974; Haan, 1957), it is inferred that features such as the mandible, the cranium or small air sacs play the most important roles, similar to the external ears of terrestrial mammals. One important difference in the sound localization performance of terrestrial mammals vs cetaceans is the latter's ability to localize sound sources within the median plane with a very high accuracy (Renaud and Popper, 1975). This can be quantified by the minimum audible angle (MAA), i.e., the minimum angular distance between two sources of sound, still allowing to discriminate them as two different sources. Signals emitted by two sources separated by an angle smaller than the MAA are perceived as coming from only one source. The MAA changes depending on the azimuth and elevation of the sources, and on the nature of the emitted signal. By studying the behavior of live dolphins when exposed to sound coming from different locations, their MAA in the median plane has been estimated around 0.7° for broadband clicks. Similar values are observed for sources positioned on the horizontal plane (Au and Hastings, 2008; Nachtigall, 2016). In comparison, psychoacousticians estimate the MAA of human subjects at around 7° in the vertical plane, as opposed to only $\sim 1°$ in the horizontal one (Nachtigall, 2016), while other terrestrial mammals perform more poorly than humans (Heffner and Heffner, 2016, Figure 3). It can be inferred from these observations that, when echolocating, dolphins are capable of extracting from their HRTF more information than terrestrial mammals in sound localization tasks (Branstetter and Mercado III, 2006). The acoustic environment of cetaceans would indeed favor animals capable of localizing sound, whether it be emitted or reflected from prey or predators, regardless of their position in space. Dolphins' MAA grows to 2.3°-3.5° for narrow-band signals (Au and Hastings, 2008; Nachtigall, 2016), which do not mimic typical echolocation clicks.

This study addresses the question of how a dolphin's head inner anatomy may contribute to sound localization, and in particular to echo-localization, by means of a suite of physical acoustics experiments conducted on one skull specimen of short-beaked common dolphin (*Delphinus Delphis*). The HRTF of the short-beaked common dolphin has so far only been addressed in a limited number of studies. Most of our previous knowledge results from numerical models; Krysl and Cranford carried out vibroacoustic simulations on a CT scan of a full head of a common dolphin showing single-frequency HRTFs for 5.6 kHz, 22.5 kHz and 38 kHz (Krysl and Cranford, 2016). In their work, single-frequency HRTFs were equivalent to amplitude or intensity variations with respect to the source position. They simulated sound pressure levels at two virtual positions on the surface of the TPCs (one dorsal, one ventral), caused by monochromatic plane waves traveling along a suite of different azimuths and elevation angles. Strong variations in modeled data were found between the dorsal and the ventral receiver positions. The spatial pattern of the HRTFs was also found to depend strongly on the source frequency used. The results were not conclusive

as to what extent the calculated asymmetries in the receiving pressure pattern were due to the inexact placement of the receivers, versus asymmetries in the specimen's anatomy. Another, similarly minded study (Aroyan, 2001) showed that the mandible and its surrounding fats focus acoustic waves toward the TPC, therefore playing an important role in sound conduction through the head. Receptivity patterns at two virtual ear positions showed high asymmetry and complexity, and varied significantly depending on which parts of the head were simulated.

In our experimental study, we attempt to evaluate the potential contribution of bone conduction to sound localization tasks. Using accelerometers glued to the pan bone, we measure elastic waves traveling through a mandible specimen immersed in water; we record the signal generated by different sound sources, positioned at many different locations within a large water tank; we measure the ITD and ILD (*binaural* cues) resulting from such recordings and estimate their potential performance as source-localization cues. Finally, we study in much detail how the waveform of the recorded signal depends on source position, and use a correlation-based method (known in physical acoustics as "acoustic time reversal" (Fink et al., 2000)) to numerically reconstruct the location of sources via full-waveform data.

Our work provides new data, relevant to the contribution of certain features of dolphins' skulls (in particular, their mandible) to sound localization performance. A number of earlier studies have suggested that the mandible plays a central role in this context (McCormick et al., 1970; Cranford, Krysl, and Hildebrand, 2008; Aroyan, 2001), but the nature of its contribution remained to be determined.

6.2 Experimental setup & data acquisition

All our experiments are conducted on the skull (cranium and mandible) of a male adult short-beaked common dolphin, shown in Figure 6.1a. The skull is ∼50 cm long and ∼20 cm wide. The specimen was acquired on loan from the French National Museum of Natural History (Muséum National d'Histoire Naturelle, Paris, France), inventory number 1989-06 from the Collection of Comparative Anatomy (Collection d'Anatomie Comparée - Mammifères et Oiseaux). Two miniature piezoelectric charge accelerometers (*Brüel & Kjaer* Type 4374) are glued to the inside of the pan bone by a common cyano-acrylate adhesive as shown in Figure 6.1b. These sensors weigh 0.75 g and are characterized by a flat frequency response curve in the frequency range of interest. They are both waterproofed by applying a layer of flexible adhesive. Measurements are conducted in a water tank (6 meters in width, 12 meters in length and 3 meters in depth) filled with chlorinated water kept at the temperature of ∼12°C throughout the duration of the experiment; the specimen is immersed in the water, centered in depth and in width. Both cranium and mandible are independently suspended and aligned with each other according to the real anatomy. The geometry of the experimental setup is shown in Figure 6.2. Let us take the midpoint

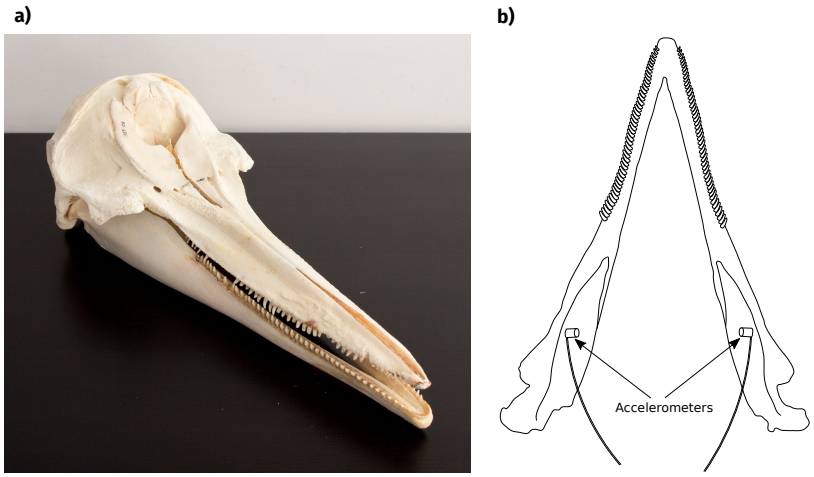

FIGURE 6.1: **(a)** Photograph of the sample (cranium and mandible) used in this study. **b)** Sketch of the mandible and the accelerometers glued to it. The accelerometers are approximately 11 cm apart.

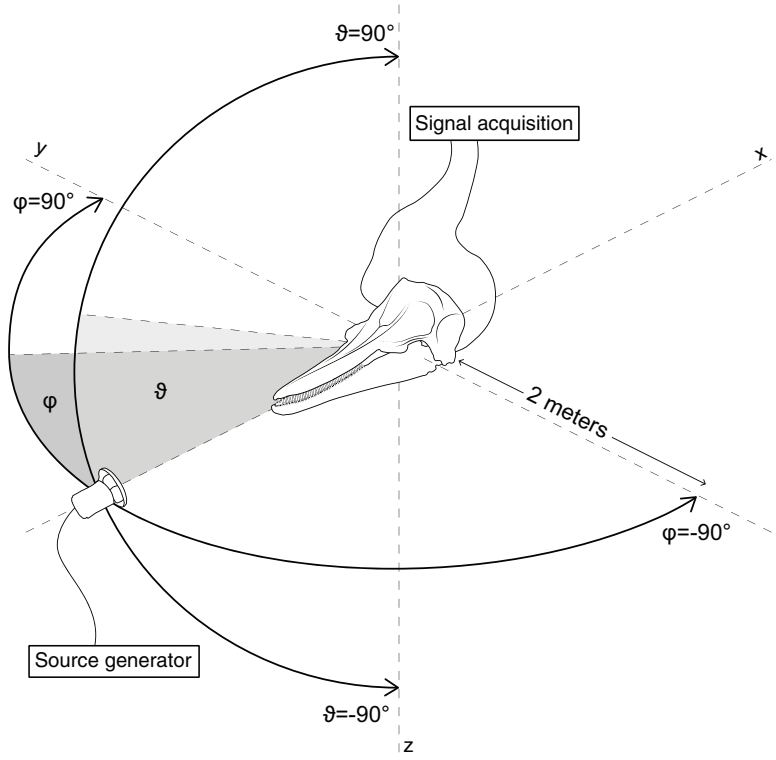

FIGURE 6.2: Sketch of the experimental setup. The sound source moves along two half circles, either in the median or horizontal plane at a distance of 2 m from the origin.

of the segment defined by the accelerometer positions as the origin of a Cartesian reference frame; let the y-axis be defined by the accelerometer positions, while the x-axis is identified by the tip of the mandible and the origin. The horizontal plane consequently lies roughly on the tooth lines. A broadband marine transducer (*Airmar* B75L) with an active area of 9.6 cm^2 and a transmitting voltage response of around 155 dB (re 1μPa per volt at 1 m) throughout the used frequency range is placed at a distance of 2 meters away from the origin in front of the skull along the x-axis. The skull is then rotated around either the z-axis, which corresponds to an angular movement of the transducer in the horizontal plane (i.e. constant source elevation $\vartheta = 0°$), while azimuth φ changes from -90° nearest the left "ear" to +90° closest to the right "ear"), or around the y-axis, which corresponds to an angular movement of the transducer in the median plane (i.e. constant $\varphi = 0°$, while ϑ changes from -90° directly below to +90° directly above the origin). Data are recorded first for a discrete set of source azimuths on the skull's horizontal plane, spaced 1° from one another, from φ=-90°to φ=+90°, and then for a discrete set of source elevations on the vertical plane, again 1° from one another, from ϑ=-90°to ϑ=+90°. For each source location, the transducer emits two different source signals which are digitally generated through a desktop computer and recorded and processed separately. Each source signal is amplified by 30 dB through a home-made power supply resulting in an emitted sound level of about 185 dB (re 1μPa per volt at 1 m).

The source signals are

1. a sinusoidal burst, i.e.

$$c(t) = \sin\left[\phi_0 + 2\pi f t\right] w(t), \tag{6.1}$$

   where ϕ_0 denotes the initial phase of the signal, f=45 kHz and $w(t)$ is a Tukey (tapered cosine) window, which has a total duration of 100 μs and tapers the first and the last 15 μs of the signals, to ensure their smooth on- and offset;

2. a linear chirp

$$c(t) = \sin\left[\varphi_0 + 2\pi(f_0 t + \frac{k}{2}t^2)\right] w(t), \tag{6.2}$$

   with minimum frequency f_0=45 kHz, maximum frequency f_1=55 kHz, chirpyness (i.e., rate of frequency change across the chirp) k=$\frac{f_1 - f_0}{t}$, and $w(t)$ the same Tukey window as above.

The sampling frequency for both signals is 2 MHz. The signals and their normalized frequency spectra are shown in Figure 6.3. The duration and frequency of source signals are chosen to be in the range of that of echolocation clicks of a common dolphin (Soldevilla et al., 2008; Richardson et al., 2013). While the sinusoidal burst is used for the investigation of binaural and monaural cues in both planes, the chirp is solely used for monaural cues.

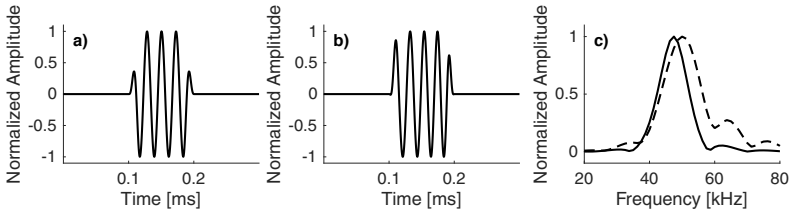

FIGURE 6.3: Source signals and their frequency spectra. **a)** Sinusoidal burst with a duration of 100 μs and frequency of 45 kHz. **b)** Narrow-band chirp with a duration of 100 μs and a frequency range of 45 to 55 kHz. **c)** Normalized spectrum of the sinusoidal burst (solid line) and the chirp (dashed line).

The accelerometers are calibrated to synchronously measure the acceleration of the pan bone on each side of the mandible. At each realization of the experiment, they record for 800 μs at a sampling rate of 2 MHz. The duration of our recordings coincides with the time needed for an acoustic wave to travel 1.2 m in water, which means that signals reflected from the sides, bottom or surface of the tank are well separated and can be easily identified; we systematically cut our data so that such signals are not taken into account. All recordings are Butterworth bandpass filtered, with cutoff frequencies of 40 kHz and 60 kHz to further reduce unwanted noise.

The entire experiment was repeated three times, including setup and wiring, in order to check consistency and minimize the effect of random errors. All measurements presented in the following are obtained by averaging the outcomes of the three experiments, for each combination of source and receiver positions. The associated standard deviation is used as an estimate of measure uncertainty. Throughout this study, we dub "direct" signal the waveform defined by Equations 6.1 or 6.2, as it is recorded at the accelerometers after having propagated through water and bone, and being accordingly attenuated. We dub "reverberated" the signal recorded after the direct signal, refracted, reflected, diffracted by and through bone tissue. For the sake of simplicity, we neglect reverberations occurring before the end of the direct signal; visual inspection (e.g., Figure 6.4) shows that their effect is indeed minor, compared to the complex, relatively long coda.

6.3 ITD- and ILD-based source localization

We define ITD as the onset time of the direct signal measured at the left accelerometer minus the onset time of the same signal, measured at the right accelerometer. We measure the ITD associated to all our recordings of horizontal- and median-plane sinusoidal sources (Equation 6.1). This is done by means of a matlab routine that identifies the shape of the source signal in the recorded signal through cross correlation. We show in Fig. 6.5 the results of this exercise, as functions of source azimuth (if the source is on the horizontal plane) or elevation (if on the vertical plane). For

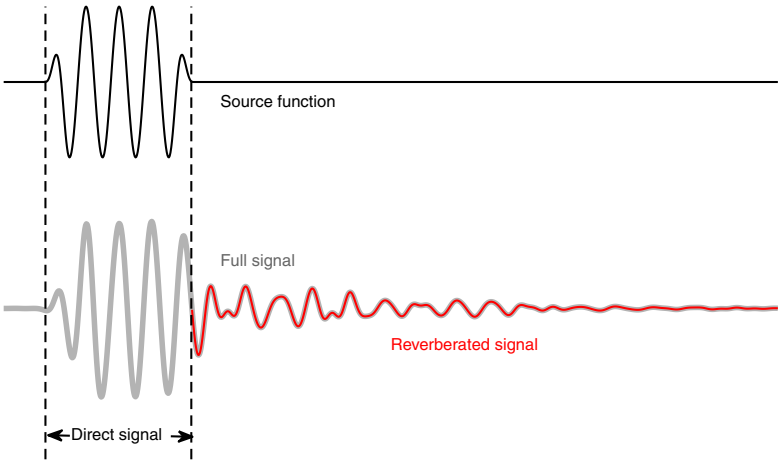

FIGURE 6.4: Examples of **(top)** signal as emitted at the source; **(bottom)** the same signal, as recorded by one receiver. The recorded trace consists of "direct" (grey) and "reverberated" (red) signals, defined in Section 6.2.

median-plane sources, the ITD should be approximately zero; measured values of ITD accordingly never exceed 6 μs, corresponding to an error of 0.9 cm in space. For horizontal-plane sources, by simple geometrical considerations and neglecting HRTF-related diffraction effects (which is reasonable given the absence of soft tissues in our experiment), ITD is expected to approximately coincide with

$$\mathrm{ITD}(\varphi) = (a/c)\sin(\varphi), \tag{6.3}$$

where a is inter-receiver distance and c the speed of sound in water. Again, Figure 6.5 shows a good agreement between our data and theoretical predictions. Importantly, our measure of ITD should not be taken as an estimate of ITD as perceived by live dolphins, which might be significantly affected by the presence of soft tissues and other anatomical features.

We define ILD as the ratio of the maximum amplitudes (Figure 6.6) of the direct signal as recorded by left vs. right receivers, in dB, i.e.,

$$\mathrm{ILD}(\varphi, \vartheta) = 20\log_{10}\left\{\frac{\max\left[s(\vartheta, \varphi, \boldsymbol{r}_L, t)\right]}{\max\left[s(\vartheta, \varphi, \boldsymbol{r}_R, t)\right]}\right\} \quad [\mathrm{dB}], \tag{6.4}$$

where, for the sake of clarity, the signal s is explicitly written as a function of source azimuth and elevation, and receiver position (its only possible values being $\boldsymbol{r}_L$, $\boldsymbol{r}_R$ for left and right receiver, respectively). Although other definitions of ILD have been proposed, e.g. in the field of robotics (Youssef, Argentieri, and Zarader, 2012), Equation 6.4 has been used in similar bioacoustic research (Moore and Au, 1975) and can be interpreted similarly to peak values of electro-physiological audiograms

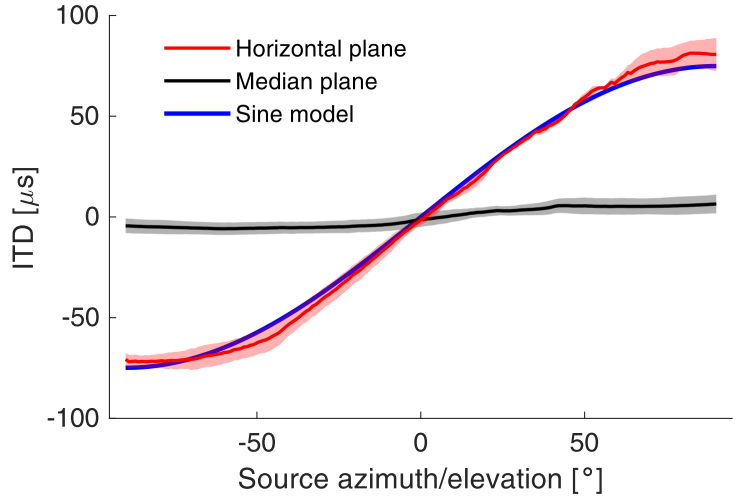

FIGURE 6.5: Measured ITD from our binaural recordings of sources deployed on the horizontal plane (red solid line), as a function of source azimuth, and on the vertical plane (black solid line), as a function of source elevation. Color-shaded areas around each solid line denote standard deviation. Expected horizontal-plane ITD based on the theoretical model of Equation 6.3 is shown as a blue solid line.

(Supin and Popov, 1993; Mulsow, Finneran, and Houser, 2014).

We cannot relate our ILD observations to a simple theoretical model as for the ITD, because of (i) the inherent complexity of waveforms resulting from multiple reverberations within the pan bone, and (ii) our neglect of anatomical features, other than the mandible and skull bones, including cranial air sacks, the albuminous foam (which separates the middle and inner ear from the skull) and acoustically functional fats, that are likely to contribute to ILD (Supin and Popov, 1993; Ketten, 1992) and, interestingly, introduce significant dispersion (Aroyan, 2001). Also, because our setup does not account for such complexity, our data cannot be directly compared to experimental data or realistic numerical ILD models.

Figure 6.7 shows our measures of ILD, derived from waveform data via Equation 6.4, as a function of source azimuth and elevation. As expected, ILD values associated with median-plane sources are close to 0, with fluctuations of less than 2 dB. For horizontal-plane sources, the ILD ranges between 18 dB and -18 dB, changing most rapidly directly in front of the dolphin's beak, at φ between -10° and 10°. In this range of φ, ILD decreases from 13 dB down to -12 dB, losing more than 1 dB per degree. This is an effect of sound shadowing by bone tissues, as the receiver at x_L loses direct acoustic sight of the sound source when this is rotated to the opposite side of the mandible. At larger, positive or negative, azimuths, the ILD grows less rapidly, at a rate of less than 1 dB per degree, and fluctuations (standard deviation) up to ± 2 dB.

The results in Figures 6.5 through 6.7 are not new or surprising per se, but confirm

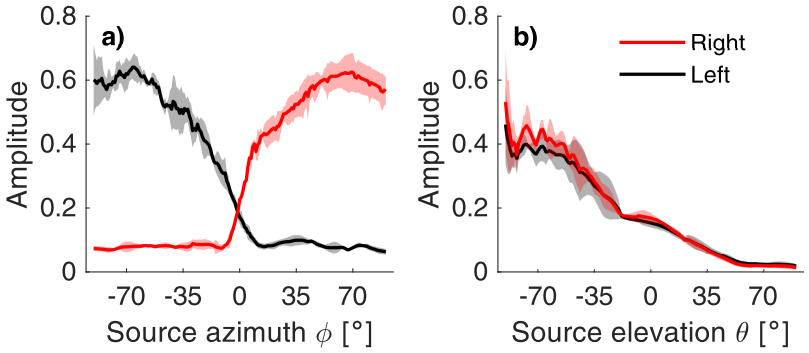

FIGURE 6.6: Maximum amplitudes recorded at the left (black) and right (red) receivers of sources deployed on **(a)** the horizontal plane, as a function of source azimuth, and **(b)** the vertical plane, as a function of source elevation. Color-shaded areas around each solid line denote standard deviation.

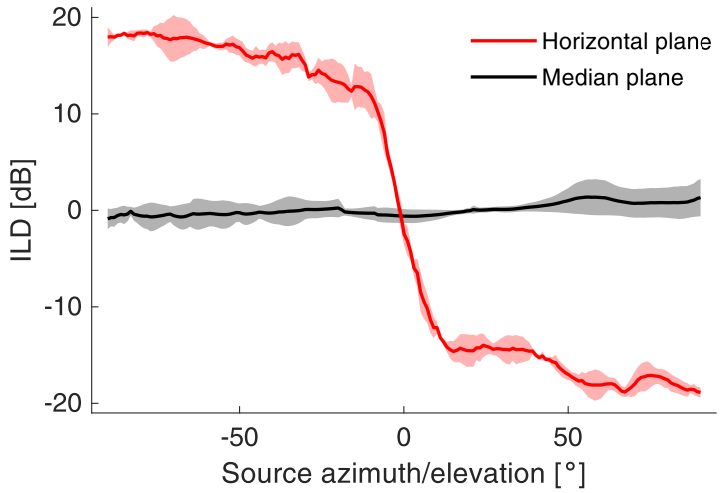

FIGURE 6.7: ILD in both planes. Mean ILD (solid lines) and their standard deviation (color shaded areas) of three independent measurements are shown in red (horizontal plane) and black (median plane).

some simple, well known properties of all binaural auditory systems. Importantly, the left-right symmetries of our data and the fit between data and a simple ITD model confirm that our setup is correct, and adequate to the applications that follow.

6.4 Correlation-based source localization

Waves that interact with a complex HRTF carry a great wealth of information, that could in principle be exploited to localize their sources. Both binaural and monaural cues discussed so far only exploit a small portion of such information. While it has been established that humans and other terrestrial species localize via those cues alone, the echolocation performance observed in dolphins suggests that their auditory system might include a more sophisticated localization mechanism. We implement a simple algorithm to localize sources, based on the time-reversal concept developed by Mathias Fink and co-workers (e.g., Fink et al., 2000; Catheline et al., 2007).

We conduct a "time-reversal" exercise based on the theoretical formulation developed in Chapter 3. Specifically, we implement the right-hand side of Equation 3.17 and study its effectiveness as a source-localization algorithm. In practice, pairs of traces $s(\mathbf{r}_R, \mathbf{r}_A, t)$, $s(\mathbf{r}_R, \mathbf{r}_B, t)$ recorded at $\mathbf{r}_R$ as described in Section 6.2, are cross-correlated to one another, for all possible pairs of source locations $\mathbf{r}_A$, $\mathbf{r}_B$. The same is done for traces recorded at $\mathbf{r}_L$. As a result, for each source location $\mathbf{r}_B$, we obtain the correlation between the corresponding recorded signal and the signal associated to all other possible sources. Because, as explained in the appendix, it is closely related to how sharply a time-reversed wave field would focus at $\mathbf{r}_B$, we dub it "focusing function." Since, in this study, we are looking at sources on the horizontal and median planes only, the focusing function depends on ϑ and φ only; by definition, it is exactly 1 when both ϑ and φ are the same as those of the actual source.

For the sake of simplicity (and speed), cross correlation is implemented by first shifting each pair of signals to have zero lag, and then calculating the correlation between the shifted traces. Intensity differences between the two correlated signals are also irrelevant, as the convolution product is normalized so that the auto-correlation at zero lag equals 1.

We next visualize how well a source is localized by our algorithm as a function of its true location. This is shown in Figure 6.8 through 6.11 where the horizontal and vertical axes of each plot correspond to the azimuth φ_0 or elevation ϑ_0 of the true source and of all recorded sources (φ_i,ϑ_i). Specifically, focusing functions obtained based on the chirp-like source in the median plane are plotted in Figure 6.8, while Figure 6.9 shows the corresponding results for the sinusoidal source. By definition, values on the diagonal of all panels in both figures are 1; near the diagonal, correlations decrease monotonously in all panels; some relevant fluctuations are then observed in both figures for ϑ_i far from ϑ_0 when both direct and reverberated signals

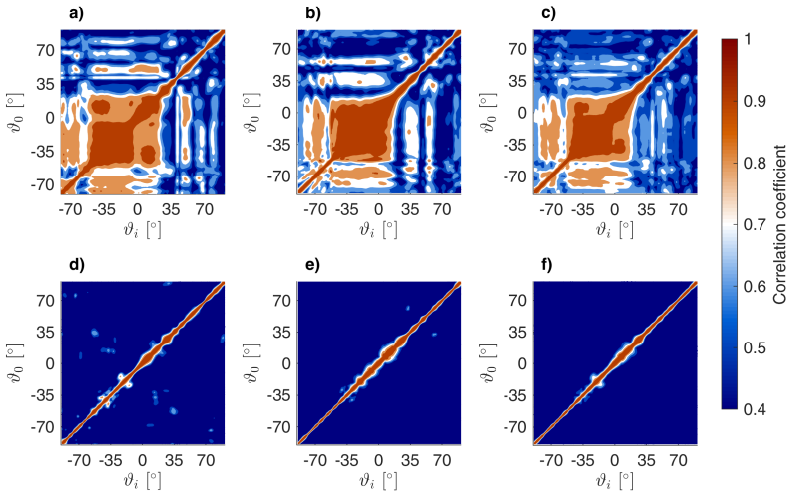

FIGURE 6.8: Focusing functions in the median plane using the chirp-like source function as determined from the entire waveform, recorded by the **(a)** left, **(b)** right, and **(c)** both (sum of (a) and (b)) accelerometers, and from the reverberated waveform alone, again at **(d)** left, **(e)** right, and **(f)** both accelerometers. Each row of a given panel shows, accordingly, the maximum cross correlation value between the signal associated with one particular source (defined by its elevation ϑ_0), and those of all other sources (elevations ϑ_i on the horizontal axis).

are correlated, but not when the reverberated signal alone is considered. In the latter case, the focusing function is much sharper, particularly in the -50° to 20° elevation range, and its sharpness does not seem to depend on source elevation ϑ_0.

To study how the resolution of our algorithm depends on the true source position in the median plane, we visualize (Figure 6.10a for the chirp-like source function, Figure 6.10b for the sinusoidal source function) the increment in ϑ needed for the focusing function to decrease to 70% of its maximum, i.e. the -3 dB width of the focusing function, which is a rule-of-thumb criterion frequently used in time-reversal acoustics (Ing et al., 2005; Catheline et al., 2007; Kim et al., 2003). The smaller the value of the -3 dB width, the higher the resolution, and the performance that can be expected in identifying the true source location. The value of 3 dB is of no particular physical or biological significance: it is only chosen in analogy with the mentioned studies. This is adequate to our goals, as we are not attempting to reproduce absolute, observed MAA values, but rather to estimate the relative changes in the resolution in source localization. Figures 6.8 through 6.10 show that direct signal alone does not provide sufficient information to discriminate sources in the -50° to 20° elevation range; on the contrary, it obscures the information contained in the reverberated signal, which, if used by itself, actually results in much sharper focusing functions. It is apparent from our results that our algorithm achieves approximately equal accuracy for monochromatic vs multi-frequency signals (Figure 6.8&6.9). Figure 6.10 shows that localization of a sinusoidal source affords slightly lower resolution (larger

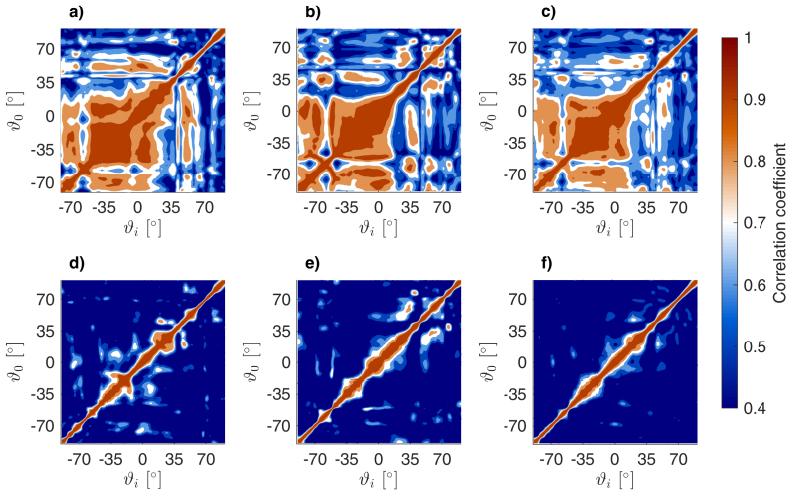

FIGURE 6.9: (Color online) Same as Figure 6.8 but using the sinusoidal source function.

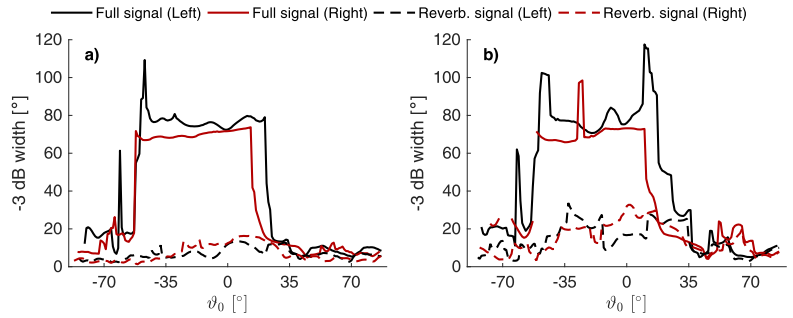

FIGURE 6.10: -3 dB widths of the focusing functions in the median plane using **a)** the chirp-like source function and **b)** the sinusoidal source function.

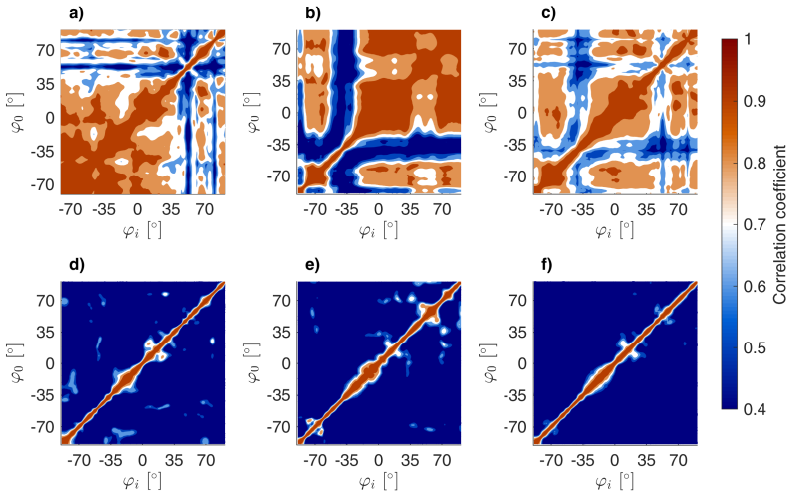

FIGURE 6.11: Same as Figure 6.8 but in the horizontal plane, i.e. φ defines the azimuth.

-3 dB widths) throughout all elevations. As to be expected, widening the frequency band of the source increases the resolution of this algorithm. Similar inferences can be made based on the focusing functions obtained from horizontal-plane sources, which are shown in Figure 6.11. In this case, the resolution highly benefits from analyzing the reverberated signal alone, if the source is on the same side of the skull as the respective receiver. Interestingly, the -3dB width is similar to that extrapolated from Figures 6.8&6.9, i.e. our algorithm is about equally sensitive to changes in azimuth vs elevation of the source.

6.5 Conclusion

We have developed a source localization algorithm (Section 6.4) based on the cross correlation of an observed signal with a library of known signals, each corresponding to a different source location. We have implemented the algorithm in the context of a biosonar application (Equation 3.17 and related discussion), and "source" should be interpreted here as synonymous with biosonar "target" (or "secondary" source). We have substantiated our source-localization metric from a theoretical standpoint, by drawing an analogy between cross correlation and the theory of acoustic time reversal. We have evaluated the performance of our algorithm, as applied to a particular setup, via a suite of experiments. The setup consists of two accelerometers installed on the mandible of a dolphin skull, fully immersed in a large water tank, and recording signals similar to a dolphin's echolocation "clicks."

We quantify the performance of our algorithm via the width of the the focusing function, or, in other words, the rate at which correlation decreases, as an observed signal is compared with library signals associated with sources increasingly far from

the true one. We find that this width is significantly reduced (the rate of correlation loss is accelerated) when the direct signal, which is simply an attenuated version of the original chirp/sinusoidal burst, is subtracted from the recorded waveform before cross correlation. This way, only the reverberated coda, most strongly affected by the shape and properties of the skull, is actually employed in localization: localizing by reverberated signal alone (rather than the entire wavetrain) sharpens source resolution.

The spatial accuracy of source localization by dolphins has been observed to be equally accurate independent of source azimuth and elevation, i.e., it has approximately constant resolution over the entire solid angle (Nachtigall, 2016). This property of dolphins is counter-intuitive, if one considers that humans and other species have presumably evolved pinnae to help determine the elevation of sound sources (Section 6.1), while cetaceans have actually lost them. We infer that, to achieve such performance, the dolphin's auditory system might make use of a localization tool, particularly effective for sources in the median plane or along the "cone of confusion." Our results suggest that signal reverberated within the dolphin's skull contains sufficient information to discriminate median-plane sources; we have shown that this could be achieved by simply cross-correlating any newly perceived sound with a library of previously recorded data.

Bone conduction (reverberation) is a possible contributing mechanism to sound localization. Here we have investigated this mechanism using a method that gives access to the optimal performance of such mechanism (limit case) through a correlation-based algorithm. While our model shares with dolphins some relevant features, we are hardly reproducing the signals that would be perceived by actual dolphins, and we cannot even attempt to reproduce quantitatively the observed localization performance of live specimens. More experiments will be needed to determine how several anatomical features, which we have not accounted for, might affect the perceived waveforms: it is expected that soft tissues surrounding the bone should have a significant effect. Our results, however, indicate very clearly that, within a good approximation, a one-to-one correspondence exists between the waveform of the bone-conducted, reverberated coda as recorded at a dolphin's ear locations, and the locations of the source (or, in principle, the reflecting target) that originally generated (or reflected) the signal. While we have no knowledge of how such information might be processed and exploited by the brain, we speculate that bone-conducted, reverberated sound is a key factor in explaining the peculiar, poorly understood accuracy of sound localization in odontocete cetaceans (Nachtigall, 2016).

Acknowledgments

This project has received funding from the European Union's Horizon 2020 research and innovation programme under the Marie Sklodowska-Curie grant agreement No

641943 (ITN WAVES). We are grateful to Christine Lefèvre, and to the Collection of Comparative Anatomy at the French National Museum of Natural History, for providing the skull specimen on which all our experiments were conducted.

Chapter 7

On the interaction of bone-conducted sound and mandibular fats

This chapter presents 2D time-domain numerical simulations on a simplified model of a dolphin's head using the spectral-element method. It complements the two preceding chapters by analyzing the influence of mandibular fats, and their interaction with bone-conducted waves on sound propagation pathways through the head, the resulting signals at the ear positions and acoustic source localization algorithms such as interaural level differences and time reversal in the horizontal plane.

Summary

Maximum amplitudes of time-domain signals are calculated at hypothetical ear positions, having propagated from various incident azimuths through a 2D model of a dolphin's head. The incorporation of mandibular fats leads to an increase in amplitude for source azimuths of around 20° to the ipsilateral side for each ear respectively. Similar patterns have been found in other experimental and numerical studies. In the absence of shear elasticity in the mandible, these peaks vanish for high frequencies and decrease for lower frequencies. Hence, only the combination of mandibular fats and an elastically modeled mandible show results similar to the ones found in other studies. Furthermore, full waveforms are examined using a TR source localization algorithm. The highest differentiability of the waveforms, i.e., the highest resolution of the algorithm is achieved with the model including fats and an elastic mandible. Neglecting either of them simplifies the waveforms and reduces resolution, especially for high frequencies. Complex wave propagation patterns, such as guided lamb waves, in and along the pan bone are likely responsible for this phenomenon.

7.1 Introduction

The ratio of wave speed in water vs. all soft biological tissues is close to 1, as opposed to 2 for bone vs. water. It could, therefore, be presumed that bone tissue has the most effect on sound pressure levels (SPL) perceived by a dolphin. However, it has been suggested that the mandibular fats, whose chemical composition and distribution are acoustically functional (Koopman et al., 2006), could guide sound to the ears, and amplify it (see Section 2.4.4). Aroyan presented numerical simulations on dolphin hearing and isolated the effect of the mandibular fats. He found focal behavior of the SPL at each ear, resulting from sound propagation through the pan bones of the lower jaw and the surrounding fats. (Aroyan, 2001). However, only compressional waves were modeled in this work, and the elastic property of the skull, especially the mandible, was neglected.

This study investigates the influence of the interaction of bone-conducted sound in an elastic mandible and the connected mandibular fats. More precisely, the question is answered of how this combination affects SPLs at the ears and acoustic source localization algorithms such as interaural level differences (ILD) and time reversal (TR) in the horizontal plane. To isolate and quantify the effect of certain parts of the head, simulations are conducted on models neglecting either the fats or the shear elasticity of the mandible, i.e., the mandible is assumed to be an acoustic medium.

7.2 Simulation setup

7.2.1 SPECFEM2D

All simulations in this chapter are carried out using the time-domain spectral-element software package SPECFEM2D. This software is a high-order variational numerical algorithm (Priolo, Carcione, and Seriani, 1994; Faccioli et al., 1997) and is widely used in applications ranging from seismology (Komatitsch and Vilotte, 1998; Komatitsch and Tromp, 1999; Komatitsch, Ritsema, and Tromp, 2002) to ultrasonics (Van Wijk et al., 2004). The mesh consists of 4-node hexahedral spectral elements, each smaller than $1/6$ of the smallest wavelength to ensure precise calculations. The simulation domain is partitioned for parallel computing by the SCOTCH library, developed by Pellegrini and Roman (Pellegrini and Roman, 1996) and implemented in SPECFEM2D by Martin et al. (Martin et al., 2008), which provides efficient mesh partitioning routines. Five GLL points are assigned to each element in both coordinate directions. To minimize the effect of reflections from the boundaries of the simulation domain, convolutional perfectly-matched absorbing layers are implemented at all four boundaries. Xie et al. provided the implementation of this method in SPECFEM2D (Xie et al., 2014; Xie et al., 2016). Based on the chosen wave velocities,

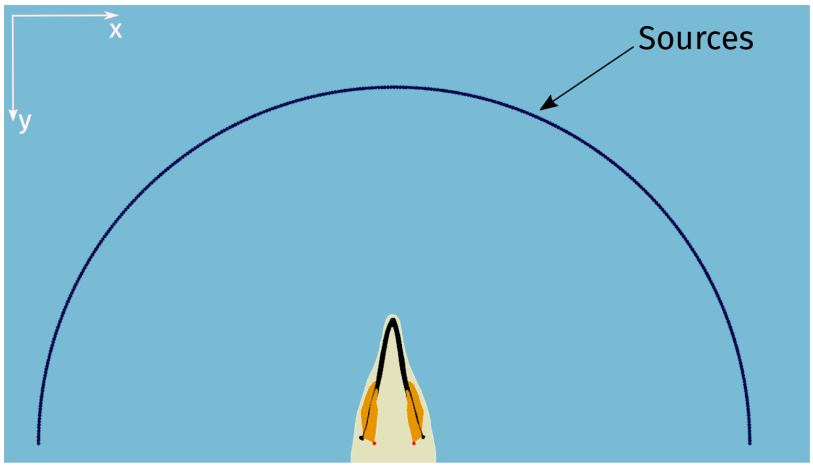

FIGURE 7.1: The simulation domain is comprised of a 2 x 1.2 m rectangle modeled as water (blue). A 2D model of a dolphin's head, including mandible (black), mandibular fats (orange) and surrounding soft tissues (light brown) is surrounded by sources (black dots), placed in a radius of 1 m around the point centered between the two ears.

time steps are chosen to be small enough to obey the Courant–Friedrichs–Lewy condition (Courant, Friedrichs, and Lewy, 1928) and are implemented using a 2nd-order Newmark scheme. All simulations are run on two CPUs of type Intel(R) Xeon(R) CPU E5-2695 v3 using 2 sockets and 40 cores in total.

7.2.2 Simulation domain

The simulation domain is comprised of a 2 m (x-dimension) by 1.2 m (y-dimension) rectangle, with a surrounding absorbing layer of 6 mm thickness. The area of the rectangle is considered to be water, and appropriate material parameters are assigned. Furthermore, a simplified 2D model of a dolphin's head is embedded in the domain. The whole domain is shown in Figure 7.1. The shape of the head is created manually, using the meshing software package Cubit® and several CT-scan images, such as Figure 2.9 and others taken from the publicly available image database of the University of Texas at Austin (Digimorph, 2002). The model is based on a transverse slice, intersecting the head at the two ear positions. The anatomy is chosen to be as general as possible, resembling all types of dolphins. Furthermore, only a few anatomical parts are modeled; the mandible (black), the mandibular fats (orange), and all other soft tissues (light brown). The two inner ears (red dots) are simplified to infinitesimally small points. Undoubtedly, the anatomy is more complex in real life, but the most prominent properties of a dolphin's head are successfully modeled; the elongated beak and mandible, the thin pan bone, and the mandibular fats. Each of the three parts of the head (mandible, tissues, and fats) is considered to be a homogeneous isotropic medium with their assigned material parameters shown in Table 7.1. Soft tissues and fats are modeled as acoustic media due to the highly dampened shear

TABLE 7.1: Material parameters for different parts of the head

Material parameter	Water	Tissue	Fats	Bone
Color in Figure 7.1	Blue	Light brown	Orange	Black
Density [kg/m^3]	998	1000	937	2600
P-wave velocity [m/s]	1483	1520	1390	2923
S-wave velocity [m/s]	-	-	-	1790

FIGURE 7.2: Mesh of the 2D dolphin's head. The dolphin's head and the surrounding water is meshed using 2 mm hexahedral elements.

wave speeds in soft materials (Frizzell, Carstensen, and Dyro, 1976; Carstensen, 1979; Madsen, Sathoff, and Zagzebski, 1983). The mandible, however, is modeled as an elastic medium including attenuation, i.e., the Q factor for compressional and shear waves is set to 30. Material parameters for the mandible are taken from Krysl and Cranford (Krysl and Cranford, 2016), which have been validated in Chapter 5. Values for soft tissues and fats are taken from Soldevilla et al. (Soldevilla et al., 2005) and Norris and Harvey (Norris and Harvey, 1974), and are simplified according to the model.

The entire domain is meshed with a maximum element size of 2 mm. While the water domain is mostly comprised of regular quadratic elements, the meshing algorithm takes the irregular shape of the head into account (see Figure 7.2). The final mesh has $\sim$ 500,000 elements. Each simulation solves for $\sim$ 8 million degrees of freedom and takes around 20 minutes.

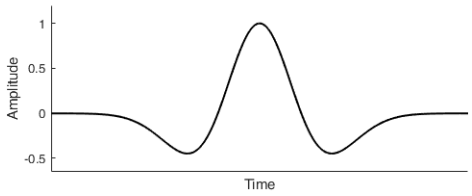

FIGURE 7.3: The source function has the shape of a Ricker wavelet, or Mexican hat function.

7.2.3 Running the simulation

The acoustic pressure at the two ears due to sound sources at various azimuths φ_i is computed the following way; source positions are defined along a half circle at a distance of 1 meter from the center between the two ears with an angular spacing of 0.5°, ranging in azimuth from $\varphi = -90°$ (to the left of the head) to $\varphi = 90°$ (to the right of the head) Sources are illustrated as black dots in Figure 7.1. In the implementation of this setup, the principle of reciprocity is key; instead of running 361 simulations, one for each sound source, sounds are emitted at the two ear positions, one simulation for each ear, and acoustic pressure is recorded at the 361 positions along the half circle. However, to facilitate understanding of the results, signals are considered to be emitted outside of the head, at positions along the circle and to be recorded at the ears. Each signal has a sampling rate of 50 MHz and 60,000 samples.

The emitted source function is a point-source Ricker wavelet, shown in Figure 7.3, and sometimes called Mexican hat function, which is the negative normalized second derivative of a Gaussian function. This wavelet can be defined by a single parameter - the central frequency f - and its amplitude $A(t)$ can be expressed as

$$A(t) = [1 - (2\kappa)]\, e^{(-\kappa)}. \tag{7.1}$$

with $\kappa = \pi^2 f^2 t^2$. The source function is normalized to a maximum pressure of 1 Pa. 20 different source functions, i.e., 20 different central frequencies are used; 5, 10, 15, ..., 95, 100 kHz. Each simulation, using one of the source frequencies, results in 361 recordings at each ear, one for each different source azimuth.

If there was no head, and the acoustic wave would propagate solely in water, all that would be recorded at the two ear positions is the unchanged Ricker wavelet, still traveling with the same amplitude (except maybe a small influence of geometrical spreading). The complex geometries of the head induce reflections and refractions on the boundaries, which can be seen in the calculated signals at the ears. These waveforms can then be used to investigate how sound changes on its way to the ear, having propagated through various parts of the head. Do some parts amplify incoming sound? Does the waveform increase in complexity due to scattering on and along certain boundaries?

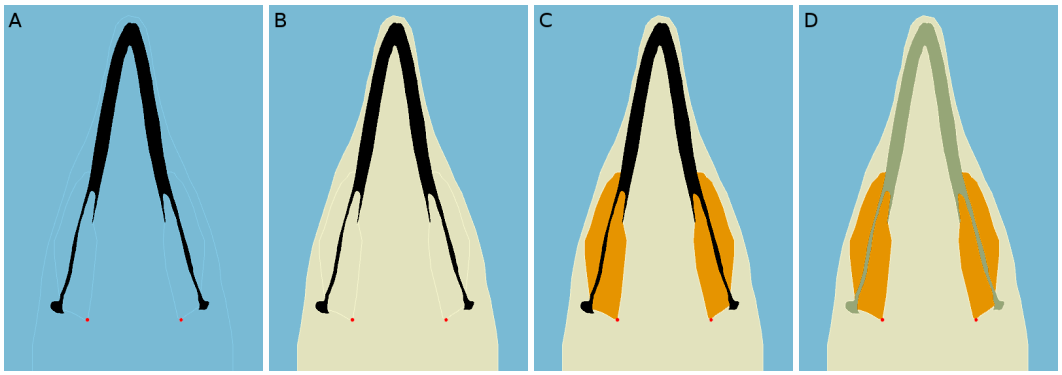

FIGURE 7.4: The four different head models. From left to right. **A:** Neither soft tissues nor fats are considered; the mandible is just surrounded by water. **B:** No fats are considered; the area of the fats is modeled as tissues. C) All parts of the head are modeled. **D:** Same as **C** but the mandible is modeled as an acoustic medium, i.e., the S-wave velocity is set to zero.

Since all parts of the head are connected, it would be difficult, using the head model shown in Figure 7.1, to isolate the influence of certain parts, e.g., the fats. Simulations are therefore carried out for four different cases, all of them illustrated in Figure 7.4. In the following presentation of the results, the four cases are labeled S_A, S_B, S_C, and S_D (left to right in Figure 7.4). The first case, S_A, neglects all soft parts of the head. The material parameters of water are also applied to the tissue and fat region, leaving the mandible surrounded by water. The second case S_B, considers the fats to have the same material parameters as the tissue. The third case S_C, which is the most "realistic" case, includes tissue, fats, and an elastic mandible, contrary to fourth case S_D which also considers tissue and fats but, here, the mandible is modeled as an acoustic medidum, i.e., the S-wave velocity is set to zero and only compressional waves are allowed to travel inside the mandible.

7.3 Results

7.3.1 Amplitudes and ILD

Maximum amplitudes of each signal are shown in Figure 7.5 for the left ear position, and Figure 7.6 for the right ear position. The results are slightly asymmetric but show, generally speaking, the same results for each side: There is little to no difference between S_A and S_B. The density ratio between water and tissue, which is 2%, is too small to induce noticeable differences in the maximum amplitudes of the signals. For sound coming from the sides, i.e., azimuths φ close to $\pm 90^\circ$, the incident angle is perpendicular to the water/tissue boundary, but, still, this does not affect the amplitude. When fats are considered, and the mandible is elastic (S_C), amplitudes change considerably. Incoming sounds are amplified by as much as 4 dB,

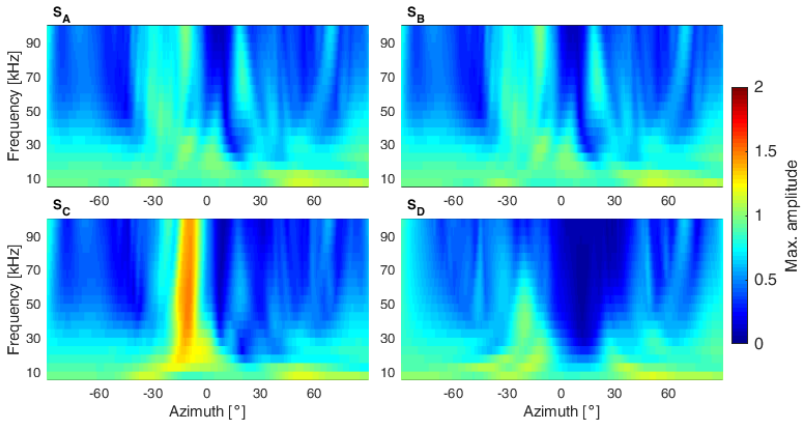

FIGURE 7.5: Maximum amplitudes at the left ear position for case S_A (**top left**), S_B (**top right**), S_C (**bottom left**), and S_D (**bottom right**). Incident pressure amplitude of 1 is shown in green, larger amplitudes increase from yellow to red to a maximum of 2, while smaller amplitudes decrease from light blue to dark blue.

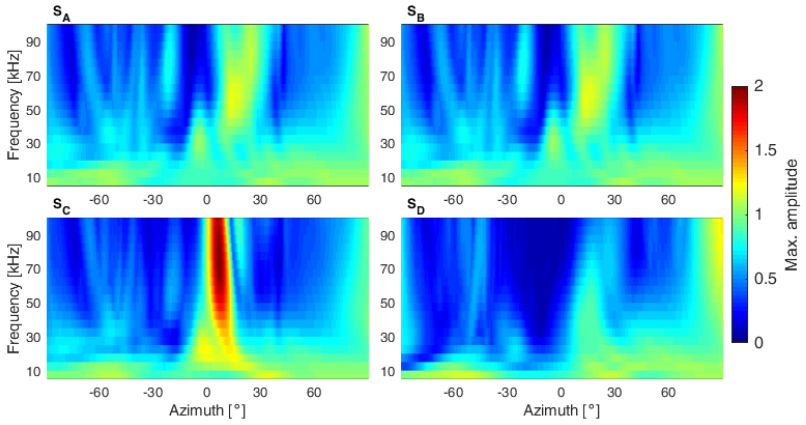

FIGURE 7.6: Same as Figure 7.5 but calculated at the right ear position.

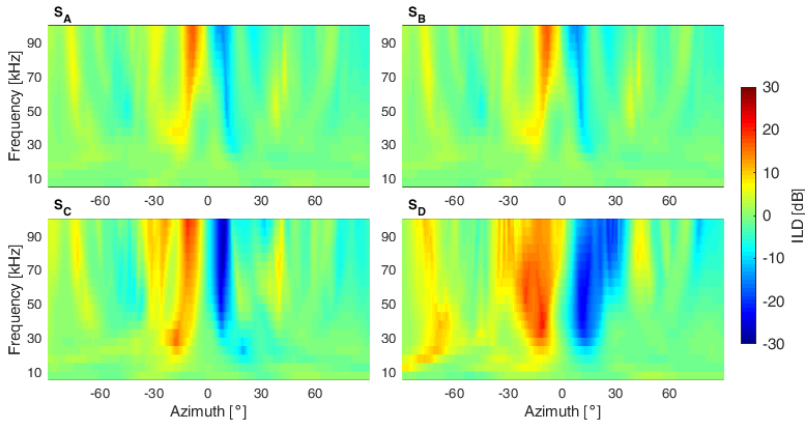

FIGURE 7.7: ILDs for case S_A (**top left**), S_B (**top right**), S_C (**bottom left**), and S_D (**bottom right**). Positive values, i.e., larger amplitudes at the left ear are shown in yellow and red, negative values, i.e., larger amplitudes at the right ear are shown in blue.

i.e., maximum amplitude of 1.6 Pa, at the left ear, and 5 dB, i.e., maximum amplitude of 1.8 Pa at the right ear. Interestingly, this amplification does not occur on the far sides of the head, but between 15 and 20° to the respective sides and throughout most frequencies. If the S-wave velocity is set to zero, and no shear waves are present in the mandible (S_D), the amplification effect of the fats is strongly reduced, especially for high frequencies. Furthermore, amplitudes at the left ear are drastically lowered for source azimuths φ between 5 and 40°, and between -40 and -5° for the right ear respectively. This is due to the acoustic shadowing zone of the front part of the mandible. At these incident angles, sound needs to travel through or around the front half of the mandible to reach the ears. Only the combination of low-density/low-velocity mandibular fats and the elastic mandible introduces large high-frequency amplitudes for sound coming from 15 to 20° to the ipsilateral side of the head.

Amplitudes at the two ears are used by mammals to localize source azimuths through ILD. Here, ILD is calculated in dB through the ratio of maximum amplitudes $A_{L/R}$ at the left and right ear respectively, i.e.,

$$ILD = 20 \cdot log_{10}\left(\frac{A_L}{A_R}\right). \tag{7.2}$$

If the sound has a higher amplitude at the left ear than the right ear, ILD is positive, otherwise negative. However, this choice of numerator and denominator is arbitrary, and could as well be switched. ILDs in Figure 7.7 show what was already to be expected from the amplitudes in Figure 7.5 and 7.6; source azimuths with strong amplification of amplitudes in S_C also show largest ILDs. Maximum ILDs are 15 dB (S_A), 15 dB (S_B), 25 dB (S_C), and 22 dB (S_D) and decrease for azimuths smaller than -30° and larger than 30°, i.e., more than 30° to each of the sides.

7.3.2 Time reversal

So far, only maximum amplitudes of the signal have been evaluated. The full waveform, including reflections smaller in amplitude than the maximum, has been neglected. However, it has been experimentally shown in Chapter 6 and 4 that the full waveform of signals, especially the coda, could be used to localize sound sources. This also is investigated here, using the same full-waveform localization method of TR. Signals are analytically back-propagated via cross correlation, and the resolution of the algorithm is evaluated via the -3 dB width of the focusing function. For the sake of completeness of this chapter, the fundamental equations are restated as follows.

Following, e.g., Fink (Fink, 2006), each signal $s(\varphi_0, r_{L/R}, t)$, recorded at the left or right ear position $r_{L/R}$, and originating from azimuth φ_0 is reversed in time, and convolved with all $s(\varphi_i, r_{L/R}, t)$ for all possible values of φ_i and recorded at the same ear:

$$T_i(\varphi_0, r_{L/R}, t) = s(\varphi_0, r_{L/R}, -t) * s(\varphi_i, r_{L/R}, t). \tag{7.3}$$

The term $s(\varphi_0, r_{L/R}, -t) * s(\varphi_i, r_{L/R}, t)$ can be seen as the transfer function of the TR algorithm and the convolution ($*$) coincides with the cross correlation of $s(\varphi_0, r_{L/R}, t)$ and $s(\varphi_i, r_{L/R}, t)$, hence, the Green's function of the system (Draeger and Fink, 1999; Derode et al., 2003). For each source azimuth φ_0, the signal processing procedure consists of finding the maximum value, with respect to time, of the correlation T_i for each φ_i. The resulting function $F(\varphi_i)$ is next normalized to its maximum so that the maximum of the autocorrelation

$$s(\varphi_0, r_{L/R}, -t) * s(\varphi_0, r_{L/R}, t) = \int s(\varphi_0, r_{L/R}, t+\tau) * s(\varphi_0, r_{L/R}, t) d\tau, \tag{7.4}$$

is set equal to 1 (Draeger and Fink, 1999). It is then reasonable to assume that, the closer $F(\varphi_i)$ is to 1, i.e., identical signals, for a given value of φ_i, the closer φ_i is to the original source φ_0. This method is not only useful in localizing unknown source positions but can be interpreted as a pattern recognition system. The closer $F(\varphi_i)$ is to 1, the more similar the two signals are, while the smaller it is, the more differentiable the signals are from each other. This procedure can be done either using signals recorded at only one of the ears or taking both ears into account by computing the mean of the two focusing functions.

Focusing functions are shown for three frequencies (20, 50, and 100 kHz) in Appendix C. When the azimuth φ_0 of the true source coincides with the signal associated with a target φ_i recorded in the library, correlation is perfect by construction; hence, the value of each diagonal entry is 1, due to the normalization of the autocorrelation (Equation 7.4). The correlation coefficient should then decay with growing distance discrepancy $\Delta\varphi$, i.e.,

$$\Delta\varphi = |\varphi_0 - \varphi_i|. \tag{7.5}$$

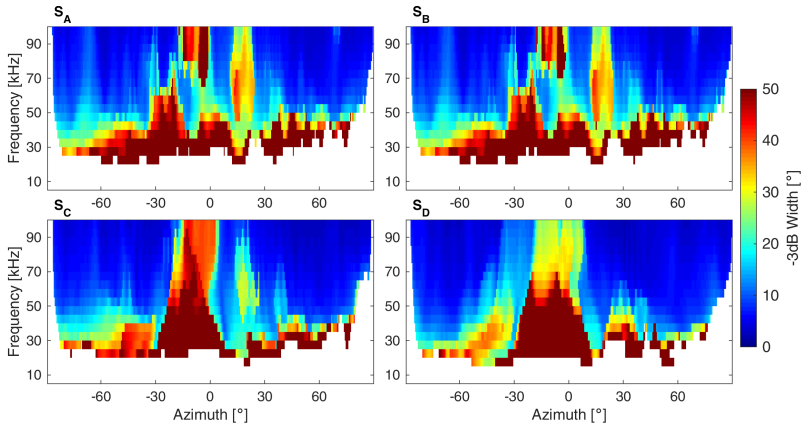

FIGURE 7.8: -3 dB widths of the focusing functions for case S_A (**top left**), S_B (**top right**), S_C (**bottom left**), and S_D (**bottom right**), and signals measured at the left ear. For white areas, the focusing functions did not decrease below -3 dB to both sides and -3 dB widths could not be calculated.

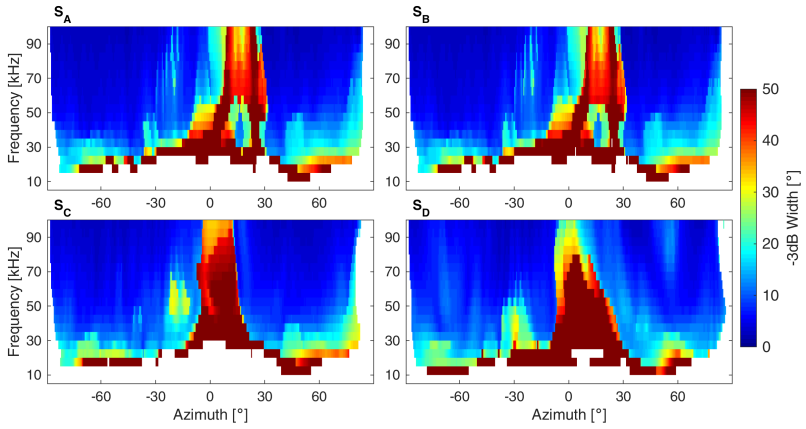

FIGURE 7.9: Same as Figure 7.8 but calculated at the right ear position.

This expected effect is confirmed throughout all data. The rate at which the focusing functions decrease with increasing $\Delta\varphi$, i.e., the resolution of the TR algorithm, is related to the frequency of the source function. The higher the frequency, the higher the possible resolution (see Section 3.2.2). The spatial resolution is estimated by analyzing the -3 dB width of $F(\varphi_i)$ for each given source position (Ing et al., 2005; Blomgren, Papanicolaou, and Zhao, 2002; Tsogka and Papanicolaou, 2002) and results are shown in Figures 7.8-7.10. In general, the results restate what can already be seen in the shape of the focusing functions; resolution decreases with decreasing frequency, and large amplitudes hamper the resolution, i.e., for source azimuths of around 15-20° to the ipsilateral side. This pattern can be seen throughout all cases, but more prominent for higher amplitude peaks, as in S_C and S_D. The same pattern appeared in a previous results; In Chapter 6, the direct signal was "cut out" of the recorded waveform and resolution was consequently greatly enhanced and of

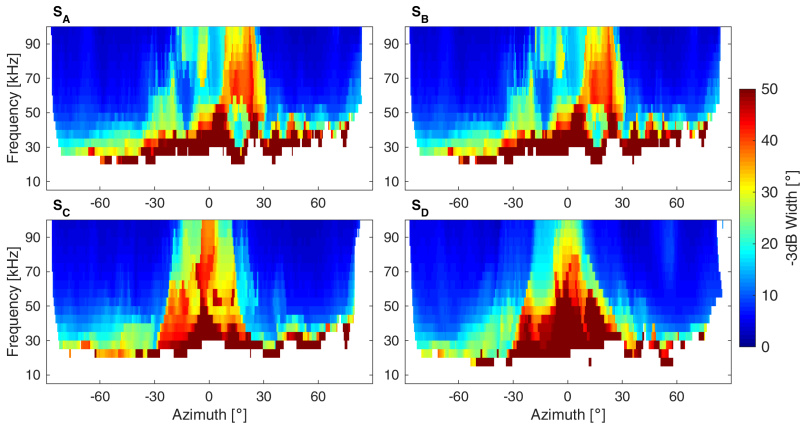

FIGURE 7.10: Same as Figure 7.8 but left/right ear averages.

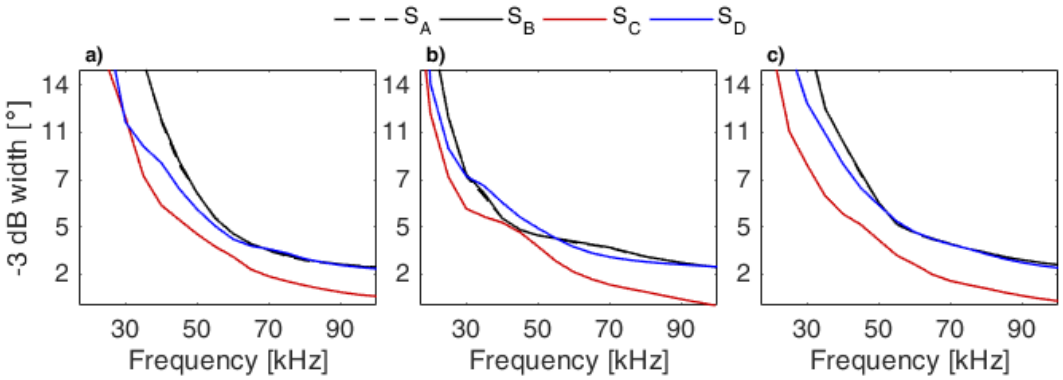

FIGURE 7.11: The smallest -3 dB widths for each frequency and case are shown for the left ear (**a)**), the right ear (**b)**) and their average (**c)**). The dashed line for case S_A is barely visible, since it is almost identical to the solid black line for case S_B.

similar value throughout all azimuths (and elevations). This "coda resolution" also coincided with the resolution for full waveforms, i.e., including the direct signal, wherever the direct signal was small in amplitude. Whichever type of signal is used for the TR algorithm, either the coda or full waveforms with small-amplitude direct signals, they both should, therefore, result in the same resolution. Figures 7.8-7.10 are evaluated by finding the smallest -3 dB width for each frequency across all azimuths, and results are shown in Figure 7.11. Following the previous considerations, this should represent the coda resolution of this system. The combination of shear waves and fats (S_C) increases the coda resolution throughout all frequencies. It notably decreases when shear waves are set to zero (S_D). The resolution then coincides with the cases without fats (S_A and S_B) for frequencies larger than ∼50 kHz.

7.4 Discussion

Amplitude, as well as ILD, results show similarities to other work. Oberrecht, Krysl, and Cranford simulated sound propagation in a short-beaked common dolphin's head using a 3D model obtained via CT-scans. They calculated the acoustic response of the left ear due to certain sound source azimuths (Oberrecht, Krysl, and Cranford, 2016, Figure 96.2), including reference data from an experimental study carried out by Norris and Harvey (Norris and Harvey, 1974). In the numerical study, the source function was a pure tone over a single cycle at 20 kHz and maximum pressure was found at around 20° to the left of the head, validating the experimental data. This pattern can also be seen in the results of this chapter, presented in Figure 7.5. Considering the most realistic case S_C, and a source frequency of 20 kHz, amplitudes at the left ear are indeed highest for a source azimuth of around -15 to -20°. Comparing all cases, it is most likely that the combination of fats and shear waves are key; flexural waves, such as guided lamb waves, along the pan bone, could induce new pressure waves in the fats. If they are in phase with the incident pressure, they could increase the amplitude of the waveforms received at the two ears (Fahy and Gardonio, 2007). This flexural wave mechanism of the pan bone and a resulting amplitude increase was proposed earlier by Cranford, Krysl, and Hildebrand (Cranford, Krysl, and Hildebrand, 2008) as a result of 3D simulations:

"Our FEM simulations suggest that the thinned posterior walls of the lower jaws are forced into a series of flexural waves by incoming sounds, provided that the sounds and bone have a specific set of characteristics. [...] One explanation of the flexural wave notion is that pressure (P) waves incident upon the mandibles are translated into P waves and shear (S) waves in the thin posterior bony shell, the pan bone, of the mandible or lower jaw. Once the P waves and S waves create flexing in the thin bony wall the sound will propagate into the internal mandibular fat bodies and through them to the bony ear complexes. [...] This mandibular mechanism depends on a number of factors including the geometry and elastic properties of the mandibles and adjacent soft tissues as well as the acoustic frequency and its angle of incidence."

Without fats (S_A and S_B), this peak is not prominent. With fats, but without elastic waves (S_D), the peak is less sharp in azimuth and smaller in amplitude. Popov and Supin measured a dolphin's auditory nerve response at the two ears using the auditory brainstem evoked response method[1] (Popov and Supin, 1991; Supin and Popov, 1993), which is also frequently used on humans (Long and Allen, 1984; Hecox and Galambos, 1974). The previously discussed amplitude peak and its increase in amplitude for higher frequencies can also be found in experimental results by Supin and Popov. Again, without shear waves (S_D), high-frequency peaks at respective

[1] This is a non-invasive method that uses electrodes placed on the head to measure how the brain processes sounds.

azimuths are missing. Furthermore, they find maximum ILDs to be around 20 dB, similar to the results in this chapter.

The presented TR procedure lacks comparable data by others. This part of the study should be considered a parametric test of how waveforms could change in complexity due to different head parts, and therefore complement Chapter 6. If and how the animal processes the waveforms remains speculative and has been discussed in more detail in Chapters 5 and 6. The best resolution is achieved through the combination of mandibular fats and an elastic mandible. S-waves and surface waves travel slower than compressional waves. They introduce multi-layer propagation paths, rendering a more complex waveform in the bone, which in turn, could introduce new pressure fluctuations in the fats, and, consequently, increase the resolution.

This study was able to recreate, with a rather simple 2D model, some findings on amplitude and ILD patterns, as well as on vibroacoustic mechanisms of wave propagation along and inside a dolphin's mandible. However, all similarities of findings between this study and others should be taken with a grain of salt. The two-dimensional model of the head has many limitations regarding its realism. The most prominent and obvious problem is the dimensionality. 2D modeling of a 3D real-life problem should always be seen as a preliminary step, and same holds true for this study. While the results have surprisingly strong similarity to real data, they should, of course, be validated in 3D in future work. However, the low computational cost of running 2D simulations and the easy creation and meshing of structures, compared to the 3D case, suggest that 2D simulations are helpful in obtaining first insights into a problem and maybe avoiding time-costly larger 3D simulations. The idea of modeling a full dolphin's head in 3D, ideally as realistically as possible, poses many problems that need to be considered by anyone, hopefully, someone, who will continue this work. Chapter 5 shows the many steps required to model the skull, e.g., segmenting CT-scan data and finding the right material parameters. One can imagine how difficult this would be when the anatomies to be modeled are almost liquid (such as fats), may have changed compared to how they were when the animal was still alive (due to blood loss), or are complex multi-layered structures like the mandibular fats (Koopman et al., 2006; Norris and Harvey, 1974). Soldevilla et al. show the many steps required to measure material properties in soft tissues, including dissection of the animal's head (Soldevilla et al., 2005). Another illustration of the impressive amount of work needed to model real heads can be found in the work of Cranford (Cranford, 2012; Cranford et al., 2008). However, as Gray and Rogers already noted, "the strong temperature sensitivity of fatty tissue properties combined with the uncertainty of in vivo tissue temperature distributions raises doubts over the utility of data collected from ex vivo samples" (Gray and Rogers, 2017).

Another limitation of the 2D model is the complexity of the parts of the head. All of them are drastically simplified for various reasons. The mandible, which has been

modeled and discussed in previous chapters, is considered to be solid, missing teeth and, to some extent, the mandibular foramen. The element size of 2mm, ensuring suitable computational speed of the simulations limits the detail of the geometry. The fats, as already mentioned, are known to have several layers of different sound speeds. In this study, several values of sound speeds, taken from Norris and Harvey (Norris and Harvey, 1974), are averaged since the exact geometrical extent of the different layers is unknown. It is even more surprising to see that the fats have such a strong effect on the wavefield (amplitude amplification and increase in complexity of the waveforms), having quite similar material properties to the surrounding tissue. It can only be suspected that these effects would increase with more realistic and complex models. All other parts of the head are defined as a homogeneous medium named "tissue". While most parts are, indeed, soft tissues, some of them have notably different sound speeds than others. Skin, muscles, and tissues, all are considered to be same, due to the same reasons why fats are considered to be homogeneous; differentiation between various soft tissues would require dissections or reliable CT-scan data, both of which are not available.

Some attempts have been made to experimentally measure the attenuation of cetacean soft tissues, e.g., by Gray and Rogers, but the results were averages of 3 cm long cross-sections, sampling mandibular fats, and a mixture of fatty, connective, and muscle tissues in the temporal region (Gray and Rogers, 2017). Furthermore, the data was obtained via ultrasound transducers emitting frequencies larger than 1 MHz, which lies out of the range of interest. Also, TR is most sensitive to phase rather than amplitude; hence, the results should be affected only marginally. Attenuation in soft tissues is therefore neglected due to the absence of reliable data and should be topic of further research.

In conclusion, the model is created to be simple but still have some similarity to a real head.

7.5 Conclusion

Elastic waves in the mandible interact with the surrounding fats, which could be beneficial to acoustic source localization of the animal. Not only does this combination amplify sound for certain source azimuths, it also increases complexity of the waveforms at the ears. Speculating that the animal can analyze sounds similar to the proposed correlation-based TR algorithm, it would benefit from the vibrational behavior of the mandible and its acoustic interaction with the surrounding fats.

Chapter 8

Conclusion

This work shows no indication that dolphins could rely on skull-related spectral cues alone for the localization of median-plane sources, as opposed to what is observed, e.g., for humans and their pinnae; the numerically modeled skull-related transfer function is not characterized by sharp maxima or minima changing monotonously as a function of source elevation. However, if this is also true for a dolphin's *head*-related transfer function needs to be proved or disproved by experiments and simulations on whole heads. It could be speculated that, even in the absence of pinnae, other adaptations in the anatomy of a dolphin's head could give rise to well-defined notches; these, in turn, would favor the hypothesis that dolphins determine source elevation in a similar way as humans, i.e., that they are sensitive to certain spectral colorations of the HRTF that clearly depend on elevation. Especially the mandibular fats and their possibly complex composition of celerities and densities need to be further investigated to fully understand their role on sound propagation pathways in heads of dolphins since they are often considered to play a vital role in auditory capabilities of dolphins. The 2D simulations presented in this work suggest that they do have a notable influence on amplitudes and waveforms perceived at the ears. This work suggests another possible explanation. The effects of mandible and cranium on wave propagation are strongly dependent on source location, with equal sensitivity to changes in source azimuth and elevation: in particular, the reverberated "coda" waveform of a perceived sound contains sufficient information to accurately localize its source, whether in the horizontal or median plane. Because an echolocating dolphin naturally "knows" the signal it emits, and whose echoes it learns to recognize, the algorithm encoded in the odontocete auditory system might be based on correlation of the waveforms of heard sounds with those of a library of biosonar echoes, similar to the proposed time-reversal algorithm. This can be described as significantly more "sophisticated" than previously postulated spectral-cue-based localization mechanisms, pointing to unknown features of the dolphin's ear-brain system that deserve further study.

Interdisciplinary research will be necessary to eventually obtain a thorough understanding of the auditory processing of dolphins. While behavioral experiments

are the foundation of knowledge on the audition of marine mammals, further numerical modeling of and experiments on wave propagation in heads of dolphins will be required to confirm or disprove the proposed auditory mechanisms.

Appendix A

Modal analysis theory

This Appendix serves as supplementary material to Chapter 5. It presents the theory of numerical and experimental modal analysis in detail.

A.1 Finite-element modal analysis

In order to understand modal analysis through FEM, let us consider a simple one-dimensional spring, as shown in Figure A.1. Newton's second law of motion, which is a second order differential equation, describes the force acting on the mass m, when displaced from rest position x by an arbitrary force $f(t)$:

$$m\ddot{x} + c\dot{x} + kx = f(t) \tag{A.1}$$

Here, k is the stiffness of the spring, and c is the damping factor. The time derivatives $\dot{x}$ and $\ddot{x}$ describe velocity and acceleration respectively. In modal analysis, the exact motion of the spring is not relevant since one is only interested in finding the resonant frequencies and mode shapes of the object. Considering free vibration, in which no forces are acting on the object, Equation A.1 can be rewritten as

$$m\ddot{x} + kx = 0, \tag{A.2}$$

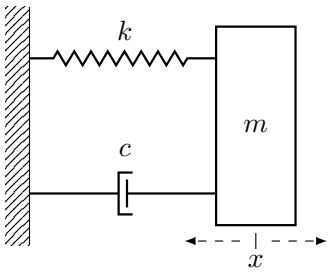

FIGURE A.1: Sketch of a one-dimensional spring. When displaced from rest position x, the motion of a spring with mass m depends on stiffness k and damping factor c. The resonant frequency can be calculated through $\sqrt{k/m}$.

if damping is neglected ($c = 0$), which is common practice in modal analysis. Not only does it simplify the mathematical problem, but the effect of damping can also be determined after the solution is found for the undamped case, if this is of further interest in the study (Ewins, 1984). Assuming harmonic motion, the solution to Equation A.2 writes

$$x(t) = x_0 e^{i\omega t}, \tag{A.3}$$

with time t and the undamped resonant frequency ω. Substituting Equation A.3 into Equation A.2 yields

$$-m\omega^2 x_0 e^{i\omega t} + k x_0 e^{i\omega t} = 0, \tag{A.4}$$

which has the solution

$$\omega = \sqrt{\frac{k}{m}}. \tag{A.5}$$

This example of a one-dimensional spring only has one degree of freedom and, therefore, only one resonant frequency. However, most real-life problems are far more complicated than calculating the motion of such an oscillator. Finding the resonant frequencies and corresponding mode shapes of complex structures is frequently done via FEM. The object is broken down into a finite number of elements, connected at grid points, called nodes. Values of mass and stiffness are assigned to N nodes, creating a system of N differential equations to be solved, i.e., N degrees of freedom. The system of equations (one for each degree of freedom) can then be written in matrix form, i.e.,

$$[M][\ddot{X}] + [C][\dot{X}] + [K][X] = [F], \tag{A.6}$$

with the mass matrix M, damping matrix C, stiffness matrix K and the external force F. As before, damping and external forces can be neglected when calculating resonant frequencies and mode shapes, and Equation A.6 can be simplified to

$$[M][\ddot{X}] + [K][X] = 0, \tag{A.7}$$

with the solution

$$[X] = [a]e^{i[\omega]t}. \tag{A.8}$$

Here, $[a]$ is the vector of displacement amplitudes, i.e., eigenvectors, and $[\omega]$ the vector of resonant frequencies. For each resonant frequency ω_k, the equation then reads

$$[K][a]_k - \lambda_k [M][a]_k = 0 \tag{A.9}$$

where $\lambda = \omega^2$. Finite-element software packages, such as COMSOL Multiphysics, solve this system of equations, describing the approximate dynamic motion of the structure, given material parameters, such as Young's modulus, Poisson's ratio, and density are defined in order to calculate M and K.

A.2 Experimental modal analysis

Resonant frequencies can also be determined experimentally. Following Perconti (Perconti, 1992), and taking the Laplace transform of both sides of Equation A.6, it can be rewritten as

$$(s^2[M] + s[C] + [K])[X(s)] = [F(s)]. \tag{A.10}$$

The system's impedance matrix $B(s)$ is defined as

$$[B(s)] = s^2[M] + s[C] + [K], \tag{A.11}$$

with its inverse $H = B^{-1}$. Equation A.10 can therefore be simplified to

$$[X(s)] = [H(s)][F(s)]. \tag{A.12}$$

The transfer matrix H describes the response of the system for a given excitation F. Each matrix element h describes the response of the system due to excitation at one point and response at another. For example, the transfer function

$$h_{ij}(s) = \frac{X_i(s)}{F_j(s)} \tag{A.13}$$

describes the response for an excitation at point j measured at point i. This can be done experimentally through, e.g., striking the object with a hammer at point j and recording displacement (or any time derivative) at point j. It can be seen (e.g., Perconti, 1992) that the transfer matrix H can be used to find the resonant frequencies and modal shapes: For a system of N degrees of freedom, each transfer function can be written as

$$h_{ij}(s) = \frac{b_1 s^{2n-2} + b_2 s^{2n-1} + \cdots + b_{2n-1}s + b_{2n-2}}{det[B(s)]}. \tag{A.14}$$

The denominator can then be expressed as the product of the poles of the transfer function, i.e.,

$$det[B(s)] = A(s - p_n)(s - p_n^*)(s - p_{n-1})(s - p_{n-1}^*) \cdots (s - p_1)(s - p_1^*), \tag{A.15}$$

with the constant A, poles p and their complex conjugates p^*. The transfer matrix H then writes

$$[H(s)] = \sum_{k=1}^{n} \left[\frac{[A_k]}{s - p_k} + \frac{[A_k^*]}{s - p_k^*} \right]. \tag{A.16}$$

The points at which the transfer matrix goes to infinity ($s = p_k$) are the resonance points of the object, and each pair p_k and p_k^* defines a resonant mode with resonant

frequency ω_k through the damping coefficient σ_k:

$$\begin{aligned} p_k &= -\sigma_k + i\omega_k, \\ p_k^* &= -\sigma_k - i\omega_k. \end{aligned} \tag{A.17}$$

Appendix B

Photographs of the experimental setup

This Appendix shows photographs taken during setup of the experiment presented in Chapter 6.

FIGURE B.1: Photograph of the outdoor pool in which the experiment was conducted. It is located at the Institut Jean le Rond d'Alembert in Saint-Cyr-l'École, France.

FIGURE B.2: Photograph of the skull specimen taken from top down.

FIGURE B.3: Photograph of the accelerometer glued to the mandible. Each accelerometer was glued to the mandible with super glue and coated with flexible adhesive to keep water from touching the equipment.

FIGURE B.4: Photograph of the damaged skull. During preparation of the experiment, small collateral damage, as seen in the photograph, was fixed with super glue.

FIGURE B.5: Photograph of the rotation system. An electronic (house-made) rotation device was mounted on a large metal plank. The plank could be moved over the water and positioned at a desired distance away from the transducer.

FIGURE B.6: Photograph of the experimental setup. The skull was placed 2 meters away from the loudspeaker and rotated around the vertical axis by the electronic rotation device.

Appendix C

Focusing functions of 2D simulations

This Appendix serves as supplementary material to Chapter 7. Each page shows focusing functions for all four scenarios and one frequency. For brevity, only three frequencies are shown; 20, 50, and 90 kHz.

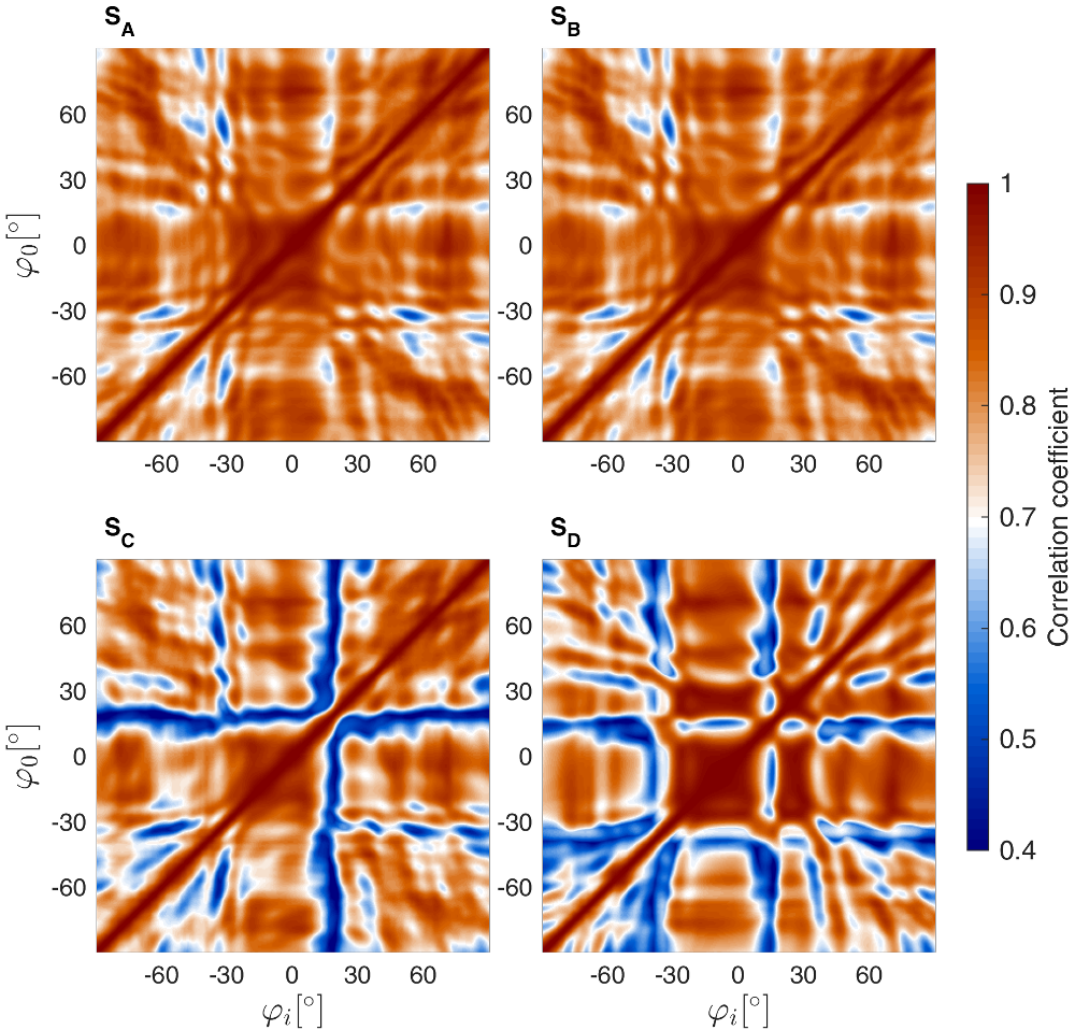

FIGURE C.1: Focusing functions using signals calculated at the left ear and a source frequency of 20 kHz for scenario S_A (**top left**), S_B (**top right**), S_C (**bottom left**), and S_D (**bottom right**). Each row of a given panel shows, accordingly, the maximum cross correlation value between the signal associated with one particular source (defined by its azimuth φ_0 on the vertical axis), and those of all other sources (azimuths φ_i on the horizontal axis).

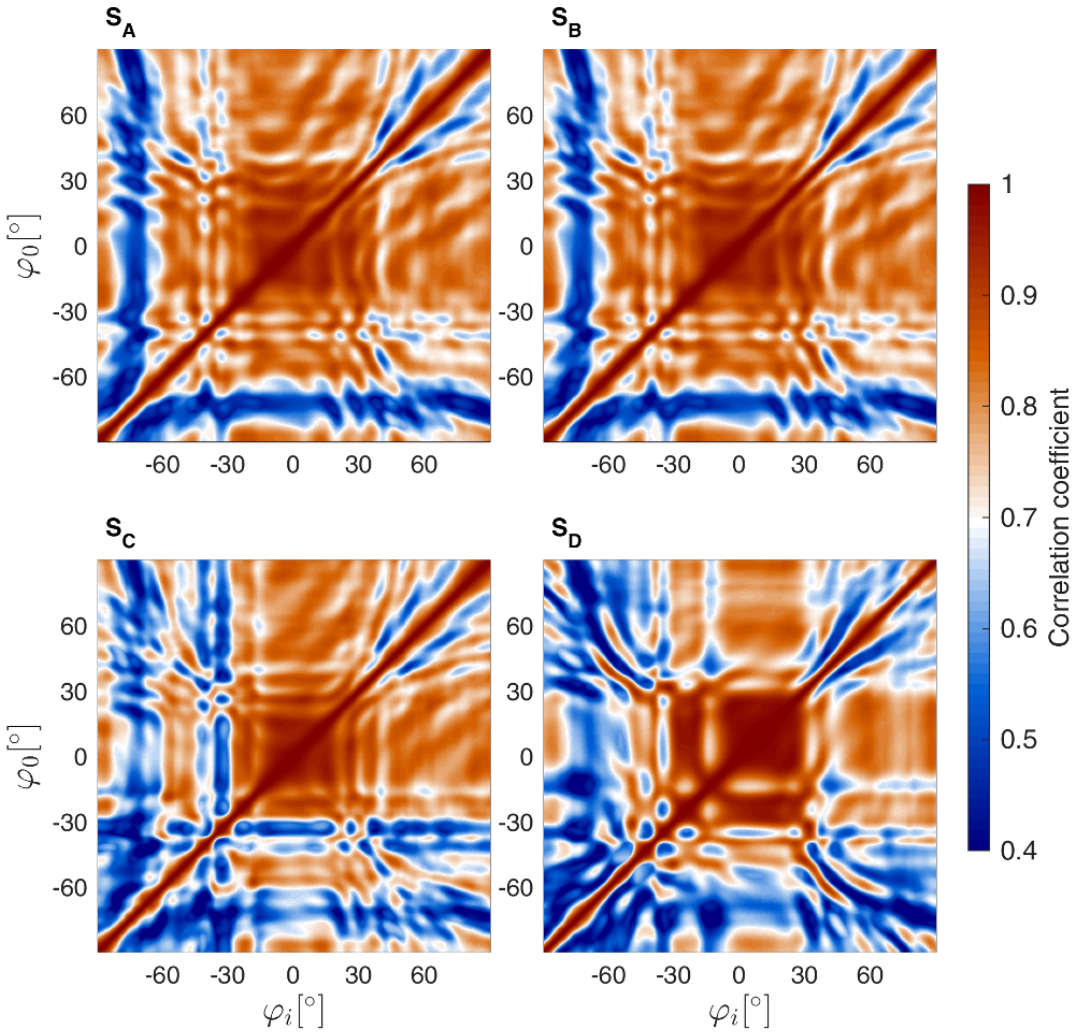

FIGURE C.2: Same as Figure C.1 but calculated at the right ear position.

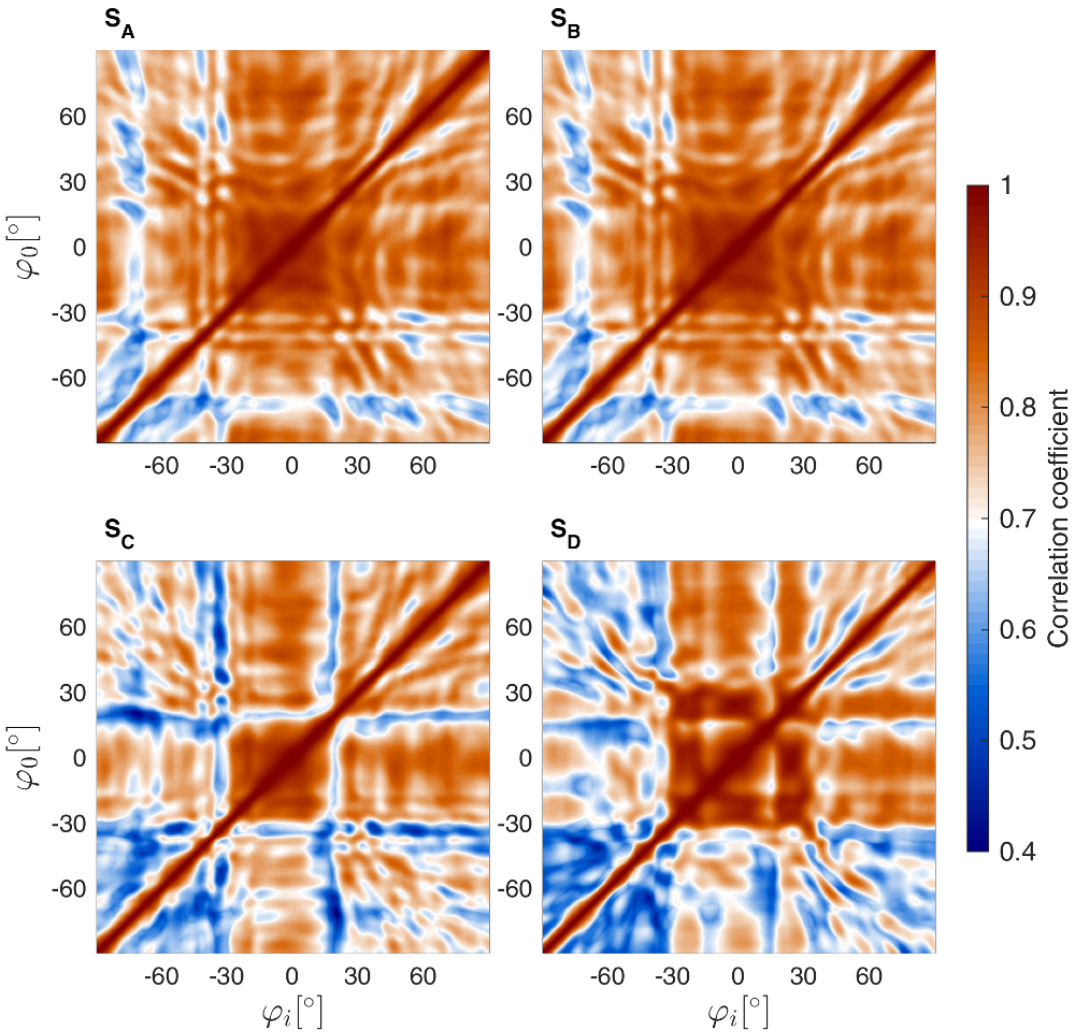

FIGURE C.3: Same as Figure C.1 but left/right ear averages.

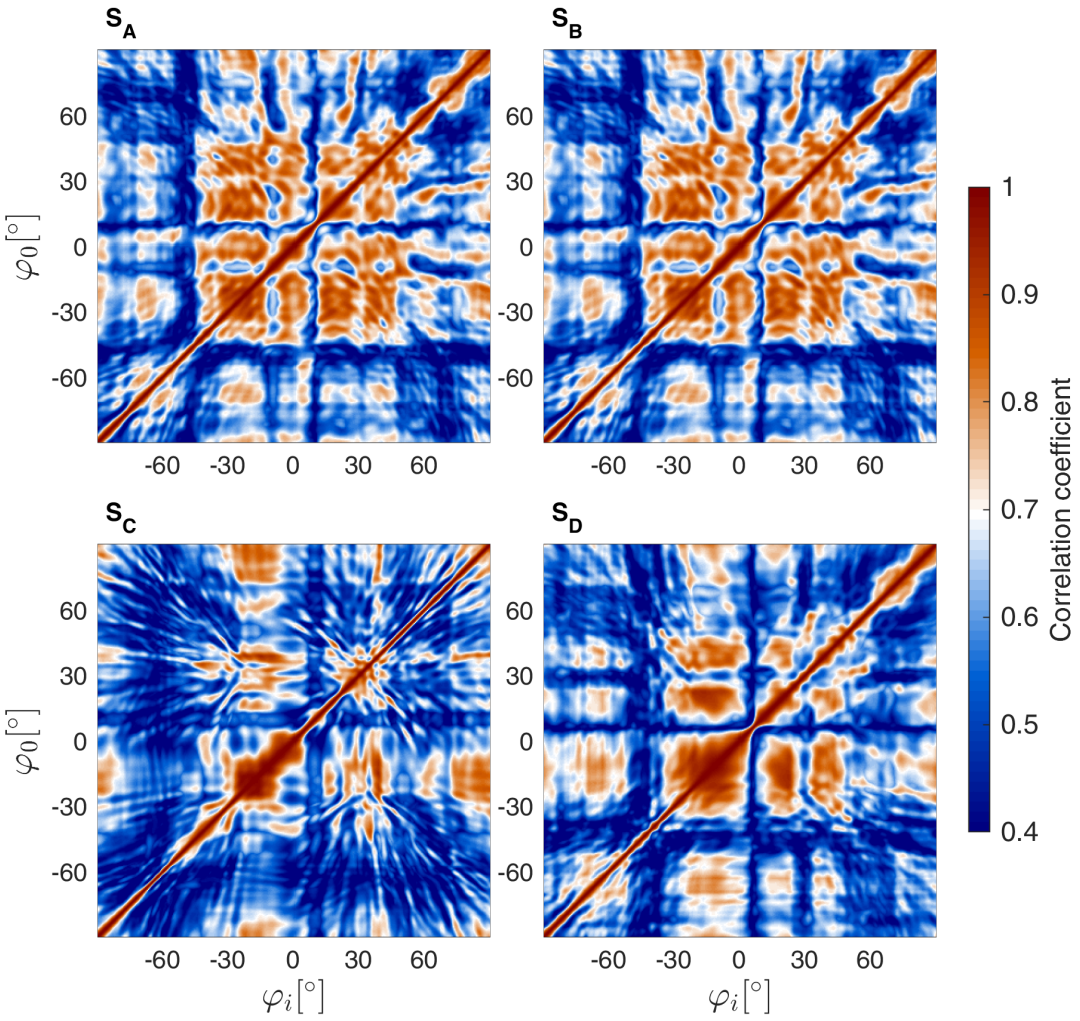

FIGURE C.4: Same as Figure C.1 but calculated at the left ear position and using a source frequency of 50 kHz.

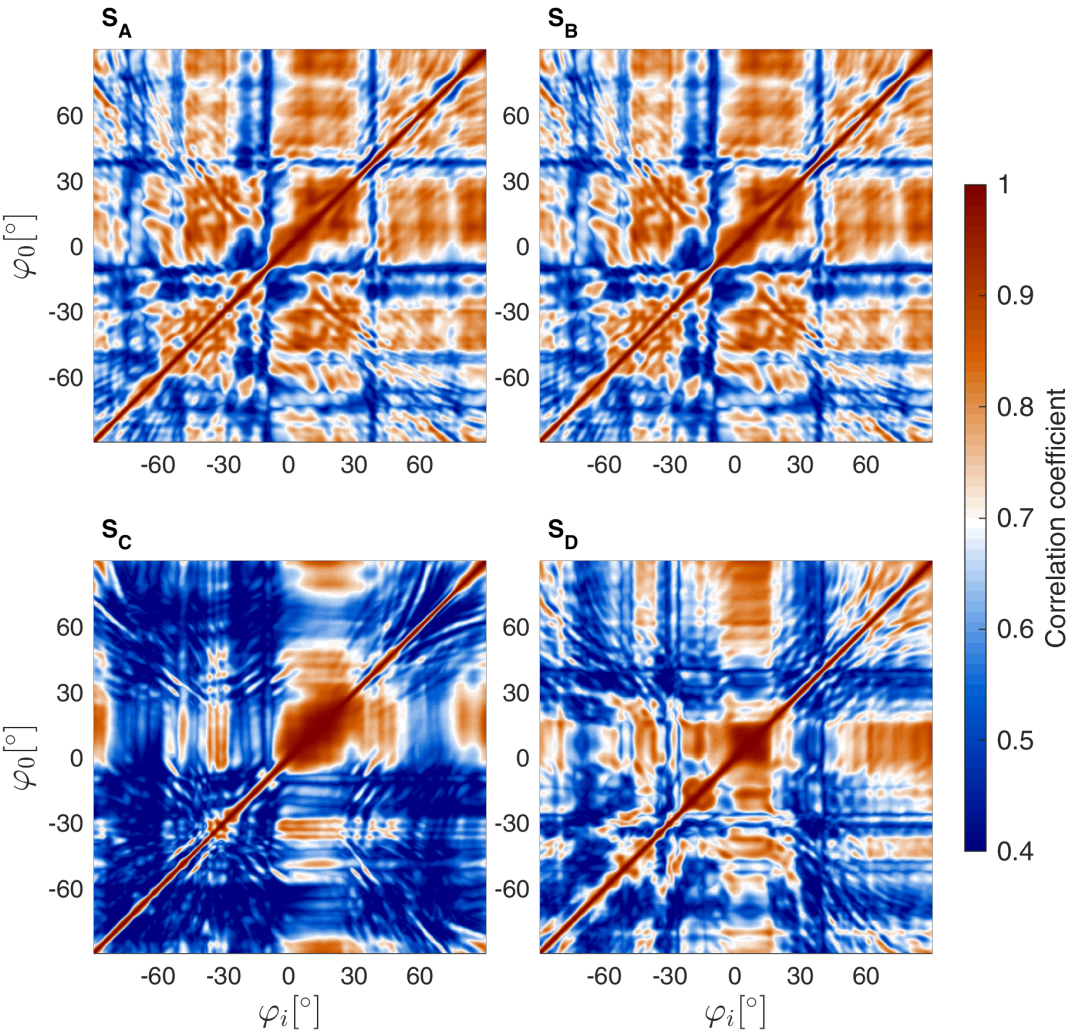

FIGURE C.5: Same as Figure C.4 but calculated at the right ear position.

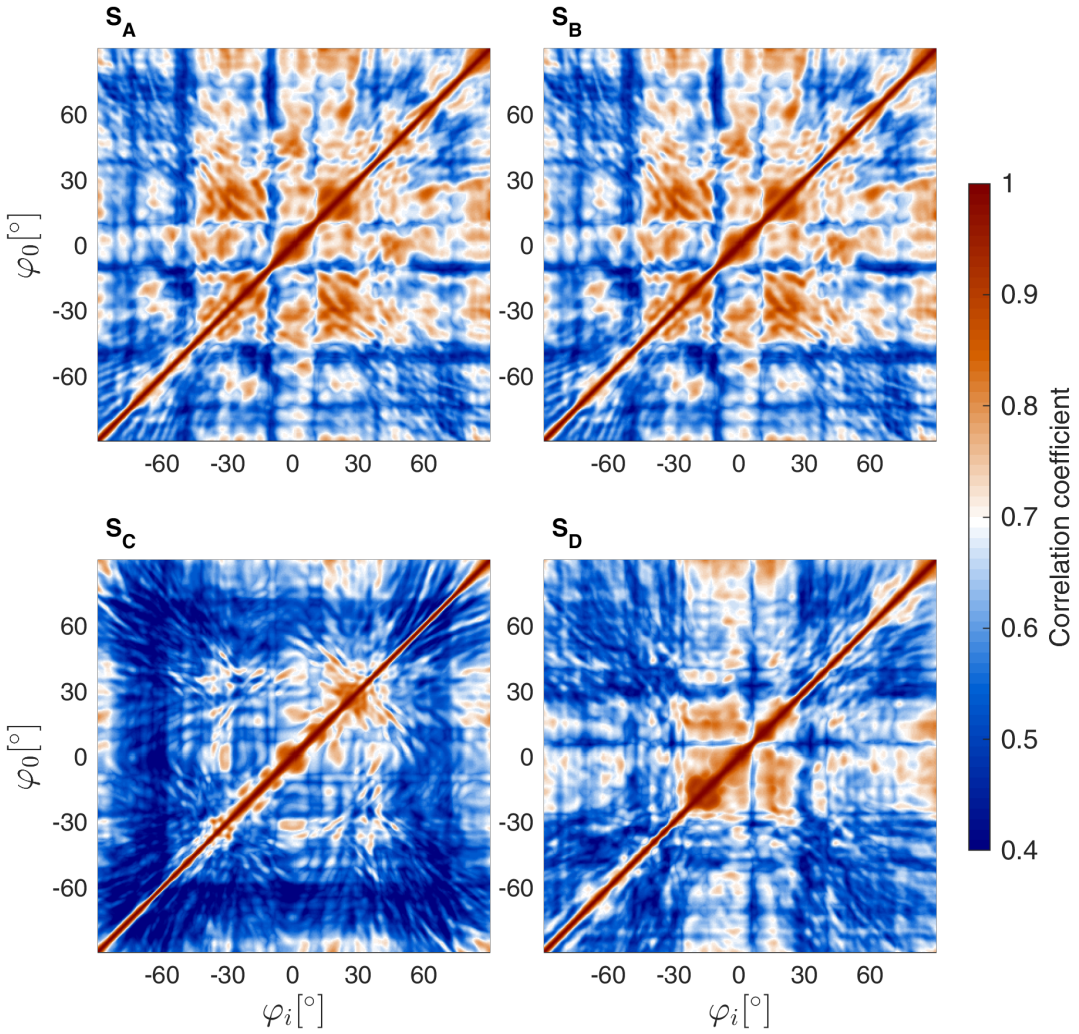

FIGURE C.6: Same as Figure C.4 but left/right ear averages.

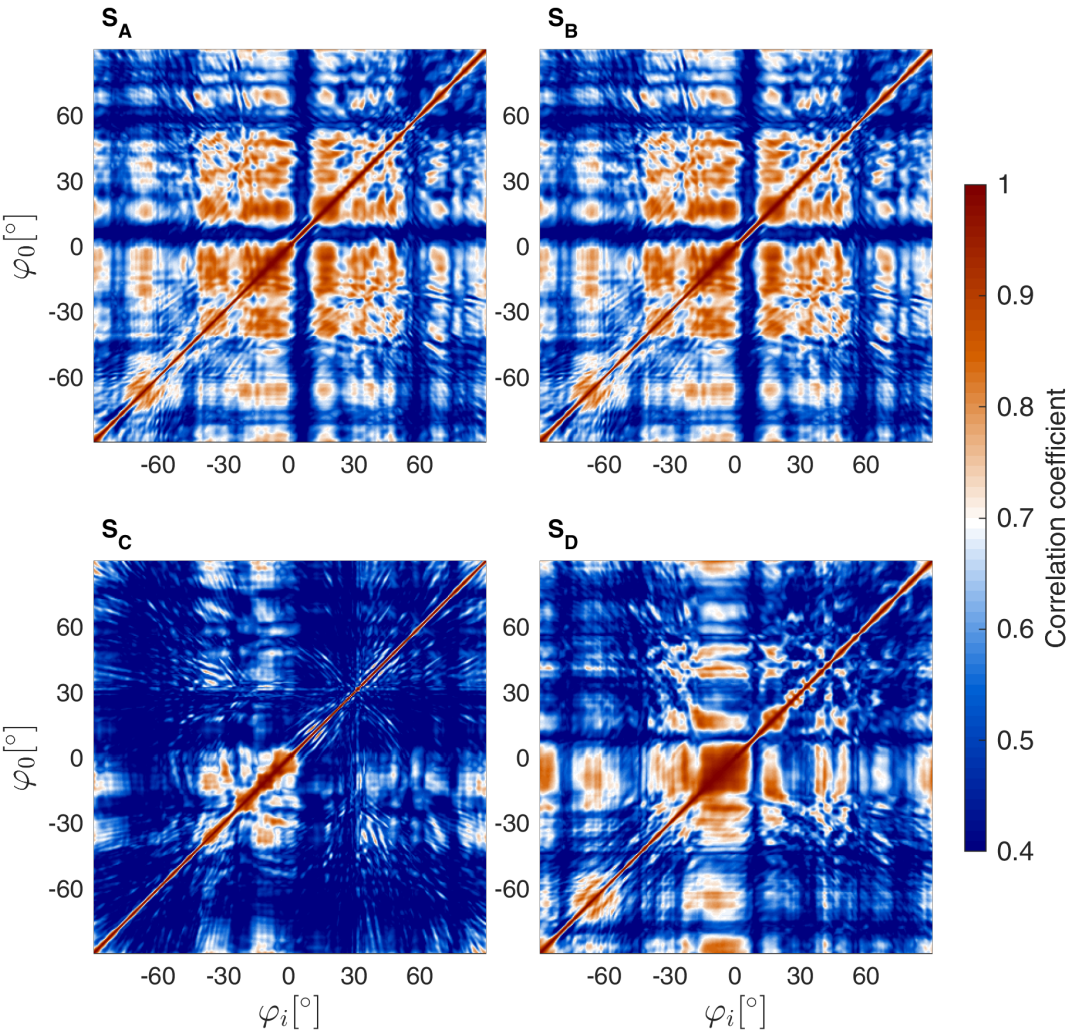

FIGURE C.7: Same as Figure C.1 but calculated at the left ear position and using a source frequency of 90 kHz.

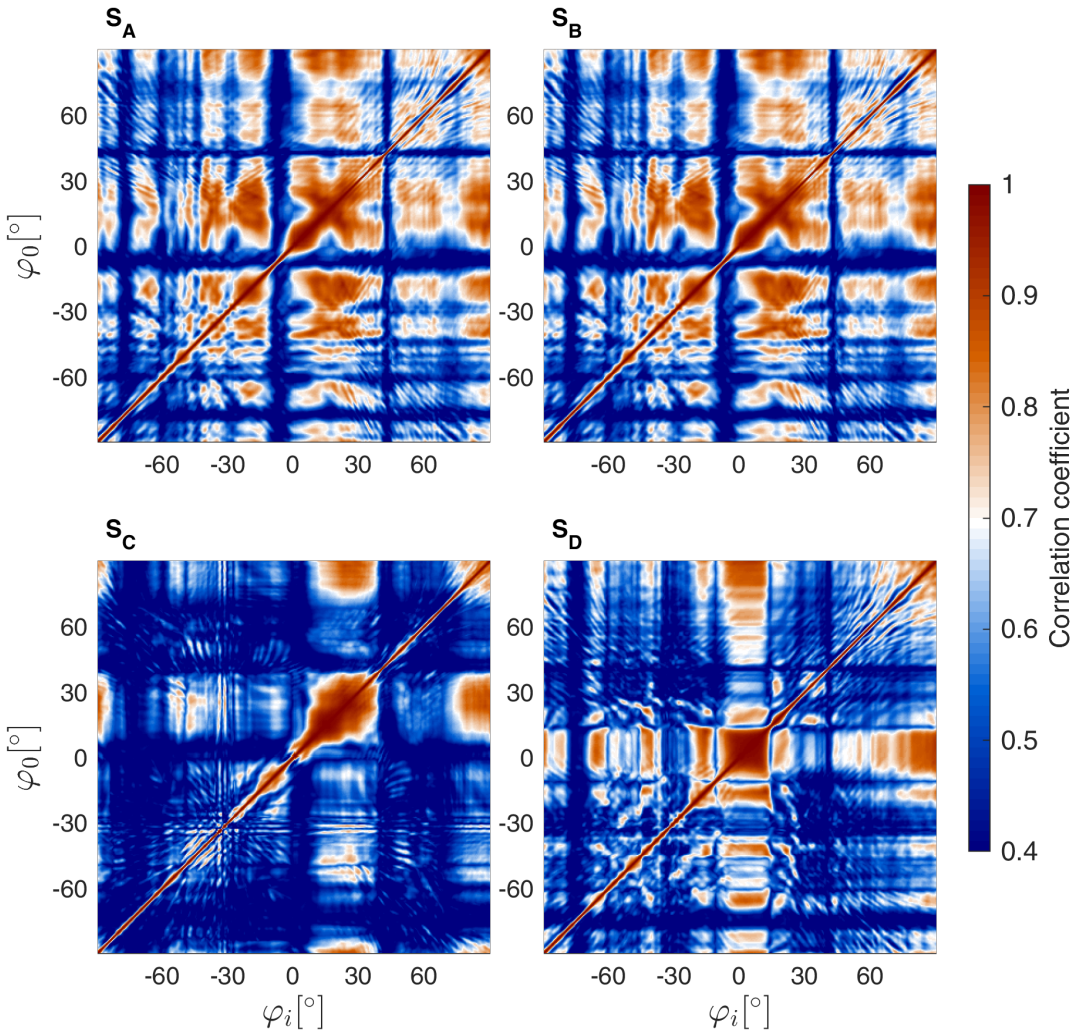

FIGURE C.8: Same as Figure C.7 but calculated at the right ear position.

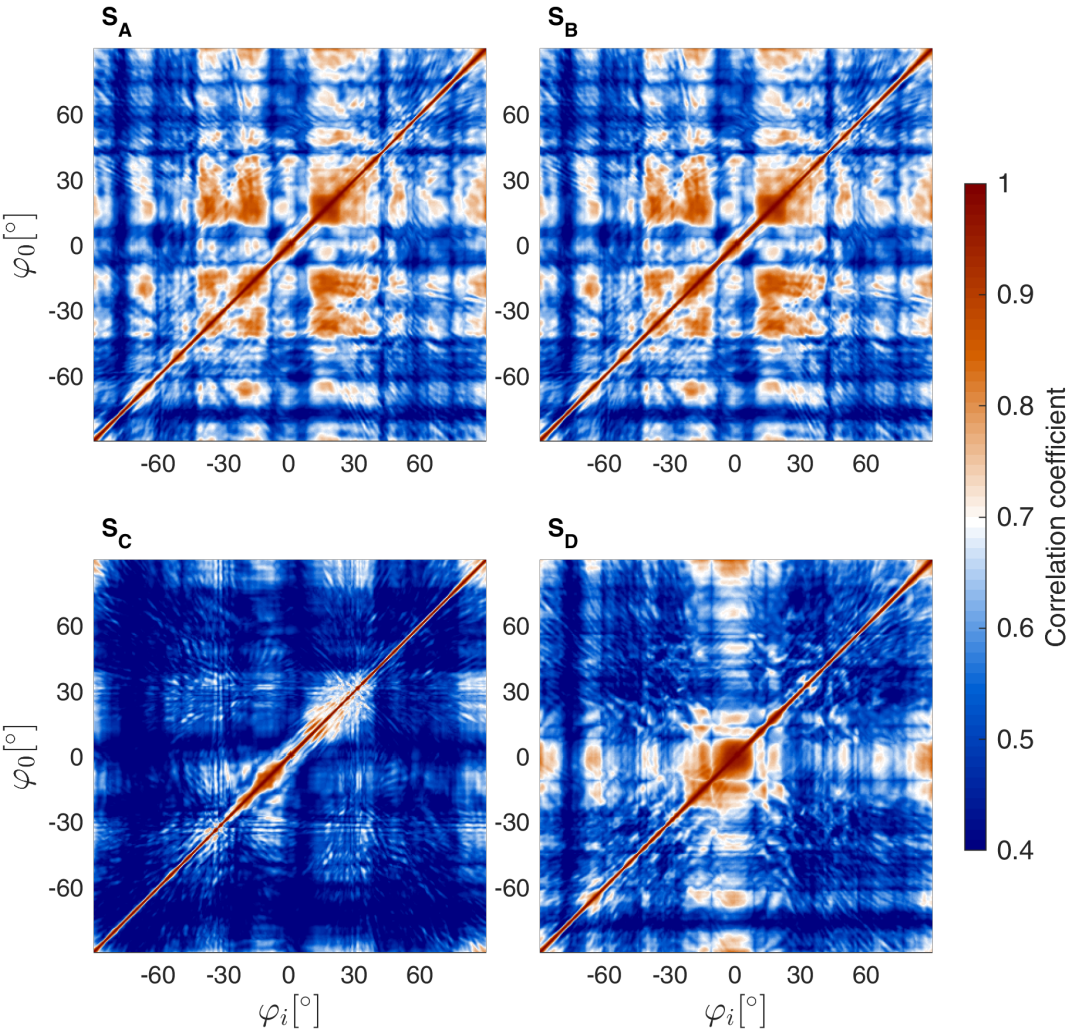

FIGURE C.9: Same as Figure C.7 but left/right ear averages.

Bibliography

Adams, Douglas (2010). *The Ultimate Hitchhiker's Guide to the Galaxy: Five Novels in One Outrageous Volume*. Del Rey.

Agterberg, Martijn JH et al. (2011). "Improved horizontal directional hearing in bone conduction device users with acquired unilateral conductive hearing loss". In: *Journal of the Association for Research in Otolaryngology* 12.1, pp. 1–11.

Aki, Keiiti (1980). *Quantitative seismology*. WH Freeman and Co.

Anonymous (1880). "Navigation in Fogs". In: *Scientific American* 43.1, pp. 3–3.

Aroyan, James L (1996). *Three-dimensional numerical simulation of biosonar signal emission and reception in the common dolphin*. University of California, Santa Cruz.

— (2001). "Three-dimensional modeling of hearing in Delphinus delphis". In: *The Journal of the Acoustical Society of America* 110.6, pp. 3305–3318.

Aroyan, James L et al. (1992). "Computer modeling of acoustic beam formation in D elphinusdelphis". In: *The Journal of the Acoustical Society of America* 92.5, pp. 2539–2545.

Aroyan, James L et al. (2000). "Acoustic models of sound production and propagation". In: *Hearing by whales and dolphins*. Springer, pp. 409–469.

Ary, William et al. (2016). "Functional morphology and symmetry in the odontocete ear complex". In: *The Effects of Noise on Aquatic Life II*. Springer, pp. 57–64.

Au, Whitlow WL (2004). "Dolphin sonar detection and discrimination capabilities". In: *The Journal of the Acoustical Society of America* 115.5, pp. 2614–2614.

— (2012). *The sonar of dolphins*. Springer Science & Business Media.

Au, Whitlow WL and Richard R Fay (2012). *Hearing by whales and dolphins*. Vol. 12. Springer Science & Business Media.

Au, Whitlow WL and Mardi C Hastings (2008). *Principles of marine bioacoustics*. Springer.

Au, Whitlow WL and Patrick WB Moore (1984). "Receiving beam patterns and directivity indices of the Atlantic bottlenose dolphin T ursiopstruncatus". In: *The Journal of the Acoustical Society of America* 75.1, pp. 255–262.

Avitabile, Peter (2001). "Experimental modal analysis". In: *Sound and vibration* 35.1, pp. 20–31.

Backus, George (1970). "A geometrical picture of anisotropic elastic tensors". In: *Reviews of geophysics* 8.3, pp. 633–671.

Barroso, Celia, Ted W Cranford, and Annalisa Berta (2012). "Shape analysis of odontocete mandibles: functional and evolutionary implications". In: *Journal of Morphology* 273.9, pp. 1021–1030.

Batteau, Dwight W (1967). "The role of the pinna in human localization". In: *Proc. R. Soc. Lond. B* 168.1011, pp. 158–180.

Bauer, Benjamin B and Emil L Torick (1966). "Experimental studies in underwater directional communication". In: *The Journal of the Acoustical Society of America* 39.1, pp. 25–34.

Bel'kovich, Vladimir M et al. (1969). "Echolocating capabilities of the common dolphin (Delphinus delphis)". In: *Zool. Zhurn* 48, pp. 876–883.

Benade, A. H. (1990). *Fundamentals of Musical Acoustics*. Dover Publications, New York.

Benoit-Bird, Kelly J and Whitlow WL Au (2009). "Cooperative prey herding by the pelagic dolphin, Stenella longirostris". In: *The Journal of the Acoustical Society of America* 125.1, pp. 125–137.

Bernard, Simon, Quentin Grimal, and Pascal Laugier (2014). "Resonant ultrasound spectroscopy for viscoelastic characterization of anisotropic attenuative solid materials". In: *The Journal of the Acoustical Society of America* 135.5, pp. 2601–2613.

Bernard, Simon et al. (2016). "Elasticity–density and viscoelasticity–density relationships at the tibia mid-diaphysis assessed from resonant ultrasound spectroscopy measurements". In: *Biomechanics and modeling in mechanobiology* 15.1, pp. 97–109.

Beston, Henry (2003). *The outermost house: A year of life on the great beach of Cape Cod*. Macmillan.

Betzig, Eric J, Jay K Trautman, et al. (1991). "Breaking the diffraction barrier: optical microscopy on a nanometric scale". In: *Science* 251.5000, p. 1468.

Blauert, Jens (1969). "Sound localization in the median plane". In: *Acta Acustica united with Acustica* 22.4, pp. 205–213.

— (1997). *Spatial hearing: the psychophysics of human sound localization*. MIT press.

Bleistein, Norman (2012). *Mathematical methods for wave phenomena*. Academic Press.

Blomgren, Peter, George Papanicolaou, and Hongkai Zhao (2002). "Super-resolution in time-reversal acoustics". In: *The Journal of the Acoustical Society of America* 111.1, pp. 230–248.

Boschi, Lapo, Irene Molinari, and Michael Reinwald (2018). "A simple method for earthquake location by surface-wave time reversal". In: *Geophysical Journal International* 215.1, pp. 1–21.

Boschi, Lapo and Cornelis Weemstra (2015). "Stationary-phase integrals in the cross correlation of ambient noise". In: *Reviews of Geophysics* 53.2, pp. 411–451.

Branstetter, Brian K and Eduardo Mercado III (2006). "Sound localization by cetaceans". In: *International Journal of Comparative Psychology* 19.1.

Brill, Randall L, Patrick WB Moore, and Lois A Dankiewicz (2001). "Assessment of dolphin (Tursiops truncatus) auditory sensitivity and hearing loss using jawphones". In: *The Journal of the Acoustical Society of America* 109.4, pp. 1717–1722.

Brill, Randall L et al. (1988). "Behavioral evidence for hearing through the lower jaw by an echolocating dolphin (Tursiops truncatus)". In: *Marine Mammal Science* 4.3, pp. 223–230.

Brown, Charles H (1994). "Sound localization". In: *Comparative hearing: mammals*. Springer, pp. 57–96.

Brungart, Douglas S, Nathaniel I Durlach, and William M Rabinowitz (1999). "Auditory localization of nearby sources. II. Localization of a broadband source". In: *The Journal of the Acoustical Society of America* 106.4, pp. 1956–1968.

Bullock, Theodore H. and Vladimir S. Gurevich (1979). "Soviet Literature on the Nervous System and Psychobiology of Cetacea". In: *International Review of Neurobiology*. Ed. by John R. Smythies and Ronald J. Bradley. Vol. 21. Academic Press, pp. 47 –127.

Burns, Marshall (1993). "The STL format". In: *Burns M. Automated fabrication: improving productivity in manufacturing. Prentice-Hall, Inc*.

Buroojy, Thomas William (2008). U.S. Patent No. 12/167,786.

Butler, Robert A and Krystyna Belendiuk (1969). "Monaural and binaural localization of noise bursts vertically in the median sagittal plane". In: *Journal of the Auditory Research* 3, pp. 230–235.

Butler, Robert A, Richard A Humanski, and Alan D Musicant (1990). "Binaural and monaural localization of sound in two-dimensional space". In: *Perception* 19.2, pp. 241–256.

Carcangiu, Sara, Augusto Montisci, and Renato Forcinetti (2015). "Numerical Simulation of Wave Propagation". In: *Ultrasonic Nondestructive Evaluation Systems*. Springer, pp. 17–45.

Carstensen, Edwin L (1979). "Absorption of sound in tissues". In: *Ultrasonic Tissue Characterization II* 525, pp. 29–40.

Cassereau, Didier and Mathias Fink (1992). "Time-reversal of ultrasonic fields. III. Theory of the closed time-reversal cavity". In: *IEEE transactions on ultrasonics, ferroelectrics, and frequency control* 39.5, pp. 579–592.

Catheline, S et al. (2008). "Time reversal of elastic waves in soft solids". In: *Physical review letters* 100.6, p. 064301.

Catheline, Stefan et al. (2007). "Acoustic source localization model using in-skull reverberation and time reversal". In: *Applied physics letters* 90.6, p. 063902.

Comsol (2018). *Comsol Multiphysics®(Version 5.3a), Stockholm, Sweden*. URL: www.comsol.com.

Conti, Stephane G, Philippe Roux, and William A Kuperman (2007). "Near-field time-reversal amplification". In: *The Journal of the Acoustical Society of America* 121.6, pp. 3602–3606.

Courant, Richard, Kurt Friedrichs, and Hans Lewy (1928). "Über die partiellen Differenzengleichungen der mathematischen Physik". In: *Mathematische Annalen* 100.1, pp. 32–74.

Cozzi, Bruno, Stefan Huggenberger, and Helmut A Oelschläger (2016). *Anatomy of dolphins: insights into body structure and function*. Academic Press.

Cranford, Ted W (2012). *Building a Virtual Model of a Baleen Whale: Phase 2*. Tech. rep. Quantitative Morphology Consulting, San Diego, CA.

Cranford, Ted W, Petr Krysl, and Mats Amundin (2010). "A new acoustic portal into the odontocete ear and vibrational analysis of the tympanoperiotic complex". In: *PLoS One* 5.8, e11927.

Cranford, Ted W, Petr Krysl, and John A Hildebrand (2008). "Acoustic pathways revealed: simulated sound transmission and reception in Cuvier's beaked whale (Ziphius cavirostris)". In: *Bioinspiration & Biomimetics* 3.1, p. 016001.

Cranford, Ted W et al. (2008). "Anatomic geometry of sound transmission and reception in Cuvier's beaked whale (Ziphius cavirostris)". In: *The Anatomical Record: Advances in Integrative Anatomy and Evolutionary Biology* 291.4, pp. 353–378.

Cranford, Ted W et al. (2014). "Validation of a vibroacoustic finite element model using bottlenose dolphin simulations: the dolphin biosonar beam is focused in stages". In: *Bioacoustics* 23.2, pp. 161–194.

Cremers, Cor, Ad Snik, and Andy Beynon (1992). "Hearing with the bone-anchored hearing aid (BAHA, HC 200) compared to a conventional bone-conduction hearing aid". In: *Clinical Otolaryngology & Allied Sciences* 17.3, pp. 275–279.

Currey, John D (2013). *Bones: structure and mechanics*. Princeton university press.

Derode, Arnaud, Philippe Roux, and Mathias Fink (1995). "Robust acoustic time reversal with high-order multiple scattering". In: *Physical review letters* 75.23, p. 4206.

Derode, Arnaud, Arnaud Tourin, and Mathias Fink (2001). "Random multiple scattering of ultrasound. II. Is time reversal a self-averaging process?" In: *Physical Review E* 64.3, p. 036606.

Derode, Arnaud et al. (2003). "Recovering the Green's function from field-field correlations in an open scattering medium (L)". In: *The Journal of the Acoustical Society of America* 113.6, pp. 2973–2976.

Dible, Sam A, James A Flint, and Paul A Lepper (2009). "On the role of periodic structures in the lower jaw of the Atlantic bottlenose dolphin (Tursiops truncatus)". In: *Bioinspiration & biomimetics* 4.1, p. 015005.

Dickson, Robert M et al. (1997). "On/off blinking and switching behaviour of single molecules of green fluorescent protein". In: *Nature* 388.6640, pp. 355–358.

Dierauf, Leslie and Frances MD Gulland (2001). *CRC handbook of marine mammal medicine: health, disease, and rehabilitation*. CRC press.

Digimorph (2002). *Digital morphology: a national science foundation digital library at the University of Texas at Austin*.

Dimarogonas, Andrew D (1996). *Vibration for engineers*. Prentice Hall.

Dobbins, Peter (2007). "Dolphin sonar—modelling a new receiver concept". In: *Bioinspiration & biomimetics* 2.1, p. 19.

Draeger, Carsten and Mathias Fink (1999). "One-channel time-reversal in chaotic cavities: Theoretical limits". In: *The Journal of the Acoustical Society of America* 105.2, pp. 611–617.

Dumbser, Michael and Martin Käser (2006). "An arbitrary high-order discontinuous Galerkin method for elastic waves on unstructured meshes—II. The three-dimensional isotropic case". In: *Geophysical Journal International* 167.1, pp. 319–336.

Edelmann, Geoffrey F et al. (2002). "An initial demonstration of underwater acoustic communication using time reversal". In: *IEEE journal of oceanic engineering* 27.3, pp. 602–609.

Errico, Claudia et al. (2015). "Ultrafast ultrasound localization microscopy for deep super-resolution vascular imaging". In: *Nature* 527.7579, pp. 499–508.

Erulkar, Solomon D (1972). "Comparative aspects of spatial localization of sound." In: *Physiological reviews* 52.1, pp. 237–360.

Evans, EF (1982). "Basic physics and psychophysics of sound". In: *The Senses. Cambridge University Press, Cambridge*, pp. 239–250.

Ewins, David J (1984). *Modal testing: theory and practice*. Vol. 15. Research studies press Letchworth.

Faccioli, Ezio et al. (1997). "2D and 3D elastic wave propagation by a pseudo-spectral domain decomposition method". In: *Journal of seismology* 1.3, pp. 237–251.

Fahlke, Julia M et al. (2011). "Cranial asymmetry in Eocene archaeocete whales and the evolution of directional hearing in water". In: *Proceedings of the National Academy of Sciences* 108.35, pp. 14545–14548.

Fahy, Frank J and Paolo Gardonio (2007). *Sound and structural vibration: radiation, transmission and response*. Elsevier.

Feinstein, Stephen H (1973). "Acuity of the human sound localization response underwater". In: *The Journal of the Acoustical Society of America* 53.2, pp. 393–399.

Fink, Mathias (1992). "Time reversal of ultrasonic fields. I. Basic principles". In: *IEEE transactions on ultrasonics, ferroelectrics, and frequency control* 39.5, pp. 555–566.

— (1999). "Time-reversed acoustics". In: *Scientific American* 281.5, pp. 91–97.

— (2001). "Acoustic Time-Reversal Mirrors". In: *Imaging of Complex Media with Acoustic and Seismic Waves* 17, pp. 17–43.

— (2006). "Time-reversal acoustics in complex environments". In: *Geophysics* 71.4, SI151–SI164.

Fink, Mathias et al. (2000). "Time-reversed acoustics". In: *Reports on Progress in Physics* 63.12, p. 1933.

Fink, Mathias et al. (2009). "Time-reversed waves and super-resolution". In: *Comptes Rendus Physique* 10.5, pp. 447–463.

Firestone, Floyd Alburn (1930). "The phase difference and amplitude ratio at the ears due to a source of pure tone". In: *The Journal of the Acoustical Society of America* 2.2, pp. 260–270.

Frizzell, Leon A, Edwin L Carstensen, and Joseph F Dyro (1976). "Shear properties of mammalian tissues at low megahertz frequencies". In: *The Journal of the Acoustical Society of America* 60.6, pp. 1409–1411.

Gernsback, Hugo (1924). U.S. Patent No. 1,521,287.

Ginsberg, Jerry H (2017). *Acoustics-a Textbook for Engineers and Physicists: Volume I: Fundamentals*. Springer.

Goldstein, Herbert (2011). *Classical mechanics*. Pearson Education India.

Graf, Sabine et al. (2009). "Acoustic modelling of dolphin sound reception and implications for biosonar design". In: *OCEANS 2009-EUROPE*. IEEE, pp. 1–6.

Gray, Michael D and Peter H Rogers (2017). "In vivo ultrasonic attenuation in cetacean soft tissues". In: *The Journal of the Acoustical Society of America* 141.2, EL83–EL88.

Guicciardini, Niccolò (2005). "Isaac newton, philosophiae naturalis principia mathematica, (1687)". In: *Landmark Writings in Western Mathematics 1640-1940*. Elsevier, pp. 59–87.

Haan, Frederik W Reysenbach de (1957). "Hearing in whales." In: *Acta oto-laryngologica. Supplementum* 134, p. 1.

Håkansson, Bo et al. (1994). "Resonance frequencies of the human skull invivo". In: *The Journal of the Acoustical Society of America* 95.3, pp. 1474–1481.

Hartmann, William M (1999). "How we localize sound". In: *Physics today* 52, pp. 24–29.

Hecox, Kurt and Robert Galambos (1974). "Brain stem auditory evoked responses in human infants and adults". In: *Archives of otolaryngology* 99.1, pp. 30–33.

Heffner, Henry E and Rickye S Heffner (2016). "The evolution of mammalian sound localization". In: *Acoustics Today* 12, pp. 20–27.

Heffner, Rickye S and Henry E Heffner (1992). "Evolution of sound localization in mammals". In: *The evolutionary biology of hearing*. Springer, pp. 691–715.

Heffner, Rickye S, Gimseong Koay, and Henry E Heffner (2010). "Use of binaural cues for sound localization in large and small non-echolocating bats: Eidolon helvum and Cynopterus brachyotis". In: *The Journal of the Acoustical Society of America* 127.6, pp. 3837–3845.

— (2014). "Hearing in alpacas (Vicugna pacos): Audiogram, localization acuity, and use of binaural locus cues". In: *The Journal of the Acoustical Society of America* 135.2, pp. 778–788.

Hell, Stefan W and Jan Wichmann (1994). "Breaking the diffraction resolution limit by stimulated emission: stimulated-emission-depletion fluorescence microscopy". In: *Optics letters* 19.11, pp. 780–782.

Hemilä, Simo, Sirpa Nummela, and Tom Reuter (1999). "A model of the odontocete middle ear". In: *Hearing Research* 133.1-2, pp. 82–97.

— (2010). "Anatomy and physics of the exceptional sensitivity of dolphin hearing (Odontoceti: Cetacea)". In: *Journal of Comparative Physiology A* 196.3, pp. 165–179.

Henry, Paula and Tomasz R Letowski (2007). "Bone Conduction : Anatomy , Physiology , and Communication". In: *Army Research Laboratory*.

Herzing, Denise L and Christine M Johnson (2015). *Dolphin communication and cognition: past, present, and future*. MIT Press.

Hofman, Paul M and A John Van Opstal (1998). "Spectro-temporal factors in two-dimensional human sound localization". In: *The Journal of the Acoustical Society of America* 103.5, pp. 2634–2648.

Hollien, Harry (1969). "Underwater sound localization: preliminary information". In: *The Journal of the Acoustical Society of America* 46.1A, pp. 124–125.

Hollien, Harry and Stephen Feinstein (1975). "Contribution of the external auditory meatus to auditory sensitivity underwater". In: *The Journal of the Acoustical Society of America* 57.6, pp. 1488–1492.

Hu, Shichao et al. (2016). "A local representation of the head-related transfer function". In: *The Journal of the Acoustical Society of America* 140.3, EL285–EL290.

Humanski, Richard A and Robert A Butler (1988). "The contribution of the near and far ear toward localization of sound in the sagittal plane". In: *The Journal of the Acoustical Society of America* 83.6, pp. 2300–2310.

Hunter, John and Joseph Banks (1787). "Observations on the Structure and Oeconomy of Whales." In: *Philosophical Transactions of the Royal Society of London* 77, pp. 371–450.

Igel, Heiner (2017). *Computational seismology: a practical introduction*. Oxford University Press.

Igel, Heiner, Tarje Nissen-Meyer, and Gunnar Jahnke (2002). "Wave propagation in 3D spherical sections: effects of subduction zones". In: *Physics of the Earth and Planetary Interiors* 132.1-3, pp. 219–234.

Iida, Kazuhiro et al. (2007). "Median plane localization using a parametric model of the head-related transfer function based on spectral cues". In: *Applied Acoustics* 68.8, pp. 835–850.

Ing, Ros K and Mathias Fink (1998). "Time-reversed Lamb waves". In: *IEEE transactions on ultrasonics, ferroelectrics, and frequency control* 45.4, pp. 1032–1043.

Ing, Ros Kiri et al. (2005). "In solid localization of finger impacts using acoustic time-reversal process". In: *Applied Physics Letters* 87.20, p. 204104.

Jeffress, Lloyd A (1948). "A place theory of sound localization." In: *Journal of comparative and physiological psychology* 41.1, p. 35.

Jensen, Finn B et al. (2000). *Computational ocean acoustics*. Springer Science & Business Media.

Jensen, Frants Havmand et al. (2009). "Biosonar adjustments to target range of echolocating bottlenose dolphins (Tursiops sp.) in the wild". In: *Journal of Experimental Biology* 212.8, pp. 1078–1086.

Johnson, C Scott (1967). "Sound detection thresholds in marine mammals". In: *Marine bio-acoustics* 2, pp. 247–260.

Kabanikhin, Sergei Igorevich (2008). "Definitions and examples of inverse and ill-posed problems". In: *Journal of Inverse and Ill-Posed Problems* 16.4, pp. 317–357.

Kassewitz, Jack et al. (2016). "A Phenomenon Discovered While Imaging Dolphin Echolocation Sounds". In: *J Marine Sci Res Dev* 6.202, p. 2.

Kästle, Emanuel D et al. (2018). "Surface Wave Tomography of the Alps Using Ambient-Noise and Earthquake Phase Velocity Measurements". In: *Journal of Geophysical Research: Solid Earth* 123.2, pp. 1770–1792.

Keller, Clifford H, Klaus Hartung, and Terry T Takahashi (1998). "Head-related transfer functions of the barn owl: measurement and neural responses". In: *Hearing research* 118.1, pp. 13–34.

Kellogg, Winthrop N (1958). "Echo ranging in the porpoise". In: *Science* 128.3330, pp. 982–988.

Ketten, Darlene R (1992). "The marine mammal ear: specializations for aquatic audition and echolocation". In: *The evolutionary biology of hearing*. Springer, pp. 717–750.

Ketten, Darlene R. (2000). "Cetacean Ears". In: *Hearing by Whales and Dolphins*. New York, NY: Springer New York, pp. 43–108.

Ketten, DR (1994). "Functional analyses of whale ears: adaptations for underwater hearing". In: *OCEANS'94.'Oceans Engineering for Today's Technology and Tomorrow's Preservation.'Proceedings*. Vol. 1. IEEE, pp. I–264.

Kim, Seongil et al. (2003). "Robust time reversal focusing in the ocean". In: *The Journal of the Acoustical Society of America* 114.1, pp. 145–157.

Kinsler, Lawrence E et al. (1999). *Fundamentals of acoustics*. Wiley-VCH.

Klump, Georg M (2000). "Sound localization in birds". In: *Comparative hearing: birds and reptiles*. Springer, pp. 249–307.

Komatitsch, Dimitri, Jeroen Ritsema, and Jeroen Tromp (2002). "The spectral-element method, Beowulf computing, and global seismology". In: *Science* 298.5599, pp. 1737–1742.

Komatitsch, Dimitri and Jeroen Tromp (1999). "Introduction to the spectral element method for three-dimensional seismic wave propagation". In: *Geophysical journal international* 139.3, pp. 806–822.

Komatitsch, Dimitri and Jean-Pierre Vilotte (1998). "The spectral element method: An efficient tool to simulate the seismic response of 2D and 3D geological structures". In: *Bulletin of the seismological society of America* 88.2, pp. 368–392.

Konishi, Masakazu (2003). "Coding of auditory space". In: *Annual review of neuroscience* 26.1, pp. 31–55.

Koopman, Heather N et al. (2006). "Topographical distribution of lipids inside the mandibular fat bodies of odontocetes: remarkable complexity and consistency". In: *IEEE Journal of Oceanic Engineering* 31.1, pp. 95–106.

Köppl, Christine (2009). "Evolution of sound localisation in land vertebrates". In: *Current Biology* 19.15, R635–R639.

Kristek, Jozef and Peter Moczo (2003). "Seismic-wave propagation in viscoelastic media with material discontinuities: A 3D fourth-order staggered-grid finite-difference modeling". In: *Bulletin of the Seismological Society of America* 93.5, pp. 2273–2280.

Krysl, Peter, Ted W Cranford, and John A Hildebrand (2008). "Lagrangian finite element treatment of transient vibration/acoustics of biosolids immersed in fluids". In: *International journal for numerical methods in engineering* 74.5, pp. 754–775.

Krysl, Petr and Ted W Cranford (2016). "Directional Hearing and Head-Related Transfer Function in Odontocete Cetaceans". In: *The Effects of Noise on Aquatic Life II*. Springer, pp. 583–587.

Kuhn, George F (1977). "Model for the interaural time differences in the azimuthal plane". In: *The Journal of the Acoustical Society of America* 62.1, pp. 157–167.

Kulkarni, Abhijit and H Steven Colburn (1998). "Role of spectral detail in sound-source localization". In: *Nature* 396.6713, p. 747.

Lamb, Horace (1917). "On waves in an elastic plate". In: *Proc. R. Soc. Lond. A* 93.648, pp. 114–128.

Larmat, Carene et al. (2006). "Time-reversal imaging of seismic sources and application to the great Sumatra earthquake". In: *Geophysical Research Letters* 33.19.

Lazan, Benjamin Joseph (1968). *Damping of materials and members in structural mechanics*. Vol. 42. Pergamon press Oxford.

Ledford, Heidi (2007). *Better sonar through dolphin teeth*. URL: https://www.nature.com/news/2007/070319/full/news070319-2.html.

Lerosey, Geoffroy et al. (2007). "Focusing beyond the diffraction limit with far-field time reversal". In: *Science* 315.5815, pp. 1120–1122.

Lewis, AMAA et al. (1984). "Development of a 500 Å spatial resolution light microscope: I. light is efficiently transmitted through $\lambda/16$ diameter apertures". In: *Ultramicroscopy* 13.3, pp. 227–231.

Li, Faqi et al. (2015). "Frequency dependence of the acoustic field generated from a spherical cavity transducer with open ends". In: *AIP Advances* 5.12, p. 127218.

Littler, TS, JJ Knight, and PH Strange (1952). "Hearing by bone conduction and the use of bone-conduction hearing aids". In: *Proceedings of the Royal Society of Medicine* 45.11, p. 783.

Long, Kevin Jay and Neil Allen (1984). "Abnormal brain-stem auditory evoked potentials following Ondine's curse". In: *Archives of neurology* 41.10, pp. 1109–1110.

Lu, Ye (2013). "Comparison of finite element method and modal analysis of violin top plate". PhD thesis. McGill University, Department of Music Research.

MacLeod, Colin D et al. (2007). "Breaking symmetry: The marine environment, prey size, and the evolution of asymmetry in cetacean skulls". In: *The Anatomical Record: Advances in Integrative Anatomy and Evolutionary Biology: Advances in Integrative Anatomy and Evolutionary Biology* 290.6, pp. 539–545.

Macpherson, Ewan A and Andrew T Sabin (2013). "Vertical-plane sound localization with distorted spectral cues". In: *Hearing research* 306, pp. 76–92.

Madsen, Ernest L, H John Sathoff, and James A Zagzebski (1983). "Ultrasonic shear wave properties of soft tissues and tissuelike materials". In: *The Journal of the Acoustical Society of America* 74.5, pp. 1346–1355.

Malvern, Lawrence E (1969). *Introduction to the Mechanics of a Continuous Medium*. Prentice-Hall Inc.

Manen, Dirk-Jan van, Andrew Curtis, and Johan O Robertsson (2006). "Interferometric modeling of wave propagation in inhomogeneous elastic media using time reversal and reciprocity". In: *Geophysics* 71.4, SI47–SI60.

Manen, Dirk-Jan van, Johan OA Robertsson, and Andrew Curtis (2005). "Modeling of wave propagation in inhomogeneous media". In: *Physical Review Letters* 94.16, p. 164301.

Marino, Lori (1998). "A comparison of encephalization between odontocete cetaceans and anthropoid primates". In: *Brain, Behavior and Evolution* 51.4, pp. 230–238.

Martin, Roland et al. (2008). "Simulation of seismic wave propagation in an asteroid based upon an unstructured MPI spectral-element method: blocking and non-blocking communication strategies". In: *High Performance Computing for Computational Science-VECPAR 2008*, pp. 350–363.

Masterton, Bruce, Henry Heffner, and Richard Ravizza (1969). "The evolution of human hearing". In: *The Journal of the Acoustical Society of America* 45.4, pp. 966–985.

May, Bradford J et al. (1995). "Design and conduct of sensory experiments for domestic cats". In: *Methods in comparative psychoacoustics*. Springer, pp. 95–108.

Mayer, Alfred (1880). *Patent US 224199 A*. Granted Patent. United States.

McAlpine, David and Benedikt Grothe (2003). "Sound localization and delay lines–do mammals fit the model?" In: *Trends in neurosciences* 26.7, pp. 347–350.

McCormick, James G et al. (1970). "Sound conduction in the dolphin ear". In: *The Journal of the Acoustical Society of America* 48.6B, pp. 1418–1428.

McCormick, James G et al. (1980). "Sound reception in the porpoise as it relates to echolocation". In: *Animal sonar systems*. Springer, pp. 449–467.

Mead, James G (1975). "Anatomy of the external nasal passages and facial complex in the Delphinidae (Mammalia: Cetacea)". In:

Michelinie, David and Frank Miller (1980). *Daredevil (#167) - The man without fear*. Marvel Comics Group.

Middlebrooks, John C (1999). "Individual differences in external-ear transfer functions reduced by scaling in frequency". In: *The Journal of the Acoustical Society of America* 106.3, pp. 1480–1492.

— (2015). "Sound localization". In: *Handbook of clinical neurology*. Vol. 129. Elsevier, pp. 99–116.

Mills, Allen William (1958). "On the minimum audible angle". In: *The Journal of the Acoustical Society of America* 30.4, pp. 237–246.

Minnaar, Pauli et al. (2001). "Localization with binaural recordings from artificial and human heads". In: *Journal of the Audio Engineering Society* 49.5, pp. 323–336.

Møhl, Bertel et al. (2003). "The monopulsed nature of sperm whale clicks". In: *The Journal of the Acoustical Society of America* 114.2, pp. 1143–1154.

Montie, Eric W, Charlie A Manire, and David A Mann (2011). "Live CT imaging of sound reception anatomy and hearing measurements in the pygmy killer whale, Feresa attenuata". In: *Journal of Experimental Biology* 214.6, pp. 945–955.

Mooney, T Aran, Maya Yamato, and Brian K Branstetter (2012). "Hearing in cetaceans: from natural history to experimental biology". In: *Adv. Mar. Biol* 63.197-246.

Moore, Patrick WB and Whitlow WL Au (1975). "Underwater localization of pulsed pure tones by the California sea lion (Z alophuscalifornianus)". In: *The Journal of the Acoustical Society of America* 58.3, pp. 721–727.

Moore, Patrick WB, Deborah A Pawloski, and Lois Dankiewicz (1995). "Interaural time and intensity difference thresholds in the bottlenose dolphin (Tursiops truncatus)". In: *Sensory Systems of Aquatic Mammals*, pp. 11–23.

Mulsow, Jason, James J Finneran, and Dorian S Houser (2014). "Interaural differences in the bottlenose dolphin (Tursiops truncatus) auditory nerve response to jawphone click stimuli". In: *The Journal of the Acoustical Society of America* 136.3, pp. 1402–1409.

Musicant, Alan D and Robert A Butler (1984). "The influence of pinnae-based spectral cues on sound localization". In: *The Journal of the Acoustical Society of America* 75.4, pp. 1195–1200.

Nachtigall, Paul E. (2016). *Biosonar and Sound Localization in Dolphins,* Oxford Research Encyclopedia of Neuroscience.

Norberg, R Åke (1978). "Skull asymmetry, ear structure and function, and auditory localization in Tengmalm's owl, Aegolius funereus (Linné)". In: *Phil. Trans. R. Soc. Lond. B* 282.991, pp. 325–410.

Norris, Kenneth S. (1964). "Some problems of echolocation in cetaceans". In: *Marine Bioacoustics*. Ed. by William N. Tavolga. New York: Pergamon Press, pp. 316–336.

— (1968a). "The echolocation of marine mammals." In: *The biology of marine mammals*. Ed. by Harald T. Andersen. New York: Academic Press, pp. 391–423.

— (1968b). "The evolution of acoustic mechanisms in odontocete cetaceans". In: *Evolution and Environment*. Ed. by Ellen T. Drake. New York: Yale University Press, pp. 297–324.

Norris, Kenneth S and George W Harvey (1974). "Sound transmission in the porpoise head". In: *The Journal of the Acoustical Society of America* 56.2, pp. 659–664.

Norris, Kenneth S et al. (1961). "An experimental demonstration of echolocation behavior in the porpoise, Tursiops truncatus (Montagu)". In: *The Biological Bulletin* 120.2, pp. 163–176.

Nummela, Sirpa et al. (2007). "Sound transmission in archaic and modern whales: anatomical adaptations for underwater hearing". In: *The Anatomical Record: Advances in Integrative Anatomy and Evolutionary Biology: Advances in Integrative Anatomy and Evolutionary Biology* 290.6, pp. 716–733.

Oberrecht, Steve P, Petr Krysl, and Ted W Cranford (2016). "Sound transmission validation and sensitivity studies in numerical models". In: *The Effects of Noise on Aquatic Life II*. Springer, pp. 785–789.

Packard, Hewlett (1997). *The fundamentals of modal testing*. Tech. rep. Application note 243-3.

Park, Hyun Woo, Seung Bum Kim, and Hoon Sohn (2009). "Understanding a time reversal process in Lamb wave propagation". In: *Wave Motion* 46.7, pp. 451–467.

Parseihian, Gaëtan, Christophe Jouffrais, and Brian FG Katz (2014). "Reaching nearby sources: comparison between real and virtual sound and visual targets". In: *Frontiers in neuroscience* 8.

Pellegrini, François and Jean Roman (1996). "Scotch: A software package for static mapping by dual recursive bipartitioning of process and architecture graphs". In: *High-Performance Computing and Networking*. Springer, pp. 493–498.

Pendry, John Brian (2000). "Negative refraction makes a perfect lens". In: *Physical review letters* 85.18, p. 3966.

Perconti, James (1992). "Practical application of modal analysis techniques". PhD thesis. Rochester Institute of Technology.

Perrott, David R and Kourosh Saberi (1990). "Minimum audible angle thresholds for sources varying in both elevation and azimuth". In: *The Journal of the Acoustical Society of America* 87.4, pp. 1728–1731.

Petroski, Henry (1985). *To engineer is human: The role of failure in successful design*. St. Martin's Press New York.

Pike, Edward Roy and Pierre C Sabatier (2001). *Scattering, Two-Volume Set: Scattering and Inverse Scattering in Pure and Applied Science*. Elsevier.

Pohl, Dieter W, W Denk, and M Lanz (1984). "Optical stethoscopy: Image recording with resolution $\lambda/20$". In: *Applied physics letters* 44.7, pp. 651–653.

Popov, Vladimir V and Alexander Ya Supin (1990). "Localization of the acoustic window at the dolphin's head". In: *Sensory Abilities of Cetaceans*. Springer, pp. 417–426.

— (1991). "Interaural intensity and latency difference in the dolphin's auditory system". In: *Neuroscience letters* 133.2, pp. 295–297.

Pourciau, Bruce (2011). "Is Newton's second law really Newton's?" In: *American Journal of Physics* 79.10, pp. 1015–1022.

Pratt, Carroll C (1930). "The spatial character of high and low tones." In: *Journal of Experimental Psychology* 13.3, p. 278.

Priolo, Enrico, José M Carcione, and Géza Seriani (1994). "Numerical simulation of interface waves by high-order spectral modeling techniques". In: *The Journal of the Acoustical Society of America* 95.2, pp. 681–693.

Rayleigh, John William Strutt Baron (1896). *The theory of sound*. Vol. 2. Macmillan.

— (1907). "XII. On our perception of sound direction". In: *The London, Edinburgh, and Dublin Philosophical Magazine and Journal of Science* 13.74, pp. 214–232.

Reinwald, Michael (2015). "Reducing non-uniqueness in probabilistic finite fault inversion for a normal fault". MA thesis. Ludwig-Maximilians-Universität München, Department of Earth and Environmental Sciences, Geophysics.

Reinwald, Michael et al. (2018). "Bone-conducted sound in a dolphin's mandible: Experimental investigation of elastic waves mediating information on sound source position." submitted.

Renaud, Donna L and Arthur N Popper (1975). "Sound localization by the bottlenose porpoise Tursiops truncatus". In: *Journal of Experimental Biology* 63.3, pp. 569–585.

Richardson, W John et al. (2013). *Marine mammals and noise*. Academic press.

Ridgway, Sam H (2000). "The auditory central nervous system of dolphins". In: *Hearing by whales and dolphins*. Springer, pp. 273–293.

Roffler, Suzanne K and Robert A Butler (1968a). "Factors that influence the localization of sound in the vertical plane". In: *The Journal of the Acoustical Society of America* 43.6, pp. 1255–1259.

— (1968b). "Factors that influence the localization of sound in the vertical plane". In: *The Journal of the Acoustical Society of America* 43.6, pp. 1255–1259.

Rosny, Julien de and Mathias Fink (2002). "Overcoming the diffraction limit in wave physics using a time-reversal mirror and a novel acoustic sink". In: *Physical review letters* 89.12, p. 124301.

— (2007). "Focusing properties of near-field time reversal". In: *Physical Review A* 76.6, p. 065801.

Roux, Philippe and Mathias Fink (1995). "Experimental evidence in acoustics of the violation of time-reversal invariance induced by vorticity". In: *EPL (Europhysics Letters)* 32.1, p. 25.

Rupin, Matthieu, Stefan Catheline, and Philippe Roux (2015). "Super-resolution experiments on lamb waves using a single emitter". In: *Applied Physics Letters* 106.2, p. 024103.

Ryabov, VA (2010). "Role of the mental foramens in dolphin hearing". In: *Natural Science* 2.6, pp. 646–653.

Sanz, M Garcia et al. (2013). "Imaging methodologies in natural sciences: The AST-RX Platform (Accès Scientifique à la Tomographie à Rayons X) of the Muséum national d'Histoire naturelle. Paris". In: *UVX 2012-11e Colloque sur les Sources Cohérentes et Incohérentes UV, VUV et X; Applications et Développements Récents*. EDP Sciences, p. 01001.

Savel, Sophie and Carolyn Drake (2000). "Psychoacoustic investigation of auditory cues involved in human underwater sound localization". In: *5th European Conference on underwater acoustics*.

Schenk, Olaf et al. (2001). "PARDISO: a high-performance serial and parallel sparse linear solver in semiconductor device simulation". In: *Future Generation Computer Systems* 18.1, pp. 69–78.

Sigurdson, John E (1997). "Analyzing the dynamics of dolphin biosonar behaviour during search and detection tasks". In: *Proceedings - Institute of Acoustics* 19, pp. 123–132.

Simonetti, F (2006). "Localization of pointlike scatterers in solids with subwavelength resolution". In: *Applied physics letters* 89.9, p. 094105.

Soldevilla, Melissa S et al. (2005). "Cuvier's beaked whale (Ziphius cavirostris) head tissues: physical properties and CT imaging". In: *Journal of experimental biology* 208.12, pp. 2319–2332.

Soldevilla, Melissa S et al. (2008). "Classification of Risso's and Pacific white-sided dolphins using spectral properties of echolocation clicks". In: *The Journal of the Acoustical Society of America* 124.1, pp. 609–624.

Song, Zhongchang et al. (2016). "Inducing rostrum interfacial waves by fluid-solid coupling in a Chinese river dolphin (Lipotes vexillifer)". In: *Physical Review E* 93.1, p. 012411.

Stein, Seth and Michael Wysession (2009). *An introduction to seismology, earthquakes, and earth structure*. John Wiley & Sons.

Stenfelt, Stefan (2011). "Acoustic and physiologic aspects of bone conduction hearing". In: *Implantable Bone Conduction Hearing Aids*. Vol. 71. Karger Publishers, pp. 10–21.

Stenfelt, Stefan and Richard L Goode (2005). "Bone-conducted sound: physiological and clinical aspects". In: *Otology & Neurotology* 26.6, pp. 1245–1261.

Stevens, Stanley Smith and Edwin B Newman (1936). "The localization of actual sources of sound". In: *The American journal of psychology* 48.2, pp. 297–306.

Stouffer, James L, E Thomas Doherty, and Harry Hollien (1975). "Effect of training on human underwater sound-localization ability". In: *The Journal of the Acoustical Society of America* 57.5, pp. 1212–1213.

Strutt, John William (1877). "VI. On the application of the principle of reciprocity to acoustics". In: *Proceedings of the Royal Society of London* 25.171-178, pp. 118–122.

Supin, Alexander Ya and Vladimir V Popov (1993). "Direction-dependent spectral sensitivity and interaural spectral difference in a dolphin: Evoked potential study". In: *The Journal of the Acoustical Society of America* 93.6, pp. 3490–3495.

Supin, Alexander Ya, Vladimir V Popov, and Alla M Mass (2012). *The sensory physiology of aquatic mammals*. Springer Science & Business Media.

Takeuchi, Nozomu and Robert J Geller (2000). "Optimally accurate second order time-domain finite difference scheme for computing synthetic seismograms in

2-D and 3-D media". In: *Physics of the earth and planetary interiors* 119.1-2, pp. 99–131.

Tanimoto, Toshiro (1990). "Modelling curved surface wave paths: membrane surface wave synthetics". In: *Geophysical Journal International* 102.1, pp. 89–100.

Tanter, Mickaël, Jean-Louis Thomas, and Mathias Fink (2000). "Time reversal and the inverse filter". In: *The Journal of the Acoustical Society of America* 108.1, pp. 223–234.

Tanter, Mickaël et al. (2001). "Optimal focusing by spatio-temporal inverse filter. I. Basic principles". In: *The Journal of the Acoustical Society of America* 110.1, pp. 37–47.

Tarantola, Albert (2005). *Inverse problem theory and methods for model parameter estimation*. Vol. 89. siam.

Taschke, Henning and Herbert Hudde (2006). "A finite element model of the human head for auditory bone conduction simulation". In: *Orl* 68.6, pp. 319–323.

Taylor, Kristen A (2013). "Directional hearing and a head-related transfer function (HRTF) of a bottlenose dolphin (Tursiops truncatus)". PhD thesis. University of Hawai'i at Manoa.

Thomas, Jeanette A, Cynthia F Moss, and Marianne Vater (2004). *Echolocation in bats and dolphins*. University of Chicago Press.

Tjellström, Anders and B Håkansson (1995). "The bone-anchored hearing aid. Design principles, indications, and long-term clinical results." In: *Otolaryngologic clinics of North America* 28.1, pp. 53–72.

Tromp, Jeroen and FA Dahlen (1993). "Variational principles for surface wave propagation on a laterally heterogeneous Earth—III. Potential representation". In: *Geophysical Journal International* 112.2, pp. 195–209.

Tsogka, Chrysoula and George C Papanicolaou (2002). "Time reversal through a solid–liquid interface and super-resolution". In: *Inverse problems* 18.6, p. 1639.

Van Opstal, John (2016). *The auditory system and human sound-localization behavior*. Academic Press.

Van Wanrooij, Marc M and A John Van Opstal (2004). "Contribution of head shadow and pinna cues to chronic monaural sound localization". In: *Journal of Neuroscience* 24.17, pp. 4163–4171.

Van Wijk, Kasper et al. (2004). "Analysis of strong scattering at the micro-scale". In: *The Journal of the Acoustical Society of America* 115.3, pp. 1006–1011.

Walker, Bruce N et al. (2005). "Evaluation of bone-conduction headsets for use in multitalker communication environments". In: *Proceedings of the Human Factors and Ergonomics Society - 49th Annual Meeting* 49.17, pp. 1615–1619.

Wapenaar, Kees and Jacob Fokkema (2006). "Green's function representations for seismic interferometry". In: *Geophysics* 71.4, SI33–SI46.

Wartzok, Douglas and Darlene R@bookdierauf2001crc, title=CRC handbook of marine mammal medicine: health, disease, and rehabilitation, author=Dierauf, Leslie

and Gulland, Frances MD, year=2001, publisher=CRC press Ketten (1999). "Marine mammal sensory systems". In: *Biology of marine mammals* 1, p. 117.

Wazen, Jack J et al. (2001). "Results of the Bone-Anchored Hearing Aid in Unilateral Hearing Loss". In: *The Laryngoscope* 111.6, pp. 955–958.

Wei, Chong, Yu Zhang, and Whitlow WL Au (2014). "Simulation of ultrasound beam formation of baiji (Lipotes vexillifer) with a finite element model". In: *The Journal of the Acoustical Society of America* 136.1, pp. 423–429.

Wenzel, Elizabeth M et al. (1993). "Localization using nonindividualized head-related transfer functions". In: *The Journal of the Acoustical Society of America* 94.1, pp. 111–123.

Wettschurek, R (1973). "Die absoluten Unterschiedsschwellen der Richtungswahrnehmung in der Medianebene beim natürlichen Hören, sowie beim Hören über ein Kunstkopf-Übertragungssystem". In: *Acustica* 28.4, pp. 197–208.

Wightman, Frederic L and Doris J Kistler (1989). "Headphone simulation of free-field listening. I: stimulus synthesis". In: *The Journal of the Acoustical Society of America* 85.2, pp. 858–867.

Wilson, Don E (2002). "Encyclopedia of Marine Mammals". In: *Journal of Mammalogy* 83.4, p. 1151.

Woodworth, Robert S and Harold Schlosberg (1938). "Experimental psychology. New York: Henry Holt and Company". In:

Xie, Bosun (2013). *Head-related transfer function and virtual auditory display*. J. Ross Publishing.

Xie, Zhinan et al. (2014). "Improved forward wave propagation and adjoint-based sensitivity kernel calculations using a numerically stable finite-element PML". In: *Geophysical Journal International* 198.3, pp. 1714–1747.

Xie, Zhinan et al. (2016). "A perfectly matched layer for fluid-solid problems: Application to ocean-acoustics simulations with solid ocean bottoms". In: *The Journal of the Acoustical Society of America* 140.1, pp. 165–175.

Xu, Buli and Victor Giurgiutiu (2007). "Single mode tuning effects on Lamb wave time reversal with piezoelectric wafer active sensors for structural health monitoring". In: *Journal of Nondestructive Evaluation* 26.2-4, pp. 123–134.

Yilmaz, Öz (2001). *Seismic data analysis: Processing, inversion, and interpretation of seismic data*. Society of exploration geophysicists.

Youssef, Karim, Sylvain Argentieri, and Jean-Luc Zarader (2012). "Towards a systematic study of binaural cues". In: *Intelligent Robots and Systems (IROS), 2012 IEEE/RSJ International Conference on*. IEEE, pp. 1004–1009.

Zienkiewicz, Olek C and Robert L Taylor (2005). *The finite element method for solid and structural mechanics*. Elsevier.